University of Dundee

DOCTOR OF PHILOSOPHY

The origin and dynamic interaction of solar magnetic fields

Wilmot-Smith, Antonia

Award date:
2007

Awarding institution:
University of St Andrews

Link to publication

The origin and dynamic interaction of solar magnetic fields

Antonia Wilmot-Smith

2007

University of St Andrews

The origin and dynamic interaction of solar magnetic fields

Antonia Wilmot-Smith

Thesis submitted for the degree of Doctor of Philosophy

of the University of St Andrews

21st June 2007

Abstract

The dynamics of the solar corona are dominated by the magnetic field which creates its structure. The magnetic field in most of the corona is 'frozen' to the plasma very effectively. The exception is in small localised regions of intense current concentrations where the magnetic field can slip through the plasma and a restructuring of the magnetic field can occur. This process is known as magnetic reconnection and is believed to be responsible for a wide variety of phenomena in the corona, from the rapid energy release of solar flares to the heating of the high-temperature corona.

The coronal field itself is three-dimensional (3D), but much of our understanding of reconnection has been developed through two-dimensional (2D) models. This thesis describes several models for fully 3D reconnection, with both kinematic and fully dynamic models presented. The reconnective behaviour is shown to be fundamentally different in many respects from the 2D case. In addition a numerical experiment is described which examines the reconnection process in coronal magnetic flux tubes whose photospheric footpoints are spun, one type of motion observed to occur on the Sun.

The large-scale coronal field itself is thought to be generated by a magnetohydrodynamic dynamo operating in the solar interior. Although the dynamo effect itself is not usually associated with reconnection, since the essential element of the problem is to account for the presence of large-scale fields, reconnection is essential for the restructuring of the amplified small-scale flux. Here we examine some simple models of the solar-dynamo process, taking advantage of their simplicity to make a full exploration of their behaviour in a variety of parameter regimes. A wide variety of dynamic behaviour is found in each of the models, including aperiodic modulation of cyclic solutions and intermittency that strongly resembles the historic record of solar magnetic activity.

Declaration

I, Antonia Wilmot-Smith, hereby certify that this thesis, which is approximately 45,000 words in length, has been written by me, that it is the record of work carried out by me and that it has not been submitted in any previous application for a higher degree.

Signature of candidate . . . .   **Date** . . . .

I was admitted as a research student in September, 2004 and as a candidate for the degree of Doctor of Philosophy in September, 2005; the higher study for which this is a record was carried out in the University of St Andrews between 2004 and 2007.

Signature of candidate . . . .   **Date** . . . .

I hereby certify that the candidate has fulfilled the conditions of the Resolution and Regulations appropriate for the degree of Doctor of Philosophy in the University of St Andrews and that the candidate is qualified to submit this thesis in application for that degree.

Signature of supervisor . . . .   **Date** . . . .

In submitting this thesis to the University of St Andrews I understand that I am giving permission for it to be made available for use in accordance with the regulations of the University Library for the time being in force, subject to any copyright vested in the work not being affected thereby. I also understand that the title and abstract will be published, and that a copy of the work may be made and supplied to any *bona fide* library or research worker.

Signature of candidate . . . .   **Date** . . . .

Acknowledgements

Contents

List of Figures

Chapter 1

Introduction

Figure 1.1: The solar corona as observed during the total solar eclipses of (*left*) 1980, close to sunspot maximum, and (*right*) 1994, close to sunspot minimum. *Source: High Altitude Observatory.*

Plasmas do not form a significant part of our every-day environment and yet the stars, the interplanetary medium and the interstellar medium are all made of ionised gases. Indeed more than 99% of the visible matter in the universe consists of plasma. A physical understanding of these plasmas is, therefore, of major importance – but hard to come by since the huge spatial scales that characterise the problem are not available for realistic experiments on Earth. Instead, the natural laboratory to turn to is the solar corona, the outer atmosphere of the Sun.

The corona exhibits significant temporal and spatial variability (as has been observed in eclipses for centuries – see Figure 1.1). Its structure is created by the magnetic field that permeates it and is responsible for its extreme temperature; in the 1940s the corona was found to be several hundred times hotter than the underlying visible surface of the Sun, the photosphere. To understand the corona we must understand its magnetic field. Where does the field originate? How does it behave and what are the consequences of the behaviour? These are some of the questions we will examine in this thesis, but first we consider the structure of the Sun in more detail.

The Sun is estimated to have been luminous for about 4.6×10^9 years – the only energy source capable

of meeting such a long term requirement is nuclear fusion. The fusion process occurs in the *core* of the Sun, which extends to 20% of its radius, and is sufficiently hot $\left(15 \times 10^6 \text{K}\right)$ and dense $\left(150 \text{ g/cm}^{-3}\right)$ to sustain the reactions, the most important of which is the proton-proton reaction. Moving further away from the solar centre, the temperature and density decrease such that fusion stops, the transition marking the beginning of the *radiative zone* where energy is transported toward the surface by radiation. Photons travelling (net) outwards through the region continually undergo absorption and re-emission, so increasing their wavelength. When the temperature gradient required to transport the energy flux by radiation is larger than that of an adiabatically stratified hydrostatic equilibrium, the region becomes unstable to convection (the Schwartzschild criterion). As a result, convective fluid motions (which are very efficient in energy transport) occur in the outer 30% of the solar radius, which makes up the *convection zone*. As a source of mechanical energy they are ultimately responsible for the solar magnetic cycle and hence for the majority of solar dynamics. Large-scale convective motions are observed only indirectly, by their manifestations such as magnetic activity in the outer solar regions and the solar rotation profile (deduced by helioseismology), since they tend to be obscured by smaller-scale motions (such as granulation) close to the surface.

Helioseismology uses measurements of global acoustic oscillations on the solar surface (in visible light) to infer properties of the solar interior. Measuring frequency shifts in these p-mode (pressure-mode) oscillations allows the internal velocity profile to be deduced. The convection zone is found to be rotating differentially, faster at the equator ($P \approx 25$ days) than the poles ($P \approx 35$ days) and, at mid-latitudes, the angular velocity contours are approximately radial. The radiative zone, however, rotates as a solid body, and there exists a sharp transition between the two rotational regimes. This transitional layer is known as the *tachocline* (Spiegel and Zahn, 1992, see Hughes et al. (2007) for a recent review) and estimates of its width vary from 0.1% to 0.9% of the solar radius, depending on how the tachocline is defined (for a discussion see Miesch, 2005). The rotation rate of the radiative zone lies between that of the polar region and the equatorial region of the convection zone and so a positive (negative) gradient in the radial angular velocity across the tachocline exists at low (high) latitudes

The radius of the Sun, $R_\odot = 6.96 \times 10^8$ m, is defined by its visible surface, the *photosphere*, where the plasma becomes optically thin (as we move radially outwards). The photosphere is very thin, comprising only 0.07% of the solar radius, and has a temperature of about 5800K. The photosphere is the inner-most layer of the Sun that can be observed directly in great detail. Large-scale *granulation* and *supergranulation* patterns are seen, which, although associated with convection, are thought not to pervade the convection zone but to be confined to approximately only the outer 3% of the solar radius. *Sunspots*, regions of extremely intense field concentration, are another major photospheric feature. They are seen as small dark regions drifting across the surface as they are carried around by the rotating Sun. It was by tracking the motions of sunspots that the solar differential rotation was first inferred.

In the layer above the photosphere, known as the *chromosphere*, the temperature rises to around 20000 K. Emission in $H\alpha$ gives the chromosphere its distinctive red colour, as seen during solar eclipses in *prominences* projecting above the limb. Prominences are regions where plasma at chromospheric temperatures is suspended up in the corona by the magnetic field there (and commonly referred to as filaments when observed on the solar disc). The $H\alpha$ emission line can be used to image the chromosphere. In this line magnetic flux concentrations at the boundaries of photospheric granulation and supergranulation cells appear as the *chromospheric network*, and the chromosphere is found to be non-uniform, containing extended
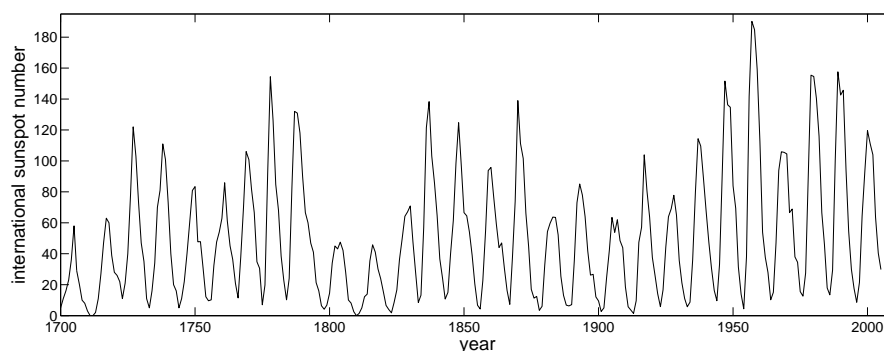
Figure 1.2: International Sunspot Numbers for the years $1700-2005$. The International Sunspot Number is given by $R = K(10G + S)$ where S denotes the number of observed sunspots, G the number of observed sunspot groups and K a quality factor to allow for comparison of results from different observational locations. Data from 40–70 stations are used in the measurements and is compiled at the Royal Observatory of Belgium. *Source: SIDC, RWC Belgium, World Data Centre for the Sunspot Index, Royal Observatory of Belgium, 2007.*

regions known as *spicules* – short lasting features in which plasma is ejected toward the corona. Other chromospheric features include *plages* and *fibrils*.

The *transition region* is a thin, highly irregular and dynamic layer that consists of plasma between chromospheric and coronal temperatures. Finally, the outer layer of the solar atmosphere is the solar corona. The dynamics of all coronal phenomena are controlled by the magnetic field. Although in *coronal seismology* the first attempts are being made to measure the field directly using the properties of coronal waves (Roberts et al., 1984), knowledge of the field is traditionally obtained by extrapolation from magnetograms at the photosphere (using potential or force-free models). The corona itself only becomes visible in white light when the solar disc is occulted – since it is very tenuous, its optical emission is several orders of magnitude less than that of the photosphere. It may, however, be observed in great detail in non-visible wavelengths (such as X-rays) because the brightest emission in these wavelengths comes from the corona and the photosphere is no longer visible.

The solar magnetic field exhibits dramatic spatial and temporal variability. Several of the changes are systematic and occur on very large-scales. For example, the number of sunspots on the face of the Sun varies in time in a cyclic but irregular manner (see Figure 1.2). The *sunspot cycle* varies in length but has an average period of approximately 11 years and, in addition, significant variations in cycle amplitude are present. As sunspots begin to emerge at the beginning of each cycle, they do so at (relatively) high latitudes of around 27° degrees, but as the cycle progresses emergence tends to occur closer to the equator, up to around 8°. Sunspots typically appear in pairs of opposite polarity, with the axis of a bipolar sunspot pair being tilted by about 4° with respect to the equator (Joy's law). The polarity of the leading sunspot (that closest to equator) in each hemisphere reverses at each cycle and has opposite polarity to the leading sunspots in the opposite hemisphere (Hale's law). The sunspot cycle reflects an underlying magnetic cycle with a period of around 22 years, in which the polar field reverses near the time of cycle maximum. The large-scale corona, as demonstrated by Figure 1.1, looks quite different from solar minimum to maximum, with coronal holes covering both poles at minima of activity while a nearly radial field structure is seen at

solar maximum where most of the corona is in the form of magnetically closed loops.

The coronal magnetic field is capable of storing huge amounts of energy as it is injected via turbulent photospheric motions. Its structure is observed to be continually changing on a wide variety of scales and a process known as *magnetic reconnection* is of fundamental importance in this respect. Reconnection is the only process that can change the magnetic field topology and is thought to be responsible for maintaining the unexpectedly high temperature of the corona as well as for a wide variety of explosive events such as *solar flares* and *coronal mass ejections* (CMEs).

In the next section we introduce the equations needed to mathematically describe the behaviour of the solar magnetic field.

1.1 The Equations of Magnetohydrodynamics

In this thesis we will assume the magnetohydrodynamic (MHD) approximation. There are a number of conditions behind this assumption, as discussed in detail in, for example, Priest (1982), Boyd and Sanderson (2003). Briefly, MHD is a theory of non-relativistic macroscopic plasma phenomena. The plasma is treated as a single fluid, with the electron and ion species locked together and is considered quasi-neutral, so the charge density vanishes. Under the non-relativistic assumption the displacement current (that given by $\partial \mathbf{E}/\partial t/c^2$ in Ampère's law) can be neglected. By macroscopic we imply that the typical length- and time-scales of interest are much larger than the typical microscopic length- and time-scales of the ion and electron dynamics (the ion Larmor radius and gyroperiod and the mean free path time and length).

The equations of MHD are:

Mass conservation

$$\frac{\partial \rho}{\partial t} + \nabla \cdot (\rho \mathbf{v}) = 0 \,, \tag{1.1}$$

the equation of motion (or, momentum conservation)

$$\rho \frac{D\mathbf{v}}{Dt} = -\nabla p + \mathbf{j} \times \mathbf{B} + \mathbf{F} \,, \tag{1.2}$$

the ideal gas law

$$p = \rho \mathcal{R} T \,, \tag{1.3}$$

Ampère's law

$$\nabla \times \mathbf{B} = \mu \mathbf{j} \,, \tag{1.4}$$

solenoidal constraint

$$\nabla \cdot \mathbf{B} = 0 \,, \tag{1.5}$$

Faraday's law

$$\frac{\partial \mathbf{B}}{\partial t} = -\nabla \times \mathbf{E} \, , \tag{1.6}$$

Ohm's law

$$\mathbf{E} + \mathbf{v} \times \mathbf{B} = \mathbf{R} \, . \tag{1.7}$$

These equations must also be supplemented by an appropriate energy equation. In the equations $\mathbf{B}$ is the magnetic induction, normally referred to as the magnetic field, $\mathbf{v}$ is the plasma velocity, $\mathbf{E}$ the electric field, $\mathbf{j}$ the electric current density, ρ the mass density, p the plasma pressure (assumed to be isotropic), $\mathcal{R}$ the gas constant, T the plasma temperature, μ the magnetic permeability, $\mathbf{F}$ denotes other forces which may be present, such as that due to gravity. Note that if the solenoidal constraint holds at some time $t = 0$ then, by taking the divergence of Faraday's law, it remains valid for all time $t > 0$. The term $\mathbf{R}$ in Ohm's law denotes a general non-ideal term. The basic assumption of resistive MHD is that the collisional effects in $\mathbf{R}$ are the dominant ones, with the resistivity normally considered the most important, i.e. $\mathbf{R} = \mathbf{j}/\sigma$ where σ is the electrical conductivity.

It is common to combine (1.4), (1.6) and the resistive form of (1.7), to give the *induction equation*,

$$\frac{\partial \mathbf{B}}{\partial t} = \nabla \times (\mathbf{v} \times \mathbf{B}) + \eta' \nabla^2 \mathbf{B} \tag{1.8}$$

where $\eta' = 1/(\mu\sigma)$ is the magnetic diffusivity. In this thesis we will frequently label $\eta = 1/\sigma$, a common, and perhaps misleading, notation in the literature. In obtaining the induction equation, the magnetic diffusivity has been taken to be uniform. Generally, however, the conductivity is expected to vary in space through a dependence on the magnetic field and the plasma temperature. We will often take a spatially dependent conductivity in this thesis and so do not work directly from the induction equation, but use it here to infer important general properties of solar and astrophysical plasmas. If the term $\eta' \nabla^2 \mathbf{B}$ in (1.8) is neglected we obtain the *ideal* induction equation which may be combined with the equation of mass continuity, (1.1), to give

$$\frac{D}{Dt} \left(\frac{\mathbf{B}}{\rho} \right) = \left(\frac{\mathbf{B}}{\rho} \right) \cdot \nabla \mathbf{v}.$$

The equation for the evolution of a material line element is

$$\frac{D}{Dt} \left(\mathbf{dl} \right) = \mathbf{dl} \cdot \nabla \mathbf{v} \, ,$$

and so we deduce that in the ideal limit the magnetic field lines move as if *frozen* into the plasma; this is Alfvén's theorem. If, however, the advective term $\nabla \times (\mathbf{v} \times \mathbf{B})$ is neglected, then the induction equation reduces to a purely diffusive equation.

The ratio of these two terms, in an order of magnitude sense, is termed the *magnetic Reynolds number*, R_m and is a measure of their relative importance:

$$R_m \quad = \quad \frac{|\nabla \times (\mathbf{v} \times \mathbf{B})|}{|\eta' \nabla^2 \mathbf{B}|}$$

$$= \frac{v_0 B_0 / l_0}{\eta' B_0 / l_0^2}$$
$$= \frac{l_0 v_0}{\eta'} .$$

The magnetic Reynolds number is nearly always very large, particularly so in the solar (and astrophysical) case because of the huge spatial scales of the systems. Thus the magnetic field is almost always frozen-into the plasma and field topology is conserved, with important consequences for dynamics. Non-ideal terms may become important if the length scales associated with the problem are small, as is the case for example in thin current sheets. The magnetic field can then slip through the plasma, allowing for reconnection.

Another important dimensionless parameter to help characterise the behaviour of the plasma is the *plasma beta*, β, which is the ratio of the gas pressure to the magnetic pressure:

$$\beta = \frac{2\mu p_0}{B_0^2}.$$

In the majority of the corona β is very much less than unity, which has the effect of inhibiting cross-field transport. Accordingly plasma tends to flow from the chromosphere into the corona along magnetic field lines. Although there are exceptions – regions with very high temperature but low magnetic field may have values $\beta > 1$ – most models of the coronal field essentially assume $\beta \ll 1$.

1.2   The Need for a Solar Dynamo

Given the importance of the solar magnetic field in determining coronal dynamics it is natural to ask how the field originates. A frozen-in primordial field would decay in a time-scale of around 10^9 years, which is comparable to the age of the solar system. It is, however, very difficult to explain the large-scale temporal variability of the field (manifested for example in the sunspot cycle shown in Figure 1.2) as consistent with such a decay. Magnetic fields also are observed in a multitude of other astrophysical bodies. For example: our galaxy exhibits a large-scale field confined approximately to the plane of its disc (see, for example Han and Qiao, 1994, and references therein); very strong surface magnetic fields have been detected on many other stars (Preston, 1971, Landstreet, 1992, Baliunas et al., 1995); on the planetary scale the magnetic field of the Earth reverses polarity at apparently random intervals in time (e.g. Cox, 1969).

Large-scale solar fields are thought to arise from the operation of a dynamo working in the solar interior, with the first suggestion of self-excited dynamo action being given by Larmor (1919); dynamo models rely on inductive motions of the plasma being able to sustain the field against the continual energy loss through Ohmic dissipation. Field amplification occurs through a stretching of the existing field, with an exemplary model of dynamo action being the *stretch-twist-fold* (STF) dynamo of Vainshtein and Zeldovich (1972), illustrated in Figure 1.3. In the first step of the process, a loop of magnetic field is stretched until it has twice its original length and so, for a frozen-in field, double the field strength. The loop is then twisted and finally one half folded back on the other to create a doubled loop with the same cross section as that of the original loop but now with twice the flux. A mechanism such as this will allow the magnetic energy in an initially smooth field distribution to increase, and indeed the STF dynamo was the
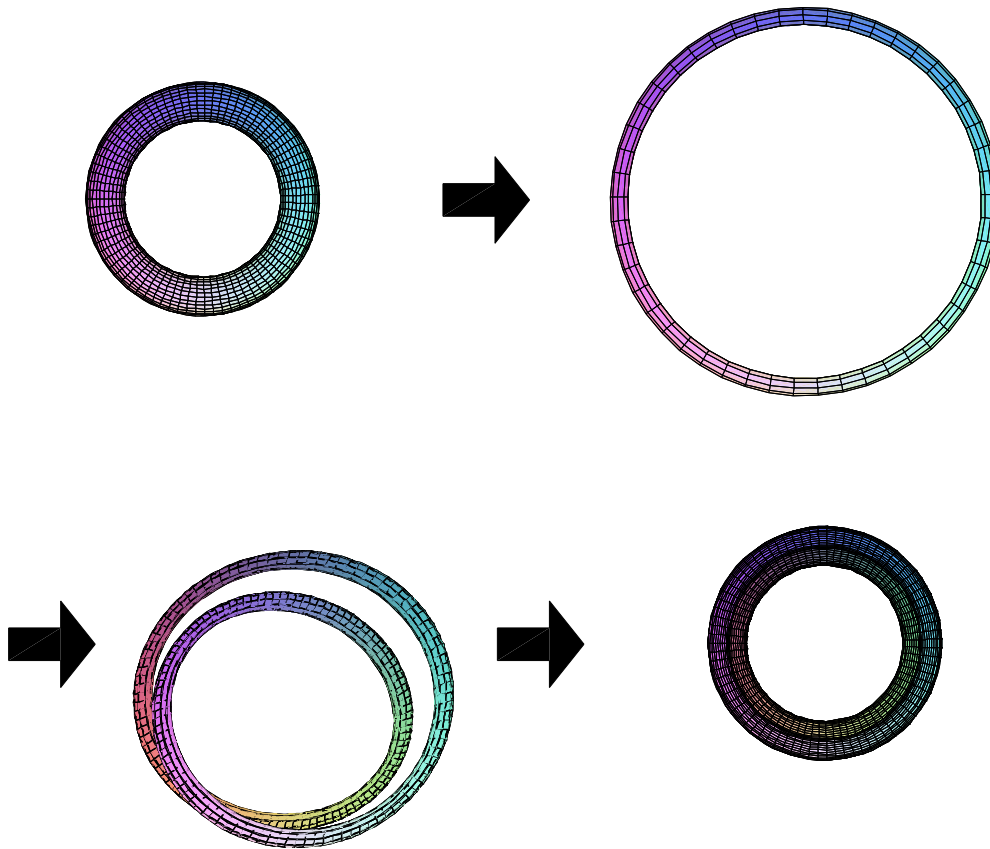
Figure 1.3: Cartoon illustrating the stretch-twist-fold sequence that demonstrates the possibility of exponential growth of the magnetic field. Stretching an incompressible closed flux tube to twice its original length reduces its cross section by half. Twisting and folding gives a tube with twice the flux and the same original cross section.

first example of a *fast* dynamo, one for which the growth rate of a magnetic field remains positive as the magnetic Reynolds number approaches infinity (with other dynamos being classed as *slow*). However, the model ignores dissipative effects, failing to take into account the strong field gradients that may arise in the process (particularly at large times) and allow diffusive effects to become important. In a more realistic dynamo model, the precise balance between driving and diffusion must be considered.

The field is normally decomposed into its toroidal (i.e. longitudinal) and poloidal (i.e. contained in meridional planes) components and the dynamo problem then formulated in two parts: generation of a toroidal field from the pre-existing poloidal field and generation of a poloidal field from the pre-existing toroidal field. The first conversion (poloidal $\rightarrow$ toroidal) is now accepted to be due to a drawing out (and so amplification) of the poloidal field by the Sun's differential rotation, the *omega effect*. The second conversion process (toroidal $\rightarrow$ poloidal) is significantly more controversial, with no one mechanism being (as yet) universally agreed upon. There are, in addition, several restrictions on dynamo action in the form of a number of anti-dynamo theorems, the most famous of which (Cowling, 1934) demonstrates that a steady axisymmetric magnetic field cannot be sustained by dynamo action.

As discussed in Chapter 6, there have now been several advances in dynamo theory, beginning with Parker's idea of an $\alpha\Omega$–dynamo operating in the solar convection zone (Parker, 1955). Although much of the work has side-stepped the difficulty of the nonlinear back-reaction on the flow by the Lorentz force by discussing only the *kinematic* problem (in which the flow is prescribed and the time variation of the magnetic field deduced) it has, nevertheless, shown that dynamos can work.

Parker (1955) suggested that non-axisymmetric small-scale helical convective motions could twist toroidal field into poloidal loops, with the net effect being the production of a large-scale poloidal field. This mechanism is classically known as the *alpha effect* although, both in this thesis and some of the literature, the term is also used to denote any general toroidal to poloidal conversion mechanism. A significant step forward in the mathematical foundations of this theory came with the introduction of *mean-field electrodynamics* (Steenbeck et al., 1966). Here the magnetic field, $\mathbf{B}$, and flow, $\mathbf{v}$, are written in terms of mean ($\mathbf{B}_0\left(\mathbf{x},t\right)$, $\mathbf{V}_0\left(\mathbf{x},t\right)$) and fluctuating components ($\mathbf{b}_0\left(\mathbf{x},t\right)$, $\mathbf{v}_0\left(\mathbf{x},t\right)$) where the mean fields vary on length-scales much larger than those of the fluctuating parts. An averaging procedure is taken over intermediate length-scales and so

$$\mathbf{B}\left(\mathbf{x},t\right) = \mathbf{B}_0\left(\mathbf{x},t\right) + \mathbf{b}\left(\mathbf{x},t\right), \quad \mathbf{V}\left(\mathbf{x},t\right) = \mathbf{V}_0\left(\mathbf{x},t\right) + \mathbf{v}\left(\mathbf{x},t\right),$$

where $\langle\mathbf{v}\rangle = \langle\mathbf{b}\rangle = 0$ (if $\langle.\rangle$ denotes averages). Under these conditions, the induction equation, (1.8), can be written in terms of mean and fluctuating parts, with the equation for the mean field being given by

$$\frac{\partial\mathbf{B}_0}{\partial t} = \nabla \times \left(\mathbf{V}_0 \times \mathbf{B}_0\right) + \nabla \times \boldsymbol{\varepsilon} + \eta'\nabla^2\mathbf{B}_0,$$

where $\boldsymbol{\varepsilon} = \langle\mathbf{v} \times \mathbf{b}\rangle$ is a mean electromotive force (e.m.f.) induced by the fluctuating components. The e.m.f. must then be expressed in terms of the mean field $\mathbf{B}_0$ so that closure of the system is obtained. A suitable relation, obtained by considering also the equation for the fluctuating field, the separation of scales and assuming the fluctuating flow $\mathbf{v}$ is isotropic, is given by

$$\boldsymbol{\varepsilon} = \alpha\mathbf{B}_0 - \beta\nabla \times \mathbf{B}_0,$$

which, in turn, gives the evolution equation for the mean field as

$$\frac{\partial\mathbf{B}_0}{\partial t} = \nabla \times \left(\mathbf{V}_0 \times \mathbf{B}_0\right) + \nabla \times \alpha\mathbf{B}_0 + \left(\eta' + \beta\right)\nabla^2\mathbf{B}_0$$

We see that β reflects a turbulent enhancement of the magnetic diffusivity and α (hence the 'alpha effect') parameterises a source-term for the mean field. If the fluctuating velocity field is not reflectionally symmetric then α will be non-zero; this lack of reflectional symmetry is key for the development of dynamo action. In mean-field simulations both α and β are given prescribed dependencies on the mean field with α typically falling-off in the presence of strong fields (this algebraic α-*quenching* represents the inefficiency of the alpha effect on strong magnetic fields). Mean-field theory has enjoyed much success in reproducing many of the observed large-scale solar magnetic features (such as the butterfy diagram) – for a review, for example, Hoyng (2003).

Alternative mechanisms for the regeneration of poloidal- from toroidal field have also been proposed,

such as the production of poloidal flux through the decay of bipolar active regions invoked in the Babcock-Leighton mechanism (Babcock, 1961, Leighton, 1969). These models utilize the same poloidal to toroidal conversion mechanism as Parker's approach but now the alpha-effect manifests itself as a surface phenomenon. Solar observations show that bipolar active regions appear on the photosphere with a systematic tilt (Joy's law) and therefore have a net north-south dipole vector. In time the active regions decay or diffuse away and in the process the leading polarities migrate toward the equator whilst the trailing polarities move toward the poles. The opposite polarities that are transported equatorward from the Northern and Southern hemispheres cancel by the equator. Crucially, the polarities that move poleward act to replace the existing poloidal field and reverse it sign. Thus the decay of bipolar active regions takes the role of a surface α-effect.

A brief discussion of the sign of the alpha-effect in these various models will also be helpful. Parker (1955) deduced that the sign of the product of α and the vertical differential rotation gradient must be negative in the northern hemisphere if the observed equatorward migration of active regions is to take place. This sign rule holds even if the differential rotation gradient and the alpha-effect are in different layers (Moffatt, 1978, Section 9.7). Through helioseismology the differential rotation gradient at low latitudes is known to be positive. In the framework of mean-field theory we expect a negative alpha-effect to act in the lower part of the convection zone. Cyclonic convection occurs throughout the convection zone. However, considering the observed differential rotation profile, if this type of dynamo action is to lead to the observed equatorward migration of active regions then we require a negative alpha effect in the Northern hemisphere. Such a negative alpha effect is believed to occur in the lower part of the convection zone only. In Babcock-Leighton models however, the alpha-effect is concentrated in the surface layers where α must be positive (since the trailing polarities of active regions are at higher latitudes on the photosphere than the following polarities). The problem of achieving an equatorward progagating dynamo wave is overcome by including a meridional flow with a short timescale in the model – and anyway Babcock-Leighton models must invoke such a flow for the transport of magnetic flux between the separated source layers.

It is likely to be some time before a full understanding of the dynamo process is reached – current analytical modelling tends to be based on somewhat tentative foundations, and numerical simulations far from being able to resolve the huge range of length- and time-scales inherent to the process. In this thesis (Chapters 6 and 7) we explore an alternative and complementary approach to traditional dynamo modelling and construct simple mathematical models that are expected to have a similar underlying structure to that of the full system. Their very simplicity allows us to fully explore their dynamics and so make inferences about the properties of both solar and stellar dynamos, while their physical justification is sufficiently general that they may be applied to a wide variety of the proposed dynamo mechanisms.

1.3   Magnetic Reconnection in Two Dimensions

The small-scale amplification of the field is clearly essential to the dynamo process, but does not help in determining how the observed large-scale fields built up from the small-scale ones, nor how the large-scale toroidal field breaks up. Magnetic reconnection must be responsible for both this large-scale generation and for the localised break-up of the toroidal field. More widely speaking, reconnection is a fundamental

plasma process that is responsible for a wide range of phenomena, being of importance in solar, space, astrophysical and laboratory plasmas, for example in:

- Heating the corona to its multi-million degree temperatures (e.g. Parker, 1983).

- Sudden violent events such as solar flares (Parker, 1963) and CMEs and the corresponding events on other stars.

- The Earth's magnetosphere (where, uniquely for non-terrestrial events, in-situ spacecraft observations at reconnection sites have been made) as it interacts with the solar wind (Xiao et al., 2006), and similarly in other planetary magnetospheres (Huddleston et al., 1997).

- Magnetic flux reduction in gravitationally collapsing protostellar clouds, as part of the process of star formation (Norman and Heyvaerts, 1985, Pringle, 1989).

- Accretion disks, where reconnection is primarily invoked as a mechanism for supplying the internal stresses that are required for efficient transfer of angular momentum (Eardley and Lightman, 1975, Tout and Pringle, 1992) but also in, for example, the time variability of accretion and the corresponding radiation (Rastaetter and Neukirch, 1997).

- Explaining the non-thermal particle populations present in extragalactic jets (Romanova and Lovelace, 1992).

- The laboratory, particularly in fusion devices. Reconnection is thought to be the cause of the sawtooth oscillations that play an important role in determining the confinement characteristics of tokamak fusion plasmas (Porcelli et al., 1996) and lead to major disruption of the device. Conversely reconnection is useful in spheromaks where it allows the seed field to be restructured to create a stronger confining field.

Early models of reconnection were strictly two-dimensional (with the field confined to a plane). Although this is a very special case – occurring only at an X-type (hyperbolic) null point and in the stationary situation restricting the electric field to being uniform (with important consequences as we will see later) – it has, nevertheless, informed much of our understanding of the topic. It is, therefore, worthwhile to summarize briefly some of the most important aspects of the theory.

The Sweet-Parker model (Sweet, 1958, Parker, 1957) is an order-of-magnitude analysis in which a current sheet (with length equal to the global external length-scale) lies between oppositely directed magnetic fields (see Figure 1.4). The model is stationary so that the current sheet is maintained and therefore the inflow must exactly counter the outward magnetic diffusion of the sheet. In addition, magnetic flux is assumed conserved between inflow and outflow. Finally, the plasma is taken to be accelerated to the Alfvén speed by the Lorentz force (which sets the width of the current sheet under mass conservation and incompressibility conditions).

In 2D, the rate of reconnection is given by the value of the electric field at the null point and measures the rate at which flux passes through the null – i.e. at which it is transferred between topologically distinct regions (see Chapter 2). The electric field is traditionally normalised to a characteristic electric field and
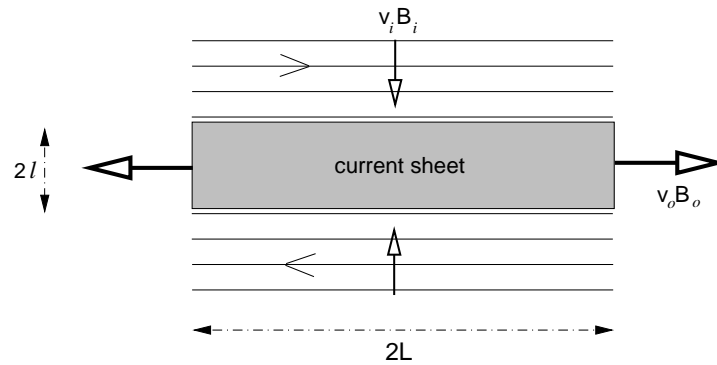
Figure 1.4: The Sweet-Parker mechanism for 2D reconnection.
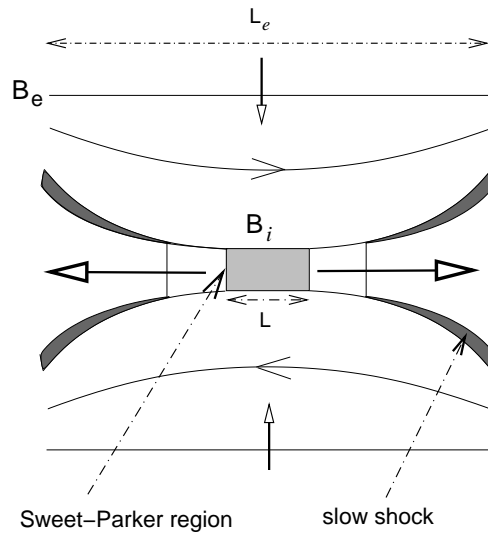
Figure 1.5: The Petschek mechanism for 2D reconnection.

the resultant Alfvén Mach number used as a dimensionless quantitative measure of the reconnection rate. Reconnection models then determine how the Alfvén Mach number scales with the Lundquist number (or global magnetic Reynolds number), S.

Under the above assumptions, the reconnection rate in the Sweet-Parker model is given by

$$M_{Ae} = \frac{1}{\sqrt{S}},$$

and is therefore, in practice, very small in the corona due to the very high Lundquist numbers there. In order to account for the very fast energy release of solar flares we need an alternative mechanism, a *fast* mechanism for which the reconnection rate is very much more than the Sweet-Parker rate.

Petschek (1964) suggested that slow MHD waves would significantly decrease the size of the diffusion region and, accordingly, increase the rate of reconnection. Thus in the model the length of the diffusion region may be considerably smaller than the global external length-scale. Four standing slow magnetoa-coustic shock waves are placed at the boundaries of the plasma outflow regions (see Figure 1.5) and allow for an additional mechanism for the conversion of magnetic energy into thermal and kinetic energy. The inflow region itself is current-free with no external sources present and the Sweet-Parker model is employed for the diffusion region, the average properties of which are matched to the external flow region as far as is allowed (Vasyliunas, 1975). From the experience gained by many numerical simulations it seems likely that the configuration only appears when the resistivity is enhanced within the diffusion region. The maximum reconnection rate is given by

$$M_{Ae} = \frac{\pi}{8 \ln (S)}$$

which, due to the logarithmic dependence on S is, for typical coronal parameter values, several orders of magnitude greater than the Sweet-Parker rate.

Chapter 2

Background to 3D Reconnection
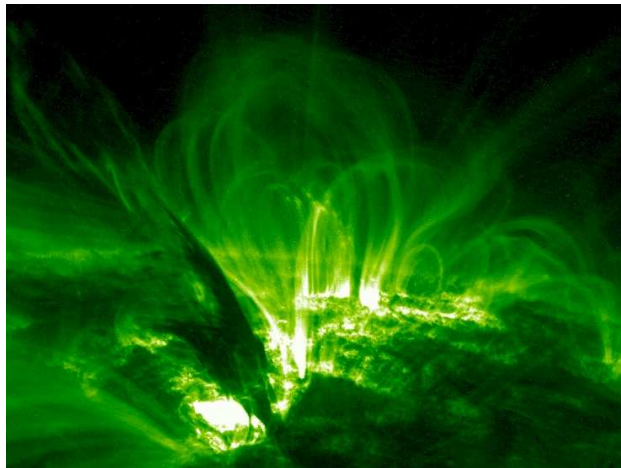
Figure 2.1: Three-dimensional structure of an M1.8 flare observed in TRACE 171 Å on 21st March 2001 in Active Region 9373, starting at 02:28UT, and peaking in X-rays at around 02:37UT.

Although a substantial literature exists describing the nature of two-dimensional reconnection, an increasing number of observations now show that the solar magnetic field is enormously complex (see Figure 2.1 for an example of such a magnetic field structure), and so motivate the need for a full three-dimensional understanding of the problem. Existing three-dimensional reconnection models have already demonstrated the 3D process to be fundamentally different in many respects to the 2D and therefore have only further enhanced this need.

The table on the next page summarizes some of the differences between reconnection in 2D and reconnection in 3D. In this chapter we describe some of these differences in more detail and further discuss some of our present ideas on 3D reconnection.

Property of Reconnection	Two Dimensions	Three Dimensions
Location	Only at an X-type null-point.	Anywhere in space, in the presence or or absence of null-points.
Flux transport velocity	Exists everywhere in space except at the X-point.	In general unique velocity does not exist. Can be replaced by multiple transport velocities.
Change of connectivity	Occurs at the X-point.	Occurs continually and continuously throughout the non-ideal region.
Counterpart reconnecting fieldlines	Unique reconnecting fieldline exists.	Generally no unique counterpart exists.
Fieldline mapping	Discontinuous	Continuous (except at separatrices)
Rate of reconnection	Given by the electric field at the null-point.	Given by maximum integrated parallel electric field across non-ideal region.

2.1 Magnetic Flux Velocities

Schindler et al. (1988) considered how appropriate the ideas on reconnection that had been developed by examining 2D theory are when applied to a general 3D scenario. They concluded that any definition of reconnection should at least be structurally stable and introduced the theory of *general magnetic reconnection* in which reconnection requires only a change in connectivity of plasma elements. A useful mathematical tool that enables us to address changes in plasma element connectivity is the concept of a *magnetic flux transport velocity* (or *flux transporting flow*), as defined by Hornig and Schindler (1996).

Under ideal evolution,

$$\mathbf{E} + \mathbf{v} \times \mathbf{B} = \mathbf{0}, \tag{2.1}$$

holds and the magnetic field is frozen into the plasma, so that the curl of (2.1) gives

$$\frac{\partial \mathbf{B}}{\partial t} - \nabla \times (\mathbf{v} \times \mathbf{B}) = \mathbf{0}. \tag{2.2}$$

One of the consequences of (2.2) is the conservation of magnetic flux (Alfvén's frozen-flux theorem),

$$\int_C \mathbf{B} \cdot d\mathbf{S} = constant,$$

i.e. the flux through a comoving surface C (a surface moving with $\mathbf{v}$) is conserved. This in turn implies the

conservation of magnetic field lines, together with conservation of magnetic nulls and of knots and linkages of field lines. The far reaching consequences of (2.2) on the evolution of the magnetic field stem from the algebraic form of the equation; they make no use of the fact that $\mathbf{v}$ is the plasma velocity. Thus we can ask whether for a general non-ideal evolution,

$$\mathbf{E} + \mathbf{v} \times \mathbf{B} = \mathbf{R}, \tag{2.3}$$

where $\mathbf{R}$ denotes an arbitrary non-ideal term, there could exist a velocity which also yields an equation of the form (2.1). Such a velocity will, in general, differ from the plasma velocity and therefore we write

$$\frac{\partial \mathbf{B}}{\partial t} - \nabla \times (\mathbf{w} \times \mathbf{B}) = \mathbf{0}, \tag{2.4}$$

calling $\mathbf{w}$ a flux transporting velocity. If such a transport velocity can be found then the field is frozen-in with respect to the flux transport velocity and the field topology cannot change.

In a situation governed by the ideal Ohm's law, (2.1), the velocity ($\mathbf{w}$) with which the magnetic field lines may be said to move can be identified with the plasma velocity ($\mathbf{v}$). In more general cases we must first address the question of the existence and uniqueness of the flux transport velocity. For this we integrate (2.4) so that it can be compared with other forms of Ohm's law. The integration yields

$$\mathbf{E} + \mathbf{w} \times \mathbf{B} = \nabla F \,, \tag{2.5}$$

where F is an arbitrary function (a function of integration). Equation (2.5) may be compared with the most general form of Ohm's law, (2.3); if a flux transporting velocity is to exist then we must be able to rewrite (2.3) in the form of (2.5), i.e. $\mathbf{R}$ must be of the form

$$\mathbf{R} = \underbrace{(\mathbf{v} - \mathbf{w})}_{:=\mathbf{u}} \times \mathbf{B} + \nabla F. \tag{2.6}$$

A sufficient condition (provided $\mathbf{B} \neq 0$) to represent $\mathbf{R}$ in form of (2.6), and hence for the existence of $\mathbf{w}$ is

$$\mathbf{B} \cdot \nabla F = \mathbf{B} \cdot \mathbf{R} \equiv \mathbf{B} \cdot \mathbf{E}. \tag{2.7}$$

If $\mathbf{E} \cdot \mathbf{B} = 0$, that is, if $\mathbf{R}$ is perpendicular to $\mathbf{B}$, then clearly this equation can be solved ($F \equiv 0$ being a trivial solution). Important examples of this situation are the resistive two-dimensional case ($\mathbf{R} = \eta \mathbf{j}$), and the case when $\mathbf{R}$ represents a Hall term: $\mathbf{R} = (ne)^{-1} \mathbf{j} \times \mathbf{B}$. In this last example the transport velocity may be identified with the electron bulk velocity.

A consideration of the 2D case demonstrates some key properties of reconnection in 2D. Here (taking $F = 0$) the flux transporting flow, $\mathbf{w}$, is given by

$$\mathbf{w} = \frac{\mathbf{E} \times \mathbf{B}}{B^2} \tag{2.8}$$

and exists everywhere except at any null-points (zeros of $\mathbf{B}$) where $\mathbf{R}$ is non-vanishing. In an ideal region the flux transport velocity $\mathbf{w}$ will, up to its parallel component, coincide with the plasma velocity $\mathbf{v}$ (note that (2.8) is actually an equation for the perpendicular component of $\mathbf{w}$ but that the parallel component may

be assumed to be zero). However, at null points a singularity in the flux transport velocity will exist in general, with the singularity at X-type null-points being the relevant one for reconnection. Locally about the X-point the flow $\mathbf{w}$ will have a stagnation type structure; magnetic flux is transported by the flow into and away from the null with the singularity in $\mathbf{w}$ at the null itself representing the cut and re-joining (reconnection) of the flux there. The rate at which this occurs measures the reconnection rate and is given by the electric field strength at the null (see, for example Schindler, 2007, p. 274).

Moving back to more general cases, equation 2.7 can also be solved if there exists a surface that all the field lines cross exactly once (which we call a *transversal surface*). Then we can integrate (2.7) along magnetic field lines in order to deduce F. Parameterizing the magnetic field line by $\mathbf{x}(s)$ and integrating $R_{\parallel}$ along the field line from the point $\mathbf{x}(0)$ on the transversal surface (C) we obtain

$$F(\mathbf{x}) = \int_0^s R_{\parallel}\mathrm{d}s + F(\mathbf{x}(0)), \quad \frac{\mathrm{d}\mathbf{x}(s)}{\mathrm{d}s} = \frac{\mathbf{B}}{|\mathbf{B}|}; \quad \mathbf{x}(0) \in C; \quad R_{\parallel} = \frac{\mathbf{R}\cdot\mathbf{B}}{|\mathbf{B}|}. \tag{2.9}$$

The solution may not exist within the whole domain under consideration and, in addition, there are situations where (2.7) has no solutions and so no flux transporting velocity exists. For example, if there are closed magnetic field lines in the domain with

$$\oint \mathbf{R}_{\parallel}\mathrm{d}s \neq 0,$$

then the integration (2.9) would fail. In addition, boundary conditions on F or $\mathbf{w}$ can prevent the existence of a solution, precisely the situation in three-dimensional reconnection. During 3D magnetic reconnection at an isolated non-ideal region, a flux velocity ($\mathbf{w}$) satisfying $\mathbf{w} = \mathbf{v}_{\perp}$ on the entire boundary of the non-ideal region does not exist in general (Hornig and Priest, 2003, Priest et al., 2003). Instead it can be replaced by a pair of flux velocities, $\mathbf{w}_{in}$ and $\mathbf{w}_{out}$, say. The behaviour of field lines anchored to one side of the non-ideal region is described by $\mathbf{w}_{in}$, where $\mathbf{w}_{in}$ coincides with $\mathbf{v}$ for flux *entering* the non-ideal region. Similarly, the behaviour of field lines anchored on the other side of the non-ideal region may be described by $\mathbf{w}_{out}$ where $\mathbf{w}_{out}$ coincides with $\mathbf{v}$ where flux *leaves* the non-ideal region. In the 3D case the two flux velocities will not coincide within the diffusion region and this property allows us to deduce some of the fundamental features of 3D reconnection.

In a general 3D situation, as a flux tube moves such that it partly enters the non-ideal region, the two flux velocities $\mathbf{w}_{in}$ and $\mathbf{w}_{out}$ can be used to track the part of the flux tube *entering* the non-ideal region and the part *leaving* the non-ideal region. Taking the projections into the non-ideal region of the flux velocities, their difference represents a splitting of the two tubes as they enter the non-ideal region. Whilst the tube continues to move with the velocity $\mathbf{w} = \mathbf{v}$ in the ideal region, the velocity within the non-ideal region depends on whether $\mathbf{w}_{in}$ or $\mathbf{w}_{out}$ is used as a tracer. These two flux velocities will differ everywhere in the non-ideal region, signifying a continual change in the magnetic connectivity of the flux passing through the boundary of the non-ideal region. The implication is that plasma elements in the ideal region that lie on a field line passing through the non-ideal region will be connected to different plasma elements on the other side of the non-ideal region at every moment in time, in other words every field line passing through the non-ideal region continually changes its magnetic connections. We may continue to track the plasma elements that lay on the initial flux tube and remain in the ideal region. After some time these will lie on an
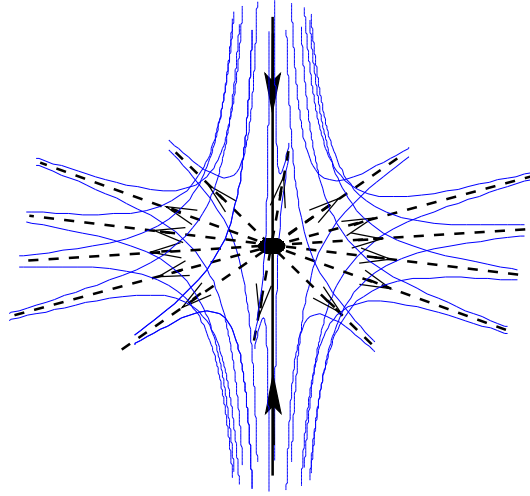
Figure 2.2: Structure of the magnetic field near a potential three-dimensional null-point. The solid black lines marks the *spine* and the dashed black lines the *fan* surface.

ideal flux tube no longer be associated with the reconnection process. However, plasma elements associated with the $\mathbf{w}_{in}$-flow and those of the $\mathbf{w}_{out}$-flow will not generally become again magnetically connected (i.e. 'rejoin').

We will make extensive use of flux velocities in Chapters 3 and 4 to describe the nature of the 3D reconnection processes under consideration. A further discussion on the existence and uniqueness of $\mathbf{w}$, together with descriptions of the behaviour of magnetic flux in purely diffusive non-ideal situations, can be found in Wilmot-Smith et al. (2005b).

2.2   Location of Reconnection

Compared with the two-dimensional case, a much wider class of reconnection scenarios may be found in three-dimensional geometries. As already discussed, in 2D, X-points (hyperbolic null points) and O-points (elliptic null points) are the only generic null points of the magnetic field and it is only possible for reconnection to occur at an X-point, where the flux transport velocity, $\mathbf{w}$, is of a stagnation type close to the null point and has a hyperbolic singularity at that location. Additionally, generation and loss of magnetic flux can both occur at O-points depending on the nature (the direction) of the flux transport velocity near such a point. Moving into in three-dimensions, reconnection may be associated with the presence of a null-point but may also occur when no null-points are present; the non-existence of a unique and non-singular flux transport velocity (as discussed in the previous section) and accordant change in magnetic connection no longer relies on the presence of a zero of the magnetic field.

The structure of three-dimensional null-points is described by, for example, Parnell et al. (1996). The local structure of the field at an example of a generic 3D null is shown in Figure 2.2. The *spine* of the

null-point is an isolated pair of field lines which either diverge or converge from opposite directions onto the null. The *fan* plane consists of a family of field lines that branch out-of or into the null. The field lines in the fan plane form a *separatrix surface* that divides regions of differing flux connectivity. If two separatrix surfaces intersect, then their line of intersection will divide four regions of differing flux connectivity. The line is known as a *separator*.

At isolated null-points two types of reconnection have been identified according to whether the current is aligned with the spine of the null (Pontin et al., 2004) or the fan of the null (Pontin et al., 2005b). The models described in Pontin et al. (2004) and (Pontin et al., 2005b) are *kinematic* ones in which the equation of motion is neglected, the magnetic field prescribed and the plasma velocity deduced from Ohm's law (so the term kinematic is used here in a slightly different sense to the traditional use in dynamo theory). In the analysis of reconnection with the current aligned with the spine of the null (Pontin et al., 2004) a simple spiral null point was assumed together with a resistivity localised about the null. The resultant reconnecting plasma flow is found to be non-zero only within the envelope of field lines linking the non-ideal region, rotational in its nature and crossing neither the spine of the null nor the fan plane. In the analysis of Pontin et al. (2005b) a 3D null was taken with a current parallel to the fan plane (and so the spine of the null is not perpendicular to the fan plane) and, again, a localised profile for the resistivity. The reconnecting plasma flow deduced is found to transport magnetic flux across both the spine and the fan of the null, so, in the latter case, transferring flux between domains.

If multiple null points are present in a domain then magnetic separators will be present. Separators form a 3D analogue of the 2D X-point (Lau and Finn, 1990) since they lie at the intersection of four flux domains and, in addition, the field in a perpendicular cross-section has an X-type structure. It is thought that currents will tend to accumulate along separators (Sweet, 1969, Longcope and Cowley, 1996), enabling reconnection to take place there (Lau and Finn, 1990, Priest and Titov, 1996). Several numerical experiments have explored separator reconnection (Galsgaard and Nordlund, 1997, Parnell and Galsgaard, 2004, Haynes et al., 2007) in some detail and observational evidence has been presented by Longcope et al. (2005).

Magnetic reconnection in three-dimensions can also occur in the absence of a null-point. The considerations of Section 2.1 show that reconnection may take place whenever any non-ideal terms, such as current concentrations, that can lead to a change in the connectivity of plasma elements are present. An example of reconnection in the absence of a null-point, *non-null* reconnection, was given by Hornig and Priest (2003). Since much of the work in this thesis also discusses non-null reconnection the findings of Hornig and Priest (2003) are summarised in the Section 2.4.

The process of magnetic reconnection changes the topology of the magnetic field. The change in topology itself may be associated with topological features such as magnetic null points and separators. Then reconnection may, for example, transfer flux between topologically distinct domains, or create new, distinct, flux domains. However, in three-dimensions a change in magnetic topology may take place even when no such features are present. A simple conceptual example is illustrated in Figure 2.3. The pre- and post-reconnection states in this example are topologically distinct – they cannot be continuously deformed into each other – but no null points have been involved in the 3D process. Therefore, to see these topological changes we will, in general, need to know the magnetic configuration of the global system, in which no
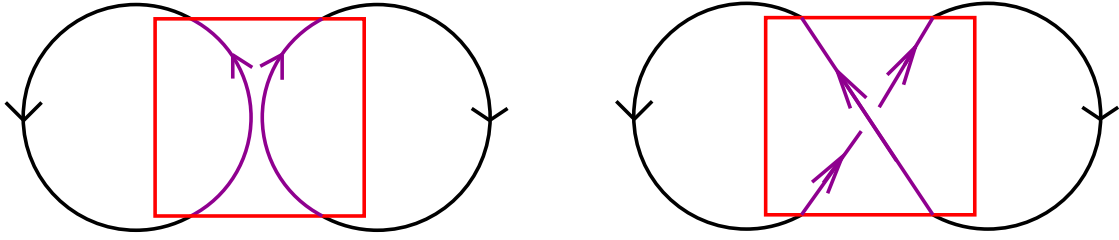
Figure 2.3: Illustrative example of a situation in which a global change in topology can occur in a 3D domain with no magnetic null points. Two magnetic flux loops exist before reconnection (some particular field lines being illustrated in the left-hand image) but only one flux loop after reconnection (right-hand image). Looking only at a subsection of the process (within the red-box) the change in topology is not evident.

magnetic flux passes through the boundary, and not just an isolated part of the configuration. Such isolated regions are, however, exactly the systems typically analysed in both two and three-dimensional models of magnetic reconnection. Fitting these local models into the global process involves extrapolating the field outside of the model domain (which might be, for example, a cuboid numerical box). However, regardless of the extrapolation used, there will, during the reconnection process, be some change in the topology of the global system. Figure 2.3 provides an illustrative example of the importance of the global system in reconnection.

2.3 Magnetic Reconnection Rates

As previously discussed, reconnection in two-dimensions takes place at an X-type null-point and transfers magnetic flux between topologically distinct domains. The reconnection rate in 2D is a measure of the rate at which flux is transferred between the distinct domains and this rate in turn is given by the value of the electric field at the null point. Traditionally, the rate is expressed in terms of the dimensionless quantity the Alfvén Mach number through the use of a normalisation of the null point electric field to some characteristic field.

Given the previously mentioned differences between 2D and 3D reconnection the question arises as to how the reconnection rate should be defined, measured and interpreted in 3D? These are still partly open questions. We begin by discussing the case of non-vanishing magnetic field and an isolated non-ideal region (D) in an otherwise ideal environment (Hesse and Schindler, 1988).

For this, consider, as illustrated in Figure 2.4, an isolated non-ideal region D (shaded) with non-vanishing magnetic field and a loop integral where the loop path is along a magnetic field line (shown in red) passing through D and a material line (blue) in the ideal environment. Integrating the electric field, $\mathbf{E}$, along this loop and using Faraday's law (1.6) together with Stokes' theorem gives

$$\oint_C \mathbf{E} \cdot dl = \int_S \nabla \times \mathbf{E} \cdot \mathrm{d}\mathbf{A} = -\frac{d}{dt} \int_S \mathbf{B} \cdot \mathrm{d}\mathbf{A}. \tag{2.10}$$

Since the material line is in the ideal region, the electric field along that section of the loop must vanish
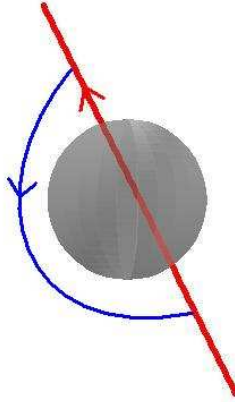
Figure 2.4: Example path taken for the loop integral given by equation (2.10) to demonstrate the relationship between a non-zero integrated parallel electric field across a localised non-ideal region and magnetic reconnection. The path is taken along a magnetic field line (shown in red) passing though the non-ideal region (shaded) and a comoving line (shown in blue) in the ideal region.

and the only contribution to the loop integral comes from that along the field line passing through D. We therefore deduce that

$$\frac{d}{dt} \int_S \mathbf{B} \cdot d\mathbf{A} = - \int E_\parallel \, dl,$$

where the line l denotes the field line taken through D, and so if the integrated parallel electric field along this magnetic field line is non-zero then there must be a change in the magnetic flux enclosed by the loop. The rate of reconnection is then given by the maximum value of this integral across D (and is given a positive value since direction of the normal component to the surface is arbitrary):

$$\frac{d\Phi_{rec}}{dt} = \left| \int E_\parallel \, dl \right|. \tag{2.11}$$

Thus while the expression for the 2D reconnection rate was given by the electric field at a point in 3D we have the integrated electric field along a line. The formulation (2.11) is consistent with the 2D one with the reconnecting flux in 2D being the 3D flux per unit length in the invariant direction.

Similarly, in a system with reconnection taking place at a magnetic separator, the rate of reconnection is given by the difference in electric potential between the ends of the separator (Longcope and Cowley, 1996). When multiple separators are present in a domain the difference in potential across each must be taken into account. Such a system must be carefully analysed to determine the total reconnected flux since it may allow for flux to be transferred simultaneously into and out of a flux domain at different boundaries (Parnell et al., 2007).

There are several circumstances for which the rate of reconnection is unknown. Examples include systems where the non-ideal region contains closed flux loops and in which the the non-ideal region is not isolated within the domain considered. In addition, questions regarding the rate of reconnection are often motivated by energetic considerations in real systems and little is known about how the rate of reconnection might relate to any release of magnetic energy in a 3D system.

2.4 An Isolated Non-Null Reconnection Process

In Chapters 3 and 4 we consider non-null reconnection. Much of this work builds on the investigations of Hornig and Priest (2003) and so we now discuss their main findings.

In most of the previous models of reconnection, the non-ideal region is bounded only in two-dimensions and extends to infinity in the third dimension. However, in a realistic model for astrophysical plasma processes, the non-ideal region should be localised in all three dimensions since this is the generic situation in astrophysical plasmas which have length scales along the magnetic field that tend to be much larger than the mean free path.

Hornig and Priest (2003) analysed such a situation in a region of non-zero magnetic field, placing particular emphasis on the evolution of magnetic flux. The model is a kinematic one with *kinematic*, in this context, referring to the (non-traditional) situation where a magnetic field of a certain form is imposed and a plasma velocity deduced using Ohm's law. Since the equation of motion is neglected the question as to whether the field can be sustained by the plasma flow is ignored.

The prescribed magnetic field in the model is a linear X-type configuration in the xy-plane with a uniform field component in the third (z) direction and so results in a uniform current. Thus, in order to obtain a localised non-ideal region, a 3D localisation of the resistivity is imposed. In a realistic situation it is expected that finite regions of intense current concentration will be the main cause of such a localisation and that it may be reinforced when the resistivity is enhanced by current-driven microinstabilities. In the model however, the localisation is achieved in this way in order to make analytical progress.

The authors noted that in a general three-dimensional situation, for a specified magnetic field, Ohm's law may be decomposed into a particular non-ideal solution and an ideal solution:

$$\mathbf{E}_{non-id} + \mathbf{v}_{non-id} \times \mathbf{B} = \eta\mathbf{j},$$
$$\mathbf{E}_{id} + \mathbf{v}_{id} \times \mathbf{B} = \mathbf{0}\,.$$

The non-ideal, or *particular* solution must be deduced from the imposed magnetic field. The localisation of $\eta\mathbf{j}$ results in the flows associated with the particular solution being rotational in nature. Identifying the flux tube consisting of all the field lines linking the non-ideal region as a HFT, the non-ideal plasma flows are confined to within the HFT and are rotating in opposite senses above and below the non-ideal region itself, as illustrated in Figure 2.5. Thus the particular solution affects only the flux within the HFT and all the field lines contained within it are continually changing their connections.

The kinematic nature of the analysis now allows for *any* ideal flow to be superimposed onto the particular rotational solution. Hornig and Priest (2003) chose, for two reasons, to examine the effect of an ideal stagnation flow. The first reason is that such flows are to be expected if thin current sheets are to be built up and so allow reconnection to begin. The second reason is that a stagnation flow can transport flux into and away from the non-ideal region (and the HFT linking the non-ideal region), this property allowing for the effect of the reconnection process on the magnetic flux evolution to be seen on a much larger scale. Whether the rotational or stagnation component of the flow is dominant within the HFT will depend on
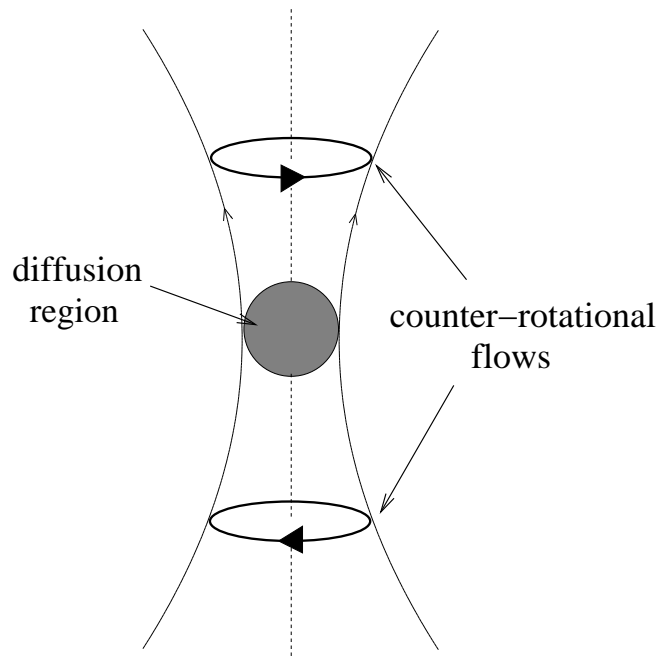
Figure 2.5: Cartoon illustrating the counter-rotational flows (thick solid lines) in the pure solution of Hornig and Priest (2003). The hyperbolic flux tube (HFT) which encloses the localized non-ideal region (shaded) is bounded by the thin solid lines.

their relative strengths, but in either case some flux will be carried by the stagnation flow into the HFT, where reconnection will take place, and then transported away from the region. The combination of the two flows, known as *composite solutions* may therefore show more similarities to the case of classical 2D reconnection than the particular solutions alone. Thus although the rate of reconnection in both the particular and composite cases is the same (with the ideal solution having no associated parallel electric field), the effect of the reconnection in terms of magnetic flux evolution is quite different.

2.5   Aims

The analysis of Hornig and Priest (2003) left open some important questions. One key feature of the analysis is the ability to impose an arbitrary ideal solution on the non-ideal particular solution. Since this freedom is not present in the 2D kinematic case it may be an inherent feature of a 3D process. However, it may also be the case that in a fully 'dynamic' analysis in which the momentum equation is also considered, the freedom disappears since the flows $\mathbf{v}_{non-id}$ and $\mathbf{v}_{id}$ must also jointly satisfy that equation (Eq. 1.2). In addition, in order to make analytical progress, the solutions were obtained by imposing a localised form for the resistivity (while the electric current was uniform) so that a localised non-ideal region could be attained. It is then natural to ask whether solutions found will differ if the localised non-ideal region is due to a localised current term instead.

This thesis aims to examine further the nature of 3D non-null reconnection and to address these questions, at least in part. We begin in Chapter 3 by attempting to address the first question, of freedom within 3D reconnection solutions, by building a fully dynamic 3D model. Several of the assumptions taken are the same as those of Hornig and Priest (2003); a stationary solution in a non-null field geometry with a non-ideal region localised in all 3D. We then carry out a perturbation expansion that allows for a splitting of the variables to be made in such a way that comparisons may be drawn with the particular and composite solutions of Hornig and Priest (2003). This enables some circumstances under which the freedom of imposing ideal flows on reconnection solutions exists.

In Chapter 4, we analyse reconnection in a flux-tube where the current-concentration is localised in all three-dimensions, reverting to a kinematic analysis in order to do so. The model uses an elliptic rather than hyperbolic field geometry; whilst the imposed magnetic field of Hornig and Priest (2003) had an X-type structure in the xy-plane and a uniform third component, our model has an O-type structure in the xy-plane (and, again, a uniform third component). The reconnection scenario described corresponds to a situation in which the footpoints of the flux-tubes are spun in opposite directions and the counter-spinning motion results in a localised reconnection region in the centre middle portion of the tube. In the chapter we first carry out an order-of-magnitude analysis that allows an intuitive understanding of the process to be built up before confirming these estimates with a quantitative model.

In Chapter 5 we build on the approach of Chapter 4, again analyzing reconnection in flux-tubes where spinning footpoint motions are imposed but now taking two initially intertwined tubes. The process is examined by means of a 3D MHD numerical experiment and, again, particular emphasis is placed on the evolution of magnetic flux within the domain.

Chapter 3

Dynamic Non-Null Reconnection

As discussed in previous section, the analysis of Hornig and Priest (2003) shows several new features of 3D reconnection but it is a kinematic one – the effects of the equation of motion are neglected. The aim of this chapter is to build upon their work by investigating an isolated reconnection process and including the equation of motion in the analysis, so that the model is a fully 'dynamic' one. We wish to determine whether the additional freedom to impose an ideal flow on the particular solution arises through the neglect of the momentum equation, or whether it is an inherently 3D effect. The MHD numerical experiments of Pontin et al. (2005a) suggest the latter. In that paper 3D simulations of a non-null reconnection process with a localised non-ideal region are described. Several of the features of the kinematic analysis are observed, in particular a rotational background component to the plasma flow that is of opposite sense on either side of the non-ideal region. Field-lines linking the non-ideal region are found to be continuously changing their connnections.

We take the set of resistive MHD equations (neglecting the energy equation), assume stationarity and imcompressibility, and carry out a perturbation expansion of the equations that allows models of a 3D reconnection process in the absence of a null-point to be built. The assumptions taken in making the expansion are such as to allow Ohm's law at the zeroth and first orders of the expansion to be written as ideal and non-ideal equations respectively. These equations are coupled together through the momentum equation and so the extent to which this coupling restricts the independence of the zeroth and first order flows (the analogue of the ideal and non-ideal flows in the model of Hornig and Priest, 2003) can be considered.

We begin in Section 3.1 by introducing the expansion technique; the MHD equations are written in dimensionless form, a suitable expansion parameter identified (the Alfvén Mach number of the flow) and the equations obtained by writing variables in a small-parameter series expansion stated. In Section 3.2 the zeroth order perturbation quantities are chosen in such a way that the full model corresponds to the particular solutions of Hornig and Priest (2003), while in Section 3.3 the zeroth order flow is chosen so that a direct comparison with the composite solutions of Hornig and Priest (2003) is found. The choice of zeroth order flow needed if such a comparison is to be made is found to be somewhat limited and so,

in Section 3.4, we proceed to examine a more general solution. Although the flow associated with this solution can be viewed as more realistic its form makes significant analytical progress difficult.

The results of this chapter can be found in Wilmot-Smith et al. (2006a) and Wilmot-Smith et al. (2007a).

3.1   Model Setup

We take the stationary incompressible resistive MHD equations and non-dimensionalise by setting

$$\mathbf{B} = B_e\mathbf{B}', \mathbf{v} = v_e\mathbf{v}', \mathbf{E} = v_eB_e\mathbf{E}', \mathbf{j} = \frac{B_e}{\mu L_e}\mathbf{j}', p = \frac{B_e^2}{\mu}p', \mathbf{r} = L_e\mathbf{r}',$$

where all the dashed quantities are of order one, and B_e, L_e, and v_e are the typical magnetic field strength, length-scale and plasma velocity. Thus Ohm's law becomes

$$\mathbf{E}' + \mathbf{v}' \times \mathbf{B}' = \frac{v_{A_e}}{v_e}\hat{\eta}\mathbf{j}',\tag{3.1}$$

where v_{A_e} is the typical Alfvén speed of the plasma, and

$$\hat{\eta} = \frac{\eta}{\mu L_e v_{A_e}},$$

is the inverse Lundquist number.

The equation of motion is

$$M_e^2(\mathbf{v}' \cdot \nabla')\mathbf{v}' = -\nabla'p' + \mathbf{j}' \times \mathbf{B}',\tag{3.2}$$

where $M_e = v_e/v_{A_e}$ is the Alfvén Mach number. For simplicity we choose to neglect here the effects that viscosity and other forces (such as gravity) might have on the solutions. The remaining MHD equations are given by

$$\nabla' \times \mathbf{B}' = \mathbf{j}',\tag{3.3}$$

$$\nabla' \times \mathbf{E}' = \mathbf{0},$$

$$\nabla' \cdot \mathbf{B}' = 0,$$

$$\nabla' \cdot \mathbf{v}' = 0.$$

Having non-dimensionalised in this way we must now choose a suitable small parameter in which to carry out the expansion. For this we choose the Alfvén Mach number M_e of the flow, and therefore must take $M_e \ll 1$. Low Mach number expansions have already been employed in the development of 2D reconnection theories – for example in the linear reconnection models of Priest and Forbes (1986) and their extention by Jardine and Priest (1988). In this case the expansion of variables is assumed as follows:

$$\mathbf{B}' = \mathbf{B}_0 + M_e\mathbf{B}_1 + M_e^2\mathbf{B}_2 + M_e^3\mathbf{B}_3 + \cdots,$$

$$\mathbf{v}' = \mathbf{v}_1 + M_e\mathbf{v}_2 + M_e^2\mathbf{v}_3 + \cdots,$$

$$\mathbf{j}' = M_e\mathbf{j}_1 + M_e^2\mathbf{j}_2 + M_e^3\mathbf{j}_3 + \cdots,$$

$$\begin{aligned}\mathbf{E}' &= \mathbf{E}_0 + M_e\mathbf{E}_1 + M_e^2\mathbf{E}_2 + \cdots \\ &= -\nabla'\phi_0 - M_e\nabla'\phi_1 - M_e^2\nabla'\phi_2 + \cdots,\end{aligned}$$

$$p' = p_0 + M_ep_1 + M_e^2p_2 + \cdots.$$

where all the quantities $\mathbf{B}_i, \mathbf{v}_i, \mathbf{j}_i, \mathbf{E}_i, \phi_i, p_i$ are dimensionless. Note that we have labelled the first term in the expansion of $\mathbf{v}'$ with the index 1 and have also taken $\mathbf{j}_0 = \mathbf{0}$, so that the lowest order magnetic field is potential, an assumption that is crucial in allowing us to find analytical solutions to the equations. Substituting these expansions into both Ohm's law and the equation of motion and comparing powers of M_e we find that at zeroth order the equation of motion is satisfied with p_0 a constant, while Ohm's law is given by

$$\mathbf{E}_0 + \mathbf{v}_1 \times \mathbf{B}_0 = \hat{\eta}\mathbf{j}_1. \tag{3.4}$$

At first order we obtain

$$\mathbf{E}_1 + \mathbf{v}_1 \times \mathbf{B}_1 + \mathbf{v}_2 \times \mathbf{B}_0 = \hat{\eta}\mathbf{j}_2, \tag{3.5}$$

$$\mathbf{0} = -\nabla'p_1 + \mathbf{j}_1 \times \mathbf{B}_0. \tag{3.6}$$

At second order the equations become

$$\mathbf{E}_2 + \mathbf{v}_1 \times \mathbf{B}_2 + \mathbf{v}_2 \times \mathbf{B}_1 + \mathbf{v}_3 \times \mathbf{B}_0 = \hat{\eta}\mathbf{j}_3, \tag{3.7}$$

$$(\mathbf{v}_1 \cdot \nabla')\,\mathbf{v}_1 = -\nabla'p_2 + \mathbf{j}_2 \times \mathbf{B}_0 + \mathbf{j}_1 \times \mathbf{B}_1, \tag{3.8}$$

while at third order we have

$$\mathbf{E}_3 + \mathbf{v}_1 \times \mathbf{B}_3 + \mathbf{v}_2 \times \mathbf{B}_2 + \mathbf{v}_3 \times \mathbf{B}_1 + \mathbf{v}_4 \times \mathbf{B}_0 = \hat{\eta}\mathbf{j}_4, \tag{3.9}$$

$$(\mathbf{v}_2 \cdot \nabla')\,\mathbf{v}_1 + (\mathbf{v}_1 \cdot \nabla')\,\mathbf{v}_2 = -\nabla'p_3 + \mathbf{j}_3 \times \mathbf{B}_0 + \mathbf{j}_2 \times \mathbf{B}_1 + \mathbf{j}_1 \times \mathbf{B}_2. \tag{3.10}$$

It is clear that a natural coupling exists not between the same ordered equations for Ohm's law and the equation of motion, but rather between Ohm's law at a given order, and the equation of motion at the next order. Thus to solve the system we will have to consider, for example, equations (3.4) and (3.6) together, and (3.5) and (3.8) together.

We set

$$\mathbf{B}_0 = b_0(ky, kx, 1), \tag{3.11}$$

where b_0 and k are constants and $k > 0$. Thus our basic state is an X-type current-free equilibrium in the xy-plane, superimposed on a uniform field in the z-direction. The field structure is illustrated in Figure 3.1. The field is assumed to be reconnecting slowly ($v \ll v_A$), and is similar to that taken by Hornig and Priest (2003) although in that case the separatrices are not inclined at right-angles, so allowing for a current.
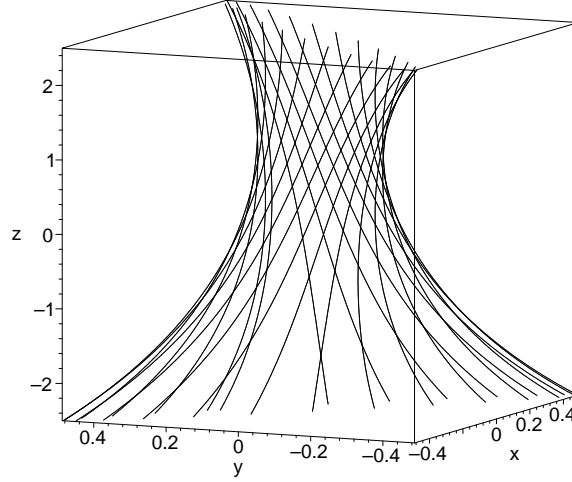
Figure 3.1: Illustration of some particular field lines indicating the structure of the magnetic field $\mathbf{B}_0$.

With this choice of field configuration we can analytically integrate the equations

$$\frac{\partial \mathbf{X}(s)}{\partial s} = \mathbf{B}\left(\mathbf{X}\left(s\right)\right)$$

to find the equations $\mathbf{X}\left(\mathbf{x}_0, s\right)$ of the field line passing through the initial point $\mathbf{x}_0$. The components of $\mathbf{X}\left(\mathbf{x}_0, s\right)$ are given by

$$
\begin{aligned}
X &= x_0 \cosh(b_0 k s) + y_0 \sinh(b_0 k s), \\
Y &= y_0 \cosh(b_0 k s) + x_0 \sinh(b_0 k s), \\
Z &= b_0 s + z_0.
\end{aligned}
\tag{3.12}
$$

with the inverse mapping $\mathbf{X_0}(\mathbf{x}, s)$, being given by

$$
\begin{aligned}
X_0 &= x \cosh(b_0 k s) - y \sinh(b_0 k s), \\
Y_0 &= y \cosh(b_0 k s) - x \sinh(b_0 k s), \\
Z_0 &= -b_0 s + z.
\end{aligned}
\tag{3.13}
$$

The parameter s parameterizes the magnetic field line and is related to the distance, λ, along field lines by $ds = d\lambda/|B|$.

As a further simplification we take $\mathbf{B}_1 = \mathbf{0}$, so that any zeroth-order flow is ideal. This assumption is not necessary for a complete solution to the system, but it does permit us to obtain ideal and non-ideal parts to Ohm's law in the zeroth- and first-order equations respectively, with a corresponding equation of motion for both solutions (at first- and second-order respectively). Thus the construction of this model allows for a direct comparison of our solutions with the kinematic ones of Hornig and Priest (2003) where a similar decomposition resulted in particular solutions satisfying the non-ideal Ohm's law, and composite solutions in which an ideal solution was superposed on this basic state. We have here in addition an equation of motion for both the particular and ideal solutions and so can consider also how this alters the results.

3.2   Particular Solutions

In this section we consider the implications of the first-order solution alone, by assuming $\mathbf{v}_1 = \mathbf{0}$. Ohm's law at zeroth order becomes $\mathbf{E}_0 = \mathbf{0}$, while the equation of motion is safisfied at zeroth and first order with p_0 and p_1 constants. This assumption results in the solutions obtained being equivalent to the particular solutions of Hornig and Priest (2003) (with the first order Ohm's law the non-ideal equation), but now also satisfying the momentum equation. For these particular solutions it is first necessary to consider equations (3.5) and (3.8) together:

$$\mathbf{E}_1 + \mathbf{v}_2 \times \mathbf{B}_0 = \hat{\eta}\mathbf{j}_2, \tag{3.14}$$

$$\mathbf{0} = -\nabla' p_2 + \mathbf{j}_2 \times \mathbf{B}_0. \tag{3.15}$$

Under these assumptions it is at fourth order that the inertial term first appears, and thus the dynamic effects in our particular solution are primarily the Lorentz force and the pressure gradients. Here we will consider the implications of two different forms for the non-ideal terms, $\hat{\eta}\mathbf{j}_2$, with special emphasis placed on the resulting plasma flows and rate of reconnected flux.

Localisation of the non-ideal term $\hat{\eta}\mathbf{j}_2$ can be achieved through a localisation in three dimensions of either $\hat{\eta}$, or of $\mathbf{j}_2$, or, in the physically most realistic situation, through a localisation of both terms. The important quantity in determining the main results presented here is ϕ_1, which is dependent only on the localisation of the product $\hat{\eta} j_{2\parallel}$, and not on how the localisation is realised. As a simplification and in order to allow for analytical solutions we here choose to prescribe a localisation of the resistivity $\hat{\eta}$. This assumption was also taken by Hornig and Priest (2003) where a hyperbolic field similar to that given by (3.11) resulted in a uniform current in the $\hat{\mathbf{z}}$-direction. By taking the curl of (3.15) we obtain

$$(\mathbf{B}_0 \cdot \nabla)\mathbf{j}_2 - (\mathbf{j}_2 \cdot \nabla)\mathbf{B}_0 = \mathbf{0},$$

which, assuming $\mathbf{j}_2 = j_2(x, y)\hat{\mathbf{z}}$, gives $(\mathbf{B}_0 \cdot \nabla)\mathbf{j}_2 = \mathbf{0}$, i.e. $\mathbf{j}_2$ as constant along field lines of $\mathbf{B}_0$:

$$\mathbf{j}_2 = f(x^2 - y^2)\hat{\mathbf{z}}. \tag{3.16}$$

There are a number of ways to choose $f(x^2 - y^2)$, two of which we examine here. In Section 3.2.1 we take f to be uniform, as was the case in Hornig and Priest (2003). In Section 3.2.2 we instead assume a form such that the current $\mathbf{j}_2$ is localised along separatrices of $\mathbf{B}_0$, which is motivated by the numerical experiments of Pontin et al. (2005a) where a such a current was observed.

3.2.1   Uniform Current

The simplest choice of $f(x^2 - y^2)$ is to take

$$\mathbf{j}_2 = j_{20}\hat{\mathbf{z}},$$

where j_{20} is constant. Such a current can be obtained by taking, for example, the magnetic field

$$\mathbf{B}_2 = -\mu j_{20} y \hat{\boldsymbol{x}},$$

which can be expressed as

$$\mathbf{B}_2 = \nabla \times A_2 \hat{\boldsymbol{z}}$$

where

$$A_2 = -\mu j_{20} y^2 / 2.$$

This is a particular solution for $\mathbf{B}_2$. Other particular solutions exist, to each of which we are free to add any potential vector field $\mathbf{B}_2^{pot} = \nabla \Psi_2$. With this perturbation the field $\mathbf{B}_0 + M_e^2 \mathbf{B}_2$ retains its X-type structure in the xy-plane, but now has separatrices inclined at a different angle. The sign of j_{20} determines whether the greater angle between separatrices is across the x-axis (for $j_{20} > 0$) or the y-axis (for $j_{20} < 0$). In this section we assume, without loss of generality, that $j_{20} < 0$.

Now (3.15) allows us to deduce p_2 as

$$p_2 = p_{20} + \frac{k j_{20} b_0}{2}(y^2 - x^2),$$

where p_{20} is constant.

Considering next Ohm's law, (3.14), we seek a solution such that the non-ideal term $\hat{\eta} \mathbf{j}_2$ is localised. Since the current $\mathbf{j}_2$ is uniform we must localise the resistivity, $\hat{\eta}$. To achieve this, together with an analytical form for the remaining terms, we prescribe a localised form for $\mathbf{E}_1 \cdot \mathbf{B}_0$, then taking the scalar product of (3.14) with $\mathbf{B}_0$ determine $\hat{\eta}$ as

$$\hat{\eta} = \frac{\mathbf{E}_1 \cdot \mathbf{B}_0}{\mathbf{j}_2 \cdot \mathbf{B}_0}.$$

One suitable form is to impose

$$\mathbf{E}_1 \cdot \mathbf{B}_0 = e_{10} b_0 \exp\left(-\frac{b_0^2 s^2}{L^2} - \frac{x_0^2 + y_0^2}{l^2}\right), \tag{3.17}$$

where $l, L > 0$. This expression is a function of the coordinates of the field lines, x_0, y_0 and s, but, setting $Z_0 = 0$, we may use the inverse field line mappings (3.13) to find an equivalent expression in terms of x, y, and z. Thus we obtain the function $\hat{\eta}$ as

$$\hat{\eta} = \frac{e_{10}}{j_{20}} \exp\left(-\frac{z^2}{L^2}\right) \exp\left(\frac{2xy \sinh(2kz) - (x^2 + y^2)\cosh(2kz)}{l^2}\right). \tag{3.18}$$

Provided e_{10} and j_{20} have the same sign this is a positive function. The parameter L gives the length of the diffusion region in the $\hat{\boldsymbol{z}}$-direction, while l represents the width of the diffusion region in the $z = 0$ plane. The hyperbolic nature of the field may render it necessary to decrease l with increasing L to ensure the diffusion region remains localised. An example of such a diffusion region is shown in Figure 3.2, where the surface $\hat{\eta} = 0.02\hat{\eta}_{max}$ is shown. The maximum value of $\hat{\eta}$ occurs at the origin, where $\hat{\eta} = e_{10}/j_{20}$.
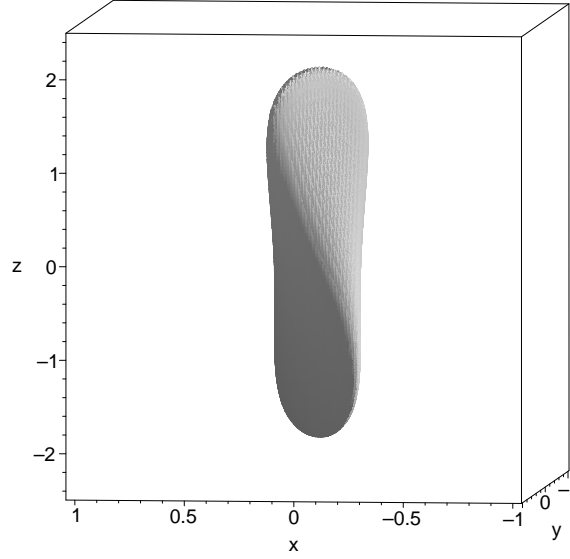
Figure 3.2: The surface $\hat{\eta} = 0.02\hat{\eta}_{max}$, containing the non-ideal region D, with the parameters $l = 0.1$, $L = 1$, $j_{20} = -1$, $e_{10} = -1$, $k = 0.5$.

It remains to find $\mathbf{E}_1$ and $\mathbf{v}_2$. We have $\mathbf{E}_1 = -\nabla\phi_1$ so, now that $\hat{\eta}$ is given, we may integrate along the field lines to deduce ϕ_1;

$$\begin{aligned} \phi_1 &= -\int \hat{\eta}\mathbf{j}_2 \cdot \mathbf{B}_0 \, ds \\ &= -\int (\mathbf{E}_1 \cdot \mathbf{B}_0) \, ds. \end{aligned} \tag{3.19}$$

Taking the gradient of this expression gives an analytical form for $\mathbf{E}_1$. Writing

$$Q = \frac{e_{10}\sqrt{\pi}L}{l}\mathrm{erf}\left(\frac{z}{L}\right),$$

and

$$\gamma = -\frac{\left(x^2 + y^2\right)\cosh\left(2kz\right) - 2xy\sinh\left(2kz\right)}{l^2},$$

we find

$$\mathbf{E}_1 = Qe^{\gamma}\frac{\left(-x\cosh\left(2kz\right) + y\sinh\left(2kz\right)\right)}{l}\hat{\boldsymbol{x}} + Qe^{\gamma}\frac{\left(x\sinh\left(2kz\right) - y\cosh\left(2kz\right)\right)}{l}\hat{\boldsymbol{y}}$$

$$+ \left(Qe^{\gamma}\frac{\left(2kxy\cosh\left(2kz\right) - k\left(x^2 + y^2\right)\sinh\left(2kz\right)\right)}{l} + e_{10}e^{\gamma}e^{-z^2/L^2}\right)\hat{\boldsymbol{z}}.$$

The vector product of (3.14) with $\mathbf{B}_0$ gives the component of $\mathbf{v}_2$ perpendicular to $\mathbf{B}_0$ as

$$\mathbf{v}_{2\perp} = \frac{(\mathbf{E}_1 - \hat{\eta}\mathbf{j}_2) \times \mathbf{B}_0}{b_0} = \frac{\left(\mathbf{E}_1 - E_{1\parallel}\hat{\boldsymbol{z}}/b_0\right) \times \mathbf{B}_0}{|\mathbf{B}_0|^2}.$$

We are free to add a velocity component parallel to $\mathbf{B}_0$, and choose to do so in such a way that the $\hat{\boldsymbol{z}}$-
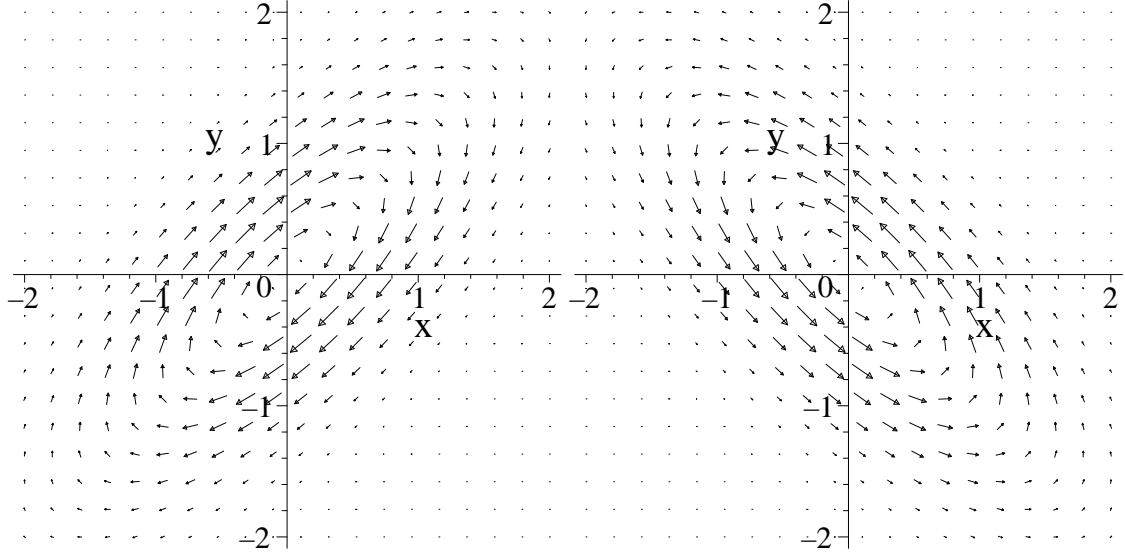
Figure 3.3: The velocity field $\mathbf{v}_2$, for (a) $z = 1$ and (b) $z = -1$, and the parameters $l = 1$, $L = 1$, $e_{10} = -1$, $k = 0.5$ and $b_0 = 1$.

component of $\mathbf{v}_2$ is zero:

$$\mathbf{v}_2 = \mathbf{v}_{2\perp} - \frac{(\mathbf{v}_{2\perp})_z \mathbf{B}_0}{|\mathbf{B}_0|^2}.$$

This also ensures that the resulting velocity is divergence-free.

Thus $\mathbf{v}_2$ is given by

$$\mathbf{v}_2 = \frac{Qe^\gamma}{b_0} \left(\frac{(x \sinh(2kz) - y \cosh(2kz))}{l} \hat{\boldsymbol{x}} + \frac{(x \cosh(2kz) - y \sinh(2kz))}{l} \hat{\boldsymbol{y}} \right). \tag{3.20}$$

Figure 3.3 illustrates $\mathbf{v}_2$ in two particular planes above and below the $z = 0$ plane. The flow is counter-rotational above and below the $z = 0$ plane, where it vanishes. Non-zero flow is limited to the region within the hyperbolic flux tube (HFT) which consists of the field lines passing through the non-ideal region. Near to the origin the velocity field is almost circular, but becomes distorted by the magnetic field on moving away from the plane $z = 0$, as shown in Figure 3.3. The pure solutions of Hornig and Priest (2003) are very similar, themselves being counter-rotational flows within the HFT, distorted by the magnetic field.

We are left to consider the remaining second-order equation, (3.7), which becomes

$$\mathbf{E}_2 + \mathbf{v}_3 \times \mathbf{B}_0 = \hat{\eta} \mathbf{j}_3. \tag{3.21}$$

This may be satisfied by taking $\mathbf{E}_2 = 0$, $\mathbf{v}_3 = 0$, and $\mathbf{j}_3 = 0$. We then may solve Ohm's law at all even orders, and the equation of motion at all odd orders, by taking

$$\mathbf{v}_i = \mathbf{B}_i = \mathbf{j}_i = \mathbf{E}_{i-1} = \mathbf{0}, \ p_i = p_{i0}, \text{ for } i = 5, 7, 9, ...$$

The equation of motion at all subsequent even orders, and Ohm's law at all subsequent odd orders may

also be solved, at least numerically, to determine completely all higher-order quantities. Here we outline a scheme for Ohm's law at third order and the equation of motion at fourth order:

$$-\nabla'\phi_3 + \mathbf{v}_4 \times \mathbf{B}_0 + \mathbf{v}_2 \times \mathbf{B}_2 = \hat{\eta}\mathbf{j}_4, \tag{3.22}$$

$$\rho\left(\mathbf{v}_2 \cdot \nabla'\right)\mathbf{v}_2 = -\nabla'p_4 + \mathbf{j}_4 \times \mathbf{B}_0 + \mathbf{j}_2 \times \mathbf{B}_2. \tag{3.23}$$

Since the components of both $\left(\mathbf{v}_2 \cdot \nabla\right)\mathbf{v}_2$ and $\mathbf{j}_2 \times \mathbf{B}_2$ parallel to $\mathbf{B}_0$ are known, we may use (3.23) to calculate p_4 by integrating along the field lines, starting from $p_4 = p_{40}\left(x_0, y_0\right)$ in the plane $z = 0$:

$$p_4\left(x_0, y_0, s\right) = -\int_{s=0}^{z/b_0}\left(\left(\mathbf{v_2} \cdot \nabla\right)\mathbf{v_2} - \mathbf{j_2} \times \mathbf{B_2}\right) \cdot \mathbf{B_0}\, \mathrm{d}s + p_4\left(x_0, y_0\right).$$

Using the inverse field line mappings this expression can be rewritten in terms of x, y, and z and ∇p_4 then deduced. In turn this allows us to find the perpendicular component of the current $\mathbf{j}_4$:

$$\mathbf{j}_{4\perp} = \frac{\left(-\nabla p_4 - \left(\mathbf{v}_2 \cdot \nabla\right)\mathbf{v}_2 + \mathbf{j}_2 \times \mathbf{B}_2\right) \times \mathbf{B}_0}{|B_0|^2}.$$

The freedom to add a component parallel to $\mathbf{B}_0$ may then be used to ensure $\mathbf{j}_4$ is divergence-free.

Turning to (3.22), it is left to determine ϕ_3 and $\mathbf{v}_4$. The equation has essentially the same structure as (3.23), and so may be solved in the same way by again integrating along the field lines to find

$$\phi_3(x_0, y_0, s) = -\int\left(\hat{\eta}\mathbf{j}_4 - \mathbf{v}_2 \times \mathbf{B}_2\right) \cdot \mathbf{B}_0\, \mathrm{d}s + \phi_3(x_0, y_0).$$

The component of the flow $\mathbf{v}_4$ perpendicular to $\mathbf{B}_0$ is given by:

$$\mathbf{v}_{4\perp} = \frac{\left(-\nabla\phi_3 - \eta\mathbf{j}_4 + \mathbf{v}_2 \times \mathbf{B}_2\right) \times \mathbf{B}_0}{|B_0|^2}.$$

Letting

$$\mathbf{v}_4 = \mathbf{v}_{4\perp} - \frac{v_{4_z}}{B_{0_z}}\mathbf{B}_0.$$

ensures $\mathbf{v}_4$ is divergence-free so that the continuity equation is satisfied. This scheme would be effective even without the assumption $\mathbf{B}_1 = 0$, which has been used to allow a direct comparison with the kinematic case. It is worthwhile to note however that obtaining numerical solutions in this manner is not expected to be a trivial task.

We now have sufficient information to determine the rate of reconnected flux. In 2D reconnection with reconnection at an X-type null point the extension of the null point along the invariant direction is a null line, or 'reconnection line'. With the addition of a uniform field component in the invariant direction the line becomes a field line across which the difference in electric potential across the non-ideal region is maximal. We therefore identify this line as the reconnection line and the reconnection rate is given by the

integral of the parallel electric field along the reconnection line (the z-axis):

$$\frac{\mathrm{d}\Phi_{\mathrm{mag}}}{\mathrm{d}t} = \int \mathbf{E}_{\parallel} \, \mathrm{d}l = \int_{-\infty}^{\infty} \left(M_e \, e_{10} \, e^{-z^2/L^2} + O\left(M_e^3\right) \right) \, \mathrm{d}z = \sqrt{\pi} M_e \, e_{10} L + O\left(M_e^3\right). \quad (3.24)$$

The parameter l does not appear in this expression and so we conclude that the extent of the diffusion region in the xy-plane does not change the reconnection rate. This agrees with a similar finding in Hornig and Priest (2003) that the diameter of their non-ideal region did not affect the reconnection rate.

3.2.2 Localised Current

In this section we assume an alternative form for the current $\mathbf{j}_2$. We examine its effect on the remaining first- and second-order terms and compare the solutions with those found in the previous section.

We have seen $\mathbf{j}_2$ is constant along field lines of $\mathbf{B}_0$, i.e. satisfies (3.16). Another obvious choice for $f(x^2 - y^2)$ is one which produces an enhanced current at the origin, which in turn requires j_2 to be localised along the separatrices of $\mathbf{B}_0$. A suitable example is

$$\mathbf{j}_2 = \frac{j_{20}}{\cosh^2\left(\frac{x^2 - y^2}{\lambda^2}\right)} \hat{\mathbf{z}}. \quad (3.25)$$

A motivation for this choice is given by the numerical simulation of Pontin et al. (2005a) who observed the evolution of magnetic flux in an isolated diffusion region within a hyperbolic flux tube, and thus have a reconnection process similar in many respects to the one we are studying. The current concentration was found to grow throughout the run, and the final profile, as shown in Figure 3.4, has a 'bow-tie' structure. The choice of current given by (3.25) results in a similar current density profile close to the origin.

Substituting (3.25) into (3.15) gives the pressure p_2 as

$$p_2 = p_{20} - \tfrac{1}{2}\lambda^2 k b_0 j_{20} \tanh\left(\frac{x^2 - y^2}{\lambda^2}\right). \quad (3.26)$$

Whereas in the previous example (Section 3.2.1) the pressure gradient had a stagnation structure, the localisation of the current now gives a pressure gradient that is localised along the separatrices of $\mathbf{B}_0$. It is dependent on the sign of j_{20}, taken to be negative here, although at this stage the choice is arbitrary. An example of the resulting pressure p_2 is shown in Figure 3.5. The saddle-point pressure profile is a direct consequence of the hyperbolic nature of the field, since there is no inertial term in equation (3.15). Such saddle-point profile would persist in the presence of inertial terms of a magnitude similar to, or less than, the Lorentz force.

Setting $\mathbf{B}_2 = \nabla \times A_2 \hat{\mathbf{z}}$, we may find a divergence-free field $\mathbf{B}_2$ which produces the current given by (3.25). We are unable to use the method of infinite space Green's functions, since this would require the contribution of the 'boundary' terms of A_2 at infinity to vanish. Instead we use an eigenfunction expansion technique as described in the following paragraph.
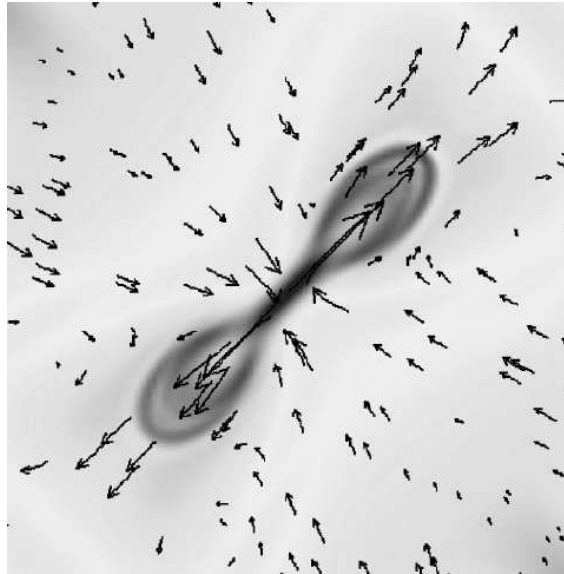
Figure 3.4: Results of a 3D MHD numerical simulation by Pontin et al. (2005a). Background shading indicates the magnitude of the final current density in the central plane, with vectors indicating the plasma velocity.
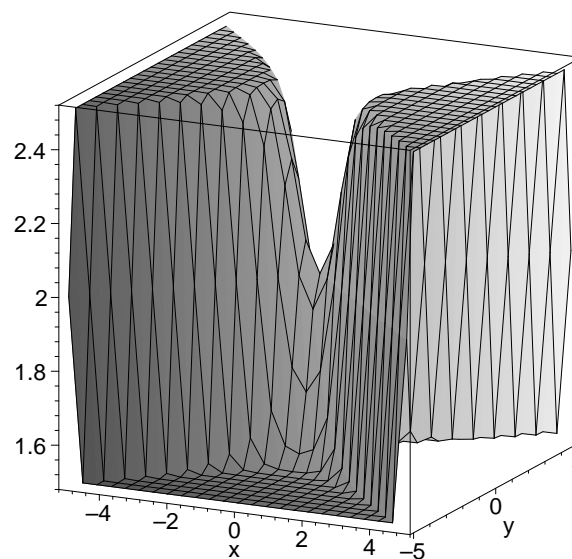
Figure 3.5: The pressure profile p_2 for $\mathbf{v}_1 = \mathbf{0}$, $\mathbf{j}_2 = j_{20}/\cosh^2\left(\left(x^2 - y^2\right)/\lambda^2\right)\hat{\mathbf{z}}$, with the parameters $p_{20} = 2$, $\lambda = 1$, $k = 0.5$, $j_{20} = -1$ and $b_0 = 2$.

Consider solutions to Poisson's equation

$$\nabla^2 A = f(x, y) \tag{3.27}$$

in the square $0 < x, y < H$ with A vanishing on the boundary by assuming the related two-dimensional eigenfunctions

$$\nabla^2 \psi = -\zeta \psi$$

with $\psi = 0$ on the boundary. For the square the eigenfunctions are sine series in both y and x:

$$\psi_{nm} = \sin\left(\frac{n\pi x}{H}\right) \sin\left(\frac{m\pi y}{H}\right),$$

$$\zeta_{nm} = \left(\frac{n\pi}{H}\right)^2 + \left(\frac{m\pi}{H}\right)^2.$$

Expanding the solution in terms of these eigenfunctions, it can be written as

$$A_2 = \sum_{n=1}^{\infty} \sum_{m=1}^{\infty} c_{nm} \sin\left(\frac{n\pi x}{H}\right) \sin\left(\frac{m\pi y}{H}\right),$$

where c_{nm} are constants. Substituting this solution into (3.27) and noting $\nabla^2 \psi = -\zeta_{nm}\psi_{nm}$, we obtain

$$\sum_{n=1}^{\infty} \sum_{m=1}^{\infty} -c_{nm} \sin\left(\frac{n\pi x}{H}\right) \sin\left(\frac{m\pi y}{H}\right) = f(x, y).$$

Now, using the orthogonal properties of the eigenfunctions, and observing that they satisfy the same boundary conditions as the solution, we have

$$-\zeta_{nm}c_{nm} \int_0^H \int_0^H \sin\left(\frac{n\pi x}{H}\right)^2 \sin\left(\frac{m\pi y}{H}\right)^2 \mathrm{d}x\mathrm{d}y =$$
$$= \int_0^H \int_0^H f(x, y) \sin\left(\frac{n\pi x}{H}\right) \sin\left(\frac{m\pi y}{H}\right) \mathrm{d}x\mathrm{d}y.$$

which determines the coefficients c_{nm}.

Using the above described method to solve

$$\nabla^2 A_2 = \frac{\mu j_{20}}{\cosh^2\left(\frac{x^2 - y^2}{\lambda^2}\right)}$$

in the region $-H/2 < x, y < H/2$ with $A_2 = 0$ on the boundary, we obtain

$$A_2(x, y) = \sum_{n, m \ odd} \sum c_{nm} \sin\left(n\pi\left(x/H - 1/2\right)\right) \sin\left(m\pi\left(y/H - 1/2\right)\right), \tag{3.28}$$

where the coefficients c_{nm} are given by

$$c_{nm} = \frac{-4\mu j_{20}}{(n^2 + m^2)\pi^2} \int_{-H/2}^{H/2} \int_{-H/2}^{H/2} \frac{\sin\left(n\pi\left(x/H - 1/2\right)\right) \sin\left(m\pi\left(y/H - 1/2\right)\right)}{\cosh^2\left(\frac{x^2 - y^2}{\lambda^2}\right)} \mathrm{d}x\mathrm{d}y.$$
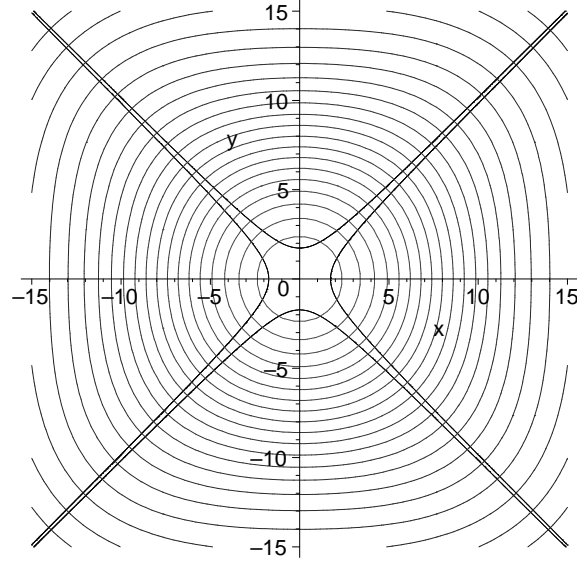
Figure 3.6: Contours of A_2 where $\mathbf{B}_2 = \nabla \times A_2 \hat{\boldsymbol{z}}$ and $\mathbf{j}_2 = j_{20}/\cosh^2(x^2 - y^2)\hat{\boldsymbol{z}}$ with the parameters $j_{20} = 1$, $\lambda = 1$, $\mu = 1$. Overlayed (darker lines) is the current density contour $1/\cosh^2(x^2 - y^2) = 0.1$.

The change of variables $u = x/\lambda$, $v = y/\lambda$, $\xi = H/\lambda$ allows the integrand to be expressed in a form independent of λ, and we obtain the equivalent expression for the coefficients c_{nm}:

$$c_{nm} = \frac{-4j_{20}\lambda^2}{(n^2 + m^2)\pi^2} \int_{-\xi/2}^{\xi/2} \int_{-\xi/2}^{\xi/2} \frac{\sin\left(n\pi\left(u/\xi - 1/2\right)\right)\sin\left(m\pi\left(v/\xi - 1/2\right)\right)}{\cosh^2\left(u^2 - v^2\right)}\,\mathrm{d}u\mathrm{d}v. \tag{3.29}$$

We find that each $c_{nm} \to 0$ as $n, m \to \infty$ and that as $H \to \infty$ each c_{nm} tends to a limiting value. Thus we use (3.28), with the coefficients (3.29) evaluated numerically, to find a form for $\mathbf{B}_2$.

A_2 is a smooth function with opposite sign from that of j_{20}, with the maximum of $|A_2|$ occurring at $x = y = 0$. The contours of A_2, which are field lines for $\mathbf{B}_2$, are shown in Figure 3.6. Superimposed is an outline of the current $\mathbf{j}_2$. The X-type structure of the field $\mathbf{B}_0$ becomes flattened by the perturbation $\mathbf{B}_2$; toward the y-axis when $j_{20} < 0$ (which is assumed to be the case here) and toward the x-axis when $j_{20} > 0$. This is shown in Figure 3.7 where the coefficient M_e^2 has been taken as $M_e^2 = 0.5$ to illustrate the effect.

Following the method previously outlined, we now prescribe a localised form for $\mathbf{E}_1 \cdot \mathbf{B}_0$, and determine $\hat{\eta}$ as

$$\hat{\eta} = \frac{\mathbf{E}_1 \cdot \mathbf{B}_0}{\mathbf{j}_2 \cdot \mathbf{B}_0}$$

by taking the scalar product of (3.14) with $\mathbf{B}_0$. Here we assume

$$\mathbf{E}_1 \cdot \mathbf{B}_0 = e_{10}b_0 \exp\left(-\frac{\left(y^2 - x^2\right)^2}{\kappa^4}\right)\exp\left(-\frac{b_0^2 s^2}{l^2} - \frac{x_0^2 + y_0^2}{l^2}\right) \tag{3.30}$$

with $l, L > 0$. This is similar to (3.17), with an extra factor $e^{-\left(y^2 - x^2\right)^2/\kappa^4}$ to later ensure $\hat{\eta}$ is sufficiently localised. Using the inverse field line mappings (3.13) to find an equivalent expression in terms of x, y, and
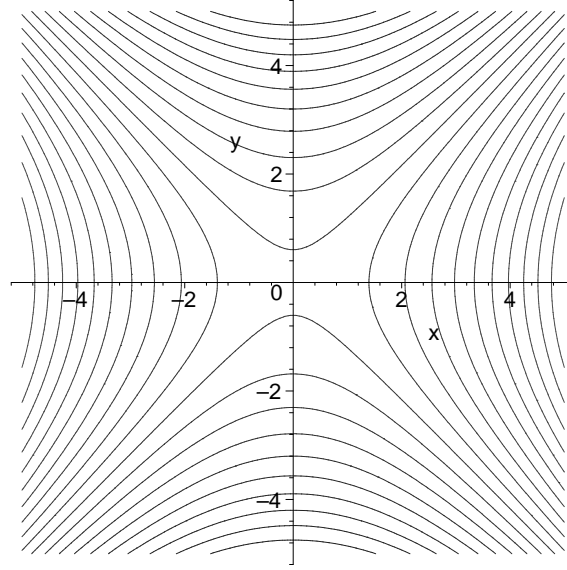
Figure 3.7: Magnetic field lines (contours of $A_0 + M_e^2 A_2$) in the xy-plane with $M_e^2 = 0.5$ and the parameters $j_{20} = -1$, $\lambda = 1$, $b_0 = 1$, $\mu = 1$ and $k = 1$.

z we obtain $\hat{\eta}$ as

$$\hat{\eta} = \frac{e_{10}}{j_{20}} e^{-\frac{z^2}{L^2}} \exp\left(\frac{-\left(y^2 - x^2\right)^2}{\kappa^4}\right) \cosh^2\left(\frac{x^2 - y^2}{\lambda^2}\right) \times \qquad (3.31)$$

$$\exp\left(\frac{2xy \sinh\left(2kz\right) - \left(x^2 + y^2\right)\cosh\left(2kz\right)}{l^2}\right),$$

which is again a positive function provided e_{10} and j_{20} are of the same sign.

Figure 3.8(a) shows the diffusion region in this example; it is seen to be very similar to that of Section (3.2.1). Although the diffusion region given by (3.18) was circular in the xy-plane and elliptical for non-zero z values, as illustrated by the cross sections of Figure 3.8(b), in this case it is distorted from that shape by the current now lying along the separatrices of the field in the xy-plane.

We deduce an analytical form for $\mathbf{E}_1$ using (3.19) which in turn allows us to find $\mathbf{v}_{2\perp}$, the component of $\mathbf{v}_2$ parallel to $\mathbf{B}_0$. This is given by

$$\mathbf{v}_{2\perp} = \frac{\left(\mathbf{E}_1 - \hat{\eta}\mathbf{j}_2\right) \times \mathbf{B}_0}{|\mathbf{B}_0|^2} = \frac{\left(\mathbf{E}_1 - E_{1\parallel}\hat{z}/b_0\right) \times \mathbf{B}_0}{|\mathbf{B}_0|^2},$$

to which we add a velocity component parallel to $\mathbf{B}_0$ to set its $\hat{z}$-component to zero and ensure it is divergence-free:

$$\mathbf{v}_2 = \mathbf{v}_{2\perp} - \frac{\left(\mathbf{v}_{2\perp}\right)_z \mathbf{B}_0}{|\mathbf{B}_0|^2}.$$

Setting

$$M = \frac{Qe^\gamma}{b_0} \exp^{-\frac{\left(x^2 - y^2\right)^2}{\kappa^4}},$$
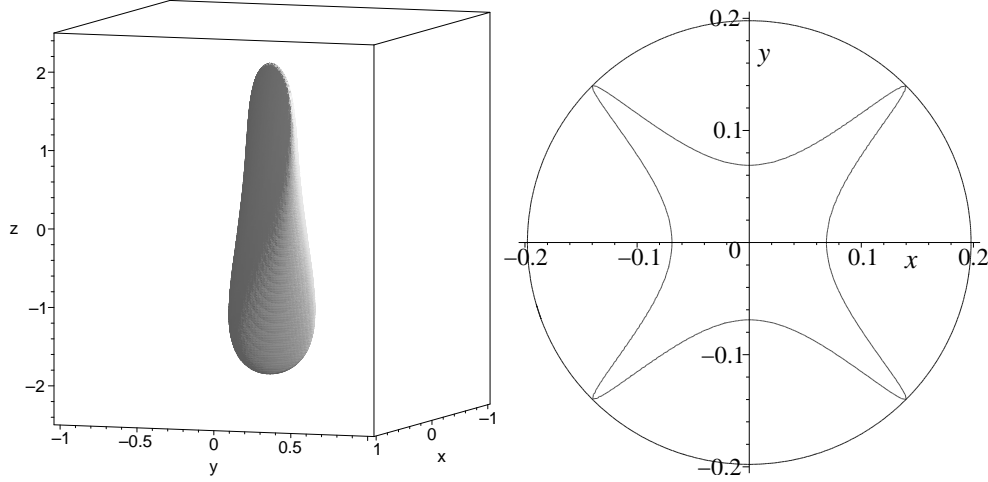
Figure 3.8: (a) The surface $\hat{\eta} = 0.02\hat{\eta}_{max}$, containing the non-ideal region D given by (3.31), and (b) cross sections in the $z = 0$ plane of the non-ideal regions D given by (3.18) (outer circle) and (3.31) (inner curve). Both figures use the parameters $l = 0.1$, $L = 1$, $j_{20} = -1$, $e_{10} = -1$, $k = 0.5$, $\kappa = 0.1$, and $\lambda = 1$.

the resulting flow $\mathbf{v}_2$ is given by

$$\mathbf{v}_2 = M\left(\frac{x\sinh(2kz) - y\cosh(2kz)}{l} + 2ly\frac{x^2 - y^2}{\kappa^4}\right)\hat{\boldsymbol{x}} \tag{3.32}$$

$$+ M\left(\frac{x\cosh(2kz) - y\sinh(2kz)}{l} + 2lx\frac{x^2 - y^2}{\kappa^4}\right)\hat{\boldsymbol{y}}.$$

The additional factor $\exp\left(-\left(x^2 - y^2\right)^2/\kappa^4\right)$ introduced in (3.30), and not present in (3.17), has had the effect of narrowing the HFT away from the $\hat{\boldsymbol{z}}$-axis. The factor therefore has the same effect on the counter-rotational flow $\mathbf{v_2}$, as clearly shown in Figure 3.9, although the qualitative structure remains largely the same.

The rate of reconnected flux can again be determined. The z-axis remains the reconnection line,

$$\frac{\mathrm{d}\Phi_{\mathrm{mag}}}{\mathrm{d}t} = \int \mathbf{E}_\parallel \, \mathrm{d}l = \int_{-\infty}^{\infty} \left(M_e \, e_{10} \, e^{-z^2/L^2} + O\left(M_e^3\right)\right) \, \mathrm{d}z = \sqrt{\pi}M_e \, e_{10}L + O\left(M_e^3\right). \tag{3.33}$$

This equation is precisely the same as that of the previous example, given by (3.24). The shape of the diffusion region in the xy-plane, which is different in both our examples, in turn alters the shape of the HFT and therefore the structure of the plasma velocity $\mathbf{v}_2$. However in the above expression these dimensions are unimportant, since it is the length of the diffusion region along the $\hat{\boldsymbol{z}}$-axis which is key in determining the reconnection rate. In principle, any decaying function could have been used to determine this length.

The model used does not allow for a simple scaling of the reconnection rate with respect to the resistivity or Lundquist number, and so we cannot yet determine the maximum rate of reconnection. This is a consequence of three dimensional reconnection being more complex and having a greater variety of solutions than the two dimensional case. Consider the values of the variables at a height $z = L_e$ above the
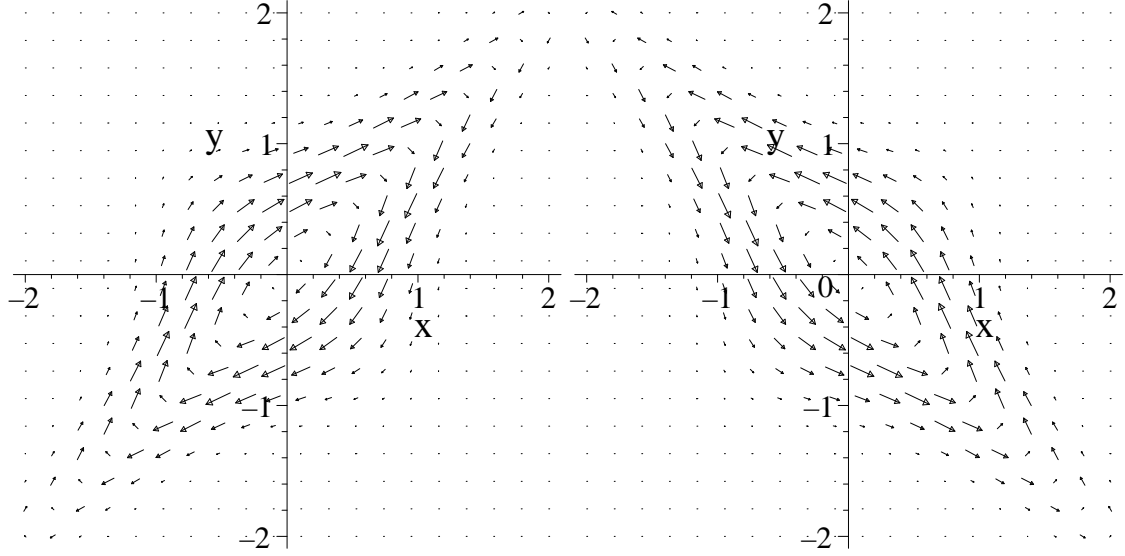
Figure 3.9: The velocity field $\mathbf{v}_2$, for (a) $z = 1$ and (b) $z = -1$, and the parameters $l = 1$, $L = 1$, $e_{10} = -1$, $k = 0.5$, $b_0 = 1$, and $\kappa = 1$.

non-ideal region. There the ratio (v_e/v_{A_e}) of the plasma velocity to the Alfvén velocity is given by

$$\frac{v_e}{v_{A_e}} = \frac{\sqrt{\pi}}{\sqrt{2}R_{m_e}} \frac{L_e}{l} \frac{L}{l} g, \tag{3.34}$$

where R_{m_e} is the global magnetic Reynolds number, $R_{m_e} = L_e v_{A_e}/\eta$, and $g = \exp(kL_e - 1/2)$ is a factor relating to the geometry of the magnetic field. The ordering of parameters $L_E > L > l$ has been assumed. The parameters l and L, which relate to the structure of the non-ideal region, and g, which relates to the field geometry, would not in a general 3D reconnection event be arbitrary, but rather determined by the evolution of the magnetic field before the onset of a stationary phase. Therefore the expression (3.34) should be interpreted with particular care. Although at first sight it appears to scale as $R_{m_e}^{-1}$, each of the other factors on the right hand side of (3.34) can be much larger than unity and also depend on R_{m_e} ($l = l(R_{m_e})$, $L = L(R_{m_e})$, $g = g(L_e, R_{m_e})$). Determining how v_e/v_{A_e} scales with R_{m_e} and so whether or not the reconnection is fast is outside the scope of this simple stationary model. Instead we proceed to examine the case of 'composite solutions'.

3.3   Composite Solutions

In many realistic situations the plasma velocity outside the HFT will be non-zero, and therefore we here choose to superimpose an ideal solution ($\mathbf{v}_1 \neq 0$) on the particular solution, giving composite solutions. In the kinematic analysis, as given by Hornig and Priest (2003), the two solutions are essentially independent, but in the present dynamic analysis they are coupled in the momentum equation (3.8) by the inertial term $(\mathbf{v}_1 \cdot \nabla')\mathbf{v}_1$. We now examine the extent to which the coupling restricts the choice of the ideal solution, and investigate how the reconnection process differs between the particular and composite solutions.

In general, the momentum equation given by (3.8) implies a coupling between the ideal and non-ideal Ohm's laws given by equations (3.4) and (3.5). However, for the class of ideal plasma flows $\mathbf{v}_1$ for which the curl of the inertial term on the left-hand side of (3.8) vanishes, the equations become decoupled. In this case the effects of a non-trivial solution to (3.4) are apparent at second order only in the pressure gradient ∇p_2. For ideal flows satisfying this condition the particular solutions of Section 3.2 may be taken as a solution to (3.5), and so we have a direct comparison with the composite solutions of Hornig and Priest (2003). We begin by examining an ideal stagnation flow $\mathbf{v}_1$ for which $\nabla \times (\mathbf{v}_1 \cdot \nabla) \mathbf{v}_1 = 0$. Stagnation flows are an obvious choice to consider because they can lead to the build-up of thin current sheets. They also allow for flux to be brought into and removed from the localised non-ideal region and so change field-line connectivities away from this region.

Turning first to (3.4), we take ϕ_0 to be the function of the field line coordinates (x_0, y_0) given by

$$\phi_0 = \frac{\varphi_0}{\Lambda^2} x_0 y_0. \tag{3.35}$$

Setting $Z_0 = 0$, the inverse field line mappings (3.13) can be used to find an equivalent expression in terms of x, y, and z, so determining $\phi_0(x, y, z)$. The component of $\mathbf{v}_1$ perpendicular to $\mathbf{B}_0$ may then be deduced from (3.4) as

$$\mathbf{v}_{1\perp} = -\frac{\nabla \phi_0 \times \mathbf{B}_0}{|\mathbf{B}_0|^2}. \tag{3.36}$$

We use the freedom in choosing the component of $\mathbf{v}_1$ parallel to $\mathbf{B}_0$ to set the z-component of $\mathbf{v}_1$ to zero:

$$\mathbf{v}_1 = \mathbf{v}_{1\perp} - \frac{(\mathbf{v}_{1\perp})_z \mathbf{B}_0}{b_0}. \tag{3.37}$$

This ensures the flow is divergence-free since the z-component of the curl of equation (3.4) becomes $b_0 (\nabla \cdot \mathbf{v}_1) = 0$. Thus we obtain

$$\mathbf{v}_1 = \frac{\varphi_0}{b_0 \Lambda^2} (x \cosh(2kz) - y \sinh(2kz)) \, \hat{\boldsymbol{x}} + \frac{\varphi_0}{b_0 \Lambda^2} (x \sinh(2kz) - y \cosh(2kz)) \, \hat{\boldsymbol{y}},$$

and see that $\nabla \times (\mathbf{v}_1 \cdot \nabla) \mathbf{v}_1 = 0$. The ideal flow crosses the separatrices of $\mathbf{B}_0$ in the xy-plane, with streamlines of $\mathbf{v}_1$ above and below the central plane shown in Figure 3.10.

Since the inertial term in (3.8) may be expressed as the gradient of a scalar function, the equation has the same structure as in the case of the particular solutions (where $\mathbf{v}_1 = 0$), which were examined in Section 3.2. Thus the same form of $\mathbf{j}_2$ may be taken in both the particular and composite case, and continue to assume the form given by

$$\mathbf{j}_2 = \frac{j_{20}}{\cosh^2 \left(\frac{x^2 - y^2}{\lambda^2} \right)} \hat{\boldsymbol{z}},$$

as in the Subsection 3.2.2. A further comparison with the numerical simulation of Pontin et al. (2005a) can now be made; our ideal stagnation flow $\mathbf{v}_1$ in the central plane has a similar profile to the plasma flow at the end of their simulation when viewed with the correct orientation according to the current concentration.
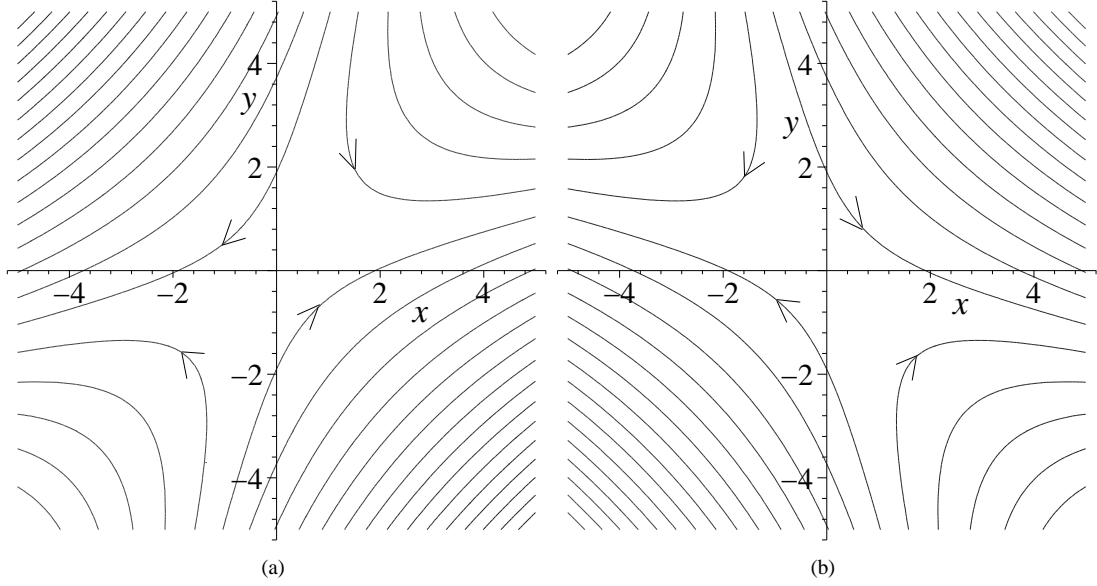
Figure 3.10: The ideal plasma velocity $\mathbf{v}_1$ for (a) $z = 0.5$ and (b) $z = -0.5$, and the parameters $\varphi_0 = 1$, $k = 0.5$, $b_0 = 2$, and $\Lambda = 1$.

Using (3.8) we deduce the pressure term p_2 as

$$p_2 = p_{20} - \tfrac{1}{2}k\lambda^2 b_0 j_{20} \tanh\left(\frac{x^2 - y^2}{\lambda^2}\right) - \frac{\varphi_0^2}{2\Lambda^2 b_0^2}\frac{\left(x^2 + y^2\right)}{\Lambda^2}. \tag{3.38}$$

The particular solution may be recovered by setting $\varphi_0 = 0$, and so it is seen that the inclusion of a zeroth-order flow has had the effect of introducing an extra term to the pressure, proportional to $\varphi_0^2/(\Lambda^4 b_0^2)$. When $\varphi_0 = 0$ there are strong gradients in the pressure along the separatrices of $\mathbf{B}_0$ in the xy-plane. This extra term has the effect of smoothing out these strong gradients, with p_2 becoming a smoother function as $\varphi_0^2/\Lambda^2 b_0^2$ is increased. An example of the pressure profile is shown in Figure 3.11, which can be compared with Figure 3.5 of Section 3.2. The additional term has a natural physical explanation. It deflects the incoming $\mathbf{v}_1$ flow toward the outflow direction, a purely hydrodynamical effect. Due to the symmetry with respect to inflow and outflow, there is no net transfer of magnetic energy to kinetic (bulk) energy of the plasma in this stationary solution, as would be expected in a more realistic situation. However, we may model part of this process by requiring $\mathbf{v}_1 \cdot \mathbf{j}_2 \times \mathbf{B}_0$ to be positive. This would result in an initial transfer of magnetic energy to kinetic energy, but with the latter subsequently transferred to potential energy, since $\mathbf{v} \cdot \nabla p > 0$, so no net acceleration can take place. We have here that

$$\mathbf{v}_1 \cdot \mathbf{j}_2 \times \mathbf{B}_0 = -\frac{\varphi_0 j_{20} k \left(\left(x^2 + y^2\right)\cosh\left(2kz\right) - 2xy\sinh\left(2kz\right)\right)}{\Lambda^2 \cosh^2\left(\frac{x^2-y^2}{\lambda^2}\right)}.$$

We require this quantity to be positive, which can be ensured by taking the combination $\varphi_0 j_{20} k < 0$.

Now turning to (3.5) we may use the same quantities $\hat{\eta}$, $\mathbf{E}_1$, and $\mathbf{v}_2$ as in Section 3.2.2 to satisfy the equation.
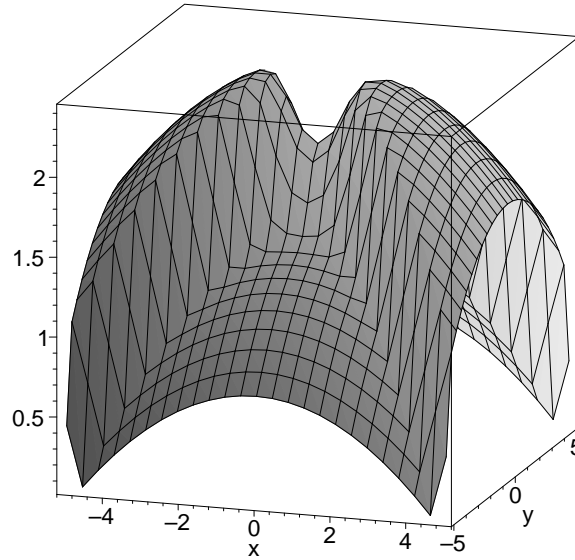
Figure 3.11: The pressure profile $p_2(x, y)$ when $\mathbf{v}_1 \neq \mathbf{0}$, $\mathbf{j}_2 = j_{20}/\cosh^2\left(\left(x^2 - y^2\right)/\lambda^2\right)\hat{\mathbf{z}}$, and the parameters $p_{20} = 2$, $b_0 = 2$, $\lambda = 1$, $k = 0.5$, $j_{20} = -1$, $\Lambda = 1$ and $\varphi_0 = 2$. The lower pressure regions correspond to inflow of $\mathbf{v}_1$ and the higher pressure regions to outflow.

The question that arises at this point then is: how do the particular and composite solutions differ? Or, in other words, what physical effect does the inclusion of the ideal flow $\mathbf{v}_1$ have on the solution? Since $\mathbf{E}_0$ is perpendicular to $\mathbf{B}_0$ the expression for the rate of reconnection is the same as that of the particular solution. However the non-vanishing external flow changes the meaning of this reconnection rate since the reconnection process can now reconnect flux outside the hyperbolic flux tube. The evolution of magnetic flux in the two cases is therefore quite different, and may be visualised using the concept of a magnetic flux velocity as described in Section 2.1. We demonstrate in the following subsection how the magnetic flux evolution differs between the particular and the composite solutions.

Magnetic flux that does not pass through the diffusion region evolves ideally, i.e. it is *frozen* into the flow and so initially-connected plasma elements remain connected. We may track the evolution of plasma elements in the ideal flow above and below the diffusion region. Initially-connected elements will only remain connected if the field line linking them does not pass through the non-ideal region; otherwise the elements will change their connectivity. The pair of quasi-flux velocities $\mathbf{w}_{in}$ and $\mathbf{w}_{out}$ can be used to project into the central plane ($z = 0$) the flow lines corresponding to the ideal evolution above and below the non-ideal region. Examining the differences between the lines of $\mathbf{w}_{in}$ and $\mathbf{w}_{out}$ allows us to deduce how the magnetic flux evolves.

For the stagnation flow described in Section 3.3(a), the relevant projection is shown in Figure 3.12 (for a particular choice of parameter values). The flow lines of $\mathbf{w}_{in}$ (grey lines) in the $z = 0$ plane are superimposed on those of $\mathbf{w}_{out}$ (black lines) in the same plane. We are able to divide the plane into three regions according to the type of reconnective behaviour that occurs; the separatrices dividing these regions are shown in Figure 3.13.

In region I the flow lines of $\mathbf{w}_{in}$ and $\mathbf{w}_{out}$ coincide perfectly. The magnetic flux passing through the
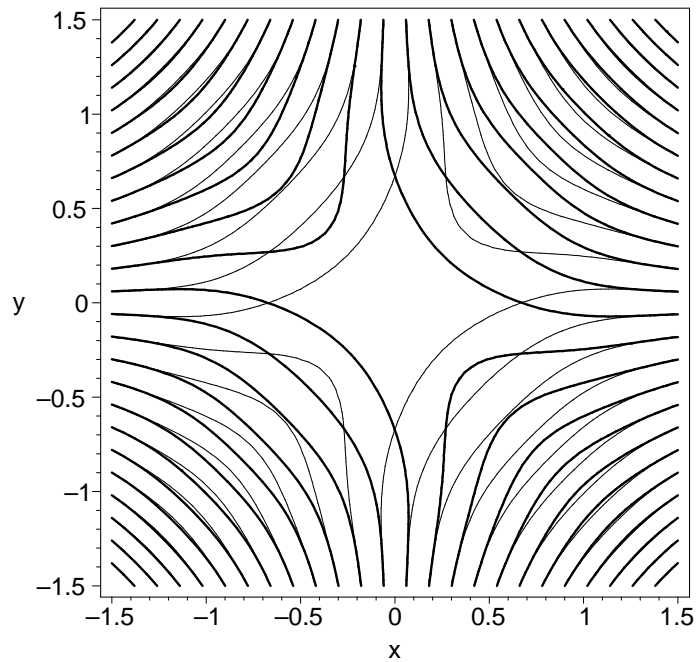
Figure 3.12: Flow $\mathbf{w}_{in}$ (grey) and $\mathbf{w}_{out}$ (black) for the solution already described in Section 3.3.
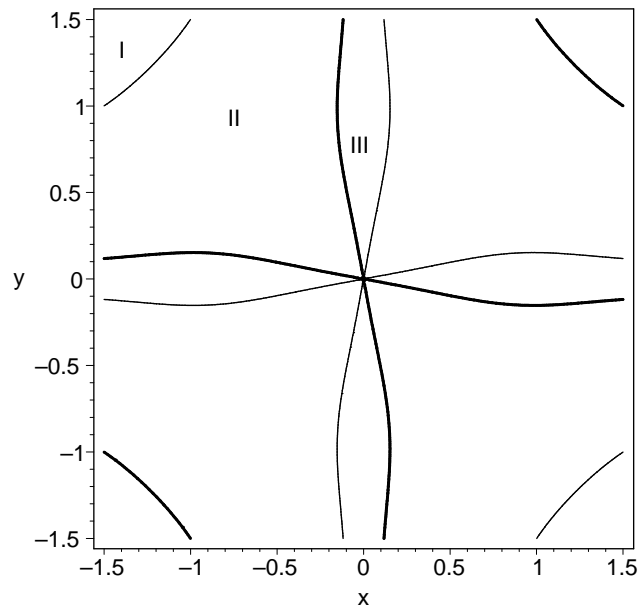
Figure 3.13: Separatrices of $\mathbf{w}_{in}$ (grey) and $\mathbf{w}_{out}$ black for the solution described in Section 3.3. The region is divided into three types of reconnective behaviour. Magnetic flux passing through region I undergoes ideal evolution. Magnetic flux passing through region II undergoes a slippage-like behaviour while flux passing through region II undergoes an evolution similar to that seen in classical 2D reconnection.

$z = 0$ plane in region I evolves ideally, so that initially-connected plasma elements will remain connected. In regions II and III the flow lines of $\mathbf{w}_{in}$ and $\mathbf{w}_{out}$ do not coincide. For magnetic flux passing through the $z = 0$ plane in these two regions we deduce that plasma elements above and below the non-ideal region that are initially connected will not remain so. Tracking the evolution of corresponding pairs allows us to distinguish different types of magnetic flux evolution.

Magnetic flux passing through region II exhibits a slippage-like behaviour. Initially connected plasma elements above and below the non-ideal region will change their connections as the flow transports the magnetic flux linking them into the non-ideal region. On leaving the shadow of the non-ideal region the initially connected elements are both transported in the same direction by the flow and a new ideal connection is again established for each plasma element. Although this connnection will not be with the initial partner, it will be with a plasma element that was initially close to that partner.

Magnetic flux passing through region III exhibits the type of behaviour most similar to that shown in classical 2D reconnection. Again, initially-connected plasma elements above and below the non-ideal region loose their connections as the magnetic flux linking them is transported into the non-ideal region. However, on leaving the shadow of the non-ideal region the initially-connected plasma elements above and below the non-ideal region are transported in different directions by the flow, along opposing 'wings' seen in Figure 3.13, and their separation will therefore increase in time, as in the classical 2D reconnection picture. The new ideal connection for a plasma element initially above (below) the non-ideal region will be with a plasma element that was initially below (above) the non-ideal region in the distant opposing wing.

Therefore in this composite solution the stagnation flow is dominant, with the rotational flow $\mathbf{v}_2$ present as a background flow. A stagnation flow was found to develop in the numerical simulations of Pontin et al. (2005a), although a background counter-rotational rotational flow was also shown to be present, and seen to fall off with distance from the X-line. The simulation also confirmed a continual and continuous change of field line connectivity. Thus many properties of their simulation are captured in the above-described analytical solution.

We have been able to make a direct comparison between the particular solutions described in Section 3.2 and the composite solutions described in this section since, for our choice of $\mathbf{v}_1$, the curl of the inertia term in (3.8) vanishes. In principle we could have chosen other ideal flows for this directly comparable analysis that also have a curl-free inertial term. One example is that which results from defining the scalar function ϕ_0 as the function of field-line coordinates given by

$$\phi_0 = \frac{\varphi_0}{\Lambda^2} \left(x_0^2 - y_0^2 \right),$$

from which we obtain

$$\mathbf{v_1} = \frac{-2\varphi_0}{b_0\Lambda^2} \left(y\hat{\mathbf{x}} + x\hat{\mathbf{z}} \right). \tag{3.39}$$

This is also a stagnation flow, but it differs considerably from the flow considered in the previous section; it does not cross the separatrices of the projection of $\mathbf{B_0}$ onto the xy-plane, and is independent of the third coordinate, z. When superimposed on the particular solution, however, the same three regions of differing flux evolution are present, as illustrated in Figure 3.14. The inflow and outflow channels bounded by the separatrices of the quasi-flux velocities are now centred around the separatrices of $\mathbf{B}_0$ in the $z = 0$ plane.
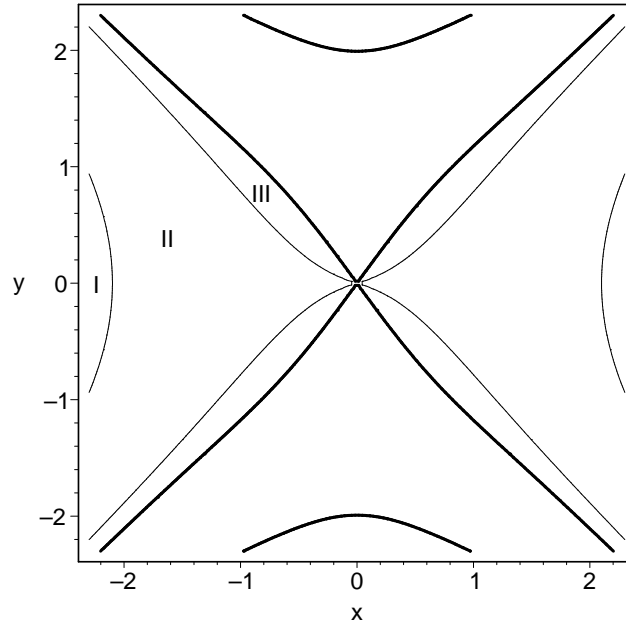
Figure 3.14: Separatrices of $\mathbf{w}_{in}$ (grey) and $\mathbf{w}_{out}$ black when $\mathbf{v}_1$ is given by (3.39). The same three types of reconnective behaviour as figure 3.13 are present.

This demonstrates one of the crucial differences between 2D and 2.5D reconnection and the 3D case. The crossing of the separatrices by the flow is only a criterion for reconnection in the 2D case. In 3D the difference between $\mathbf{w}_{in}$ and $\mathbf{w}_{out}$ is the crucial property for reconnection. Another example in this class of flows which can be used to form composite solutions is the rotational ideal flow arising from the choice

$$\phi_0 = \frac{\varphi_0}{\Lambda^2} \left(x_0^2 + y_0^2 \right). \tag{3.40}$$

This ideal flow is rotating in the same sense for all z, and so does not have the effect of bringing flux into and away from the non-ideal region.

For the three flows examined in this section, the reconnection rate, as determined by the integral of the parallel electric field along the reconnection line, is identical, but the magnetic flux evolution quite different. The distinct types of reconnective behaviour illustrated here, and in paper I, may be distinguished by considering the associated internal and external reconnection rates, as introduced by Hornig (2006).

The *external reconnection rate* measures the rate at which flux is transported into (and equivalently out of) the non-ideal region. This rate is always less than or equal to the total reconnection rate, and the *internal reconnection rate* measures the difference between the total reconnection rate and the external reconnection rate. The electric potential along the flow lines of $\mathbf{w}_{in}$ and $\mathbf{w}_{out}$ is constant, since these are streamlines of the ideal flow. The difference in electric potential between the inflow channels bounded by the separatrices of the flow therefore quantifies the external reconnection rate, while the internal reconnection rate is given by the difference between the total rate (measured by the integrated parallel electric field along the reconnection line) and the external reconnection rate.

The stagnation flow examples illustrated in Figures 3.13 and 3.14 both correspond to a purely external reconnection rate. In this situation the separatrices of the flow (which divide regions II and III) pass though the origin, and so the difference in the electric potential between them is equal to the total reconnection rate, i.e. the difference in electric potential across the non-ideal region. For an ideal rotational flow, such as that arising from the electric potential given by (3.40), the external reconnection rate vanishes and the reconnection is internal only. Similarly if the ideal flow is zero (as in the case of the particular solutions of paper I) then the reconnection is purely internal. Thus the interpretation of reconnection rate in this way allows for a clear distinction between the different types of solutions considered here.

We note also that a combination of internal and external reconnection is not excluded in these solutions, and is expected if a smooth transition between the purely external reconnection solutions illustrated in Figures 3.13 and 3.14 and the purely internal reconnection found in the particular solution is to be made. Such a solution exists when the magnitude of the ideal flow $\mathbf{v}_1$ is decreased to be the same, or less than, that of the non-ideal flow $M_e\mathbf{v}_2$. In addition to the three regions of differing space flux evolution described above and illustrated in Figure 3.13, the magnetic flux in these mixed solutions would show rotational dynamics within part of the HFT.

3.4   Accelerating Stagnation Flow

In a realistic situation we would expect to see a plasma flow that results in a net transfer of magnetic energy to kinetic (bulk) energy of the plasma since magnetic energy is the main source of energy in the solar corona. This property must be explicitly prescribed here since the model does not include the time-dependent processes external (and possibly prior) to the reconnection process that lead to the build-up of a current sheet and corresponding plasma flows. Instead these properties are represented in the model via boundary conditions on the flow, magnetic field and pressure profiles. Thus in the expansion scheme we may ensure an increase in kinetic energy occurs in the reconnection process by requiring $\mathbf{v}_1 \cdot \mathbf{j}_2 \times \mathbf{B}_0 - \mathbf{v}_1 \cdot \nabla p_2$ to be, on average, positive over the volume (which is not the case for the above stagnation flow). This increase in kinetic energy may be the result of a transfer of magnetic energy (due to $\mathbf{v}_1 \cdot \mathbf{j}_2 \times \mathbf{B}_0$), a transfer of thermal energy (due to $\mathbf{v}_1 \cdot \nabla p_2$) or a combination of both effects. Numerical experiments, such as those of Biskamp (1986), Priest and Forbes (1986), Linton and Priest (2003), Parnell and Galsgaard (2004) and von Rekowski et al. (2006), suggest considering a plasma flow that sharply changes its direction toward the outflow region; in such experiments fast jets of plasma emerging from the reconnection region are observed. We examine in this section an ideal plasma flow, $\mathbf{v}_1$, which possesses these properties, using a method similar to that of Section 3.2.1. Now, however, since the curl of the inertial term in (3.8) does not vanish, there is a much larger degree of coupling between equations (3.4) and (3.5), and the particular solution of Section 3.2 can no longer be used as a solution to (3.5).

Just as in the previous section we will consider incompressible solutions; a plasma flow with a faster outflow velocity than inflow velocity must have an associated outflow channel that is narrower than its inflow channel. To achieve such a flow we impose a non-symmetric function, ϕ_0, for the lowest order electric potential, and then deduce the plasma velocity $\mathbf{v}_1$ from (3.4). For example, we may impose ϕ_0 as

(a)   (b)   (c)
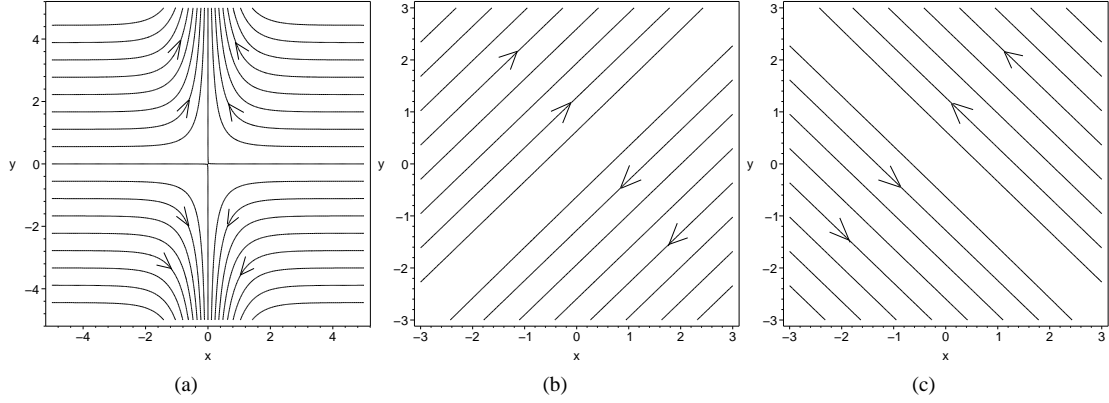
Figure 3.15: (a) Stagnation-point structure of the velocity field $\mathbf{v_1}$ corresponding to $\phi_0 = -\varphi_0 y_0 \tanh(x_0)/\Lambda^2$ in the plane $z = 0$. As indicated by the closeness of the contours, the plasma has a greater velocity along the outflow direction. In the planes (b) $z = 2$, and (c) $z = -2$, the flow is still of a stagnation type but is now stretched along the diagonal to such an extent that it is almost aligned with the $y = x$ and $y = -x$ lines, respectively.

the function of field line coordinates given by

$$\phi_0 = -\frac{\varphi_0}{\Lambda^2} y_0 \tanh(x_0), \tag{3.41}$$

and use the inverse field line mappings to deduce an equivalent expression in terms of x, y and z. An analytical expression for $\mathbf{v_1}$ (which is too long to be shown here, but may be easily calculated using any symbolic computation package) is found using (3.37). In the central region the flow has a stagnation structure, as shown in Figure 3.15, with single inflow and outflow channels that are of different widths. Thus, depending on the direction of the flow, and since it is incompressible, an acceleration or deceleration of the plasma takes place. The physically relevant case corresponds to the choice $\varphi_0 > 0$, for which the outflow direction is the narrower channel along the y-direction, and so the plasma is accelerated during the reconnection process.

Turning now to the lowest-order momentum equation in the expansion scheme, (3.8), we integrate along the field lines (3.12), starting from the plane $z = 0$ to deduce the pressure p_2:

$$p_2(x, y, z) = -\int_{s=0}^{z/b_0} (\mathbf{v}_1 \cdot \nabla \mathbf{v}_1) \cdot \mathbf{B}_0 \, ds + p_2(x_0, y_0). \tag{3.42}$$

We first examine solutions obtained when the free function $p_2(x_0, y_0)$ is set to zero. Later in the section we shall consider another particular example where $p_2(x_0, y_0) \neq 0$, and show that the choice of this free function has a considerable effect on the reconnection process.

An example of the pressure profile in the case where $p_2(x_0, y_0) = 0$ is shown in Figure 3.16(a). The expression obtained for p_2 is dependent on φ_0^2, and so the pressure profile is independent of the flow direction. Thus for the case $\varphi_0 > 0$ which we are considering here, a pressure gradient exists along the outflow direction which is in the direction of the flow, and so acts to accelerate the plasma.

The perpendicular component of the current, $\mathbf{j}_{2\perp}$, can be determined analytically from (3.8) once the

(a) (b)
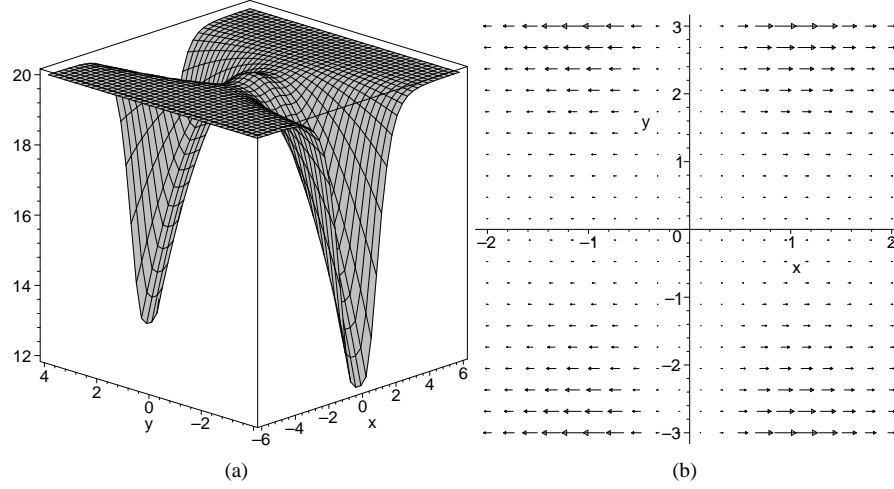
Figure 3.16: (a) The pressure profile p_2 and (b) the Lorentz force $\mathbf{j}_2 \times \mathbf{B}_0$ in the plane $z = 0$ for an accelerating stagnation flow $\mathbf{v}_1$. The free function $p_2\,(x_0, y_0)$ in equation (3.42) has been set to zero. The outflow is aligned with the y-axis, and corresponds to the channel of decreasing pressure.

pressure is given:

$$\dot{\mathbf{j}}_{2\perp} = \frac{(-\nabla p_2 - (\mathbf{v}_1 \cdot \nabla)\,\mathbf{v}_1) \times \mathbf{B}_0}{|\mathbf{B}_0|^2}.$$

A Lorentz force is present within the outflow channels, and is directed away from the central line of minimum pressure, as shown in Figure 3.16(b). Thus, since it is not aligned with the flow direction, this force does not act to alter the plasma velocity; in this example it is only the pressure gradient which accelerates the plasma, causing the fast outflow jets. The quantity $\mathbf{v}_1 \cdot \mathbf{j}_{2\perp} \times \mathbf{B}_0 - \mathbf{v}_1 \cdot \nabla p_2$ is, on average, positive over the region provided $\varphi_0 > 0$, i.e. provided the flow is accelerated from its inflow to outflow direction. This net acceleration, a consequence of the pressure gradient, results in a net transfer of thermal energy to kinetic energy.

The full form of the current $\mathbf{j}_2$ may be determined by finding a scalar function $\lambda\,(x, y, z)$ such that setting $\mathbf{j}_2 = \mathbf{j}_{2\perp} + \lambda\mathbf{B}_0$ ensures the current is divergence-free. Taking $\nabla \cdot \mathbf{j}_{2\perp} + \nabla\lambda \cdot \mathbf{B}_0 = 0$ and integrating along the field lines gives

$$
\begin{aligned}
\lambda(x, y, z) &= -\int_{s=0}^{s=z/b_0} \nabla \cdot \mathbf{j}_{2\perp}\,ds + \lambda\,(x_0, y_0) \\
&= \tilde{\lambda}(x, y, z) + \lambda(x_0, y_0),
\end{aligned}
\tag{3.43}
$$

where $\lambda\,(x_0, y_0)$ is a function that we are free to impose on the solution. The current is then given by

$$\mathbf{j}_2 = (\,\mathbf{j}_{2\perp} + \tilde{\lambda}(x, y, z)\mathbf{B}_0) + \lambda(x_0, y_0)\mathbf{B}_0 = \tilde{\mathbf{j}}_2 + \mathbf{j}_2^*,$$

where $\mathbf{j}_2^*$ is solely determined by the free function $\lambda\,(x_0, y_0)$. The term $\mathbf{j}_2^*$ also determines the current along the z-axis because, due to the vanishing divergence of $\mathbf{j}_{2\perp}$ along the z-axis, the the z-component of $\tilde{\mathbf{j}}_2$ vanishes there. Equation (3.5) then implies that the reconnection rate will be determined by this free function (together with the form of $\hat{\eta}$), rather than by the ideal flow $\mathbf{v}_1$, i.e. governed by the lowest order
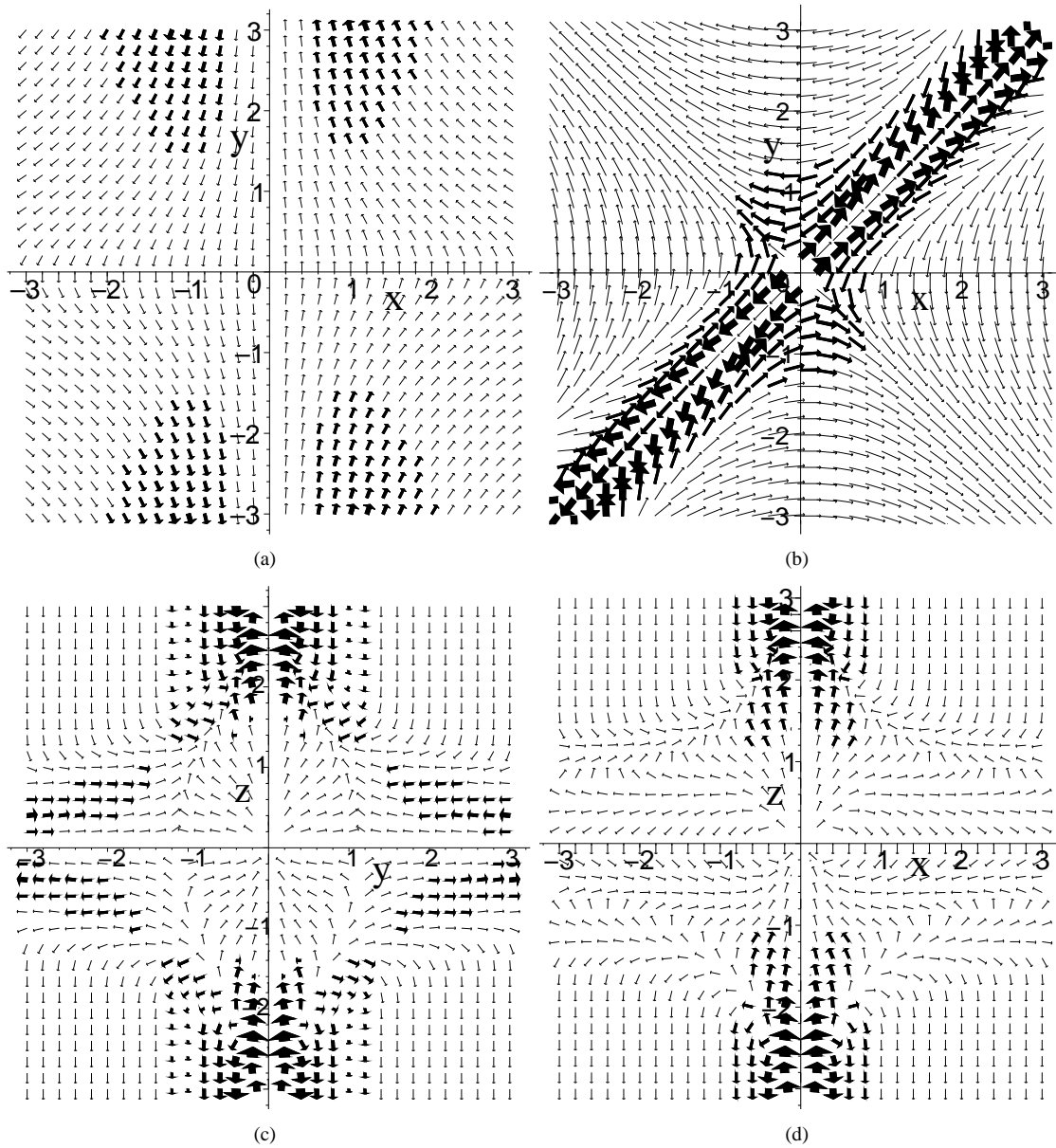
Figure 3.17: Vector-field plot showing the current $\tilde{\mathbf{j}}_2$ in the planes (a) $z = 0$, (b) $z = 2.2$, (c) $x = 0$, (d) $y = 0$, in the case where $p_2\left(x_0, y_0\right) = 0$ with the parameters $\varphi_0 = 1$, $\Lambda = 1$, $b_0 = 1$, and $k = 1$. The thickness of each arrow represents the magnitude of the current vector at that point and the same scaling for the vectors has been used for each of the plots.

(a)   (b)
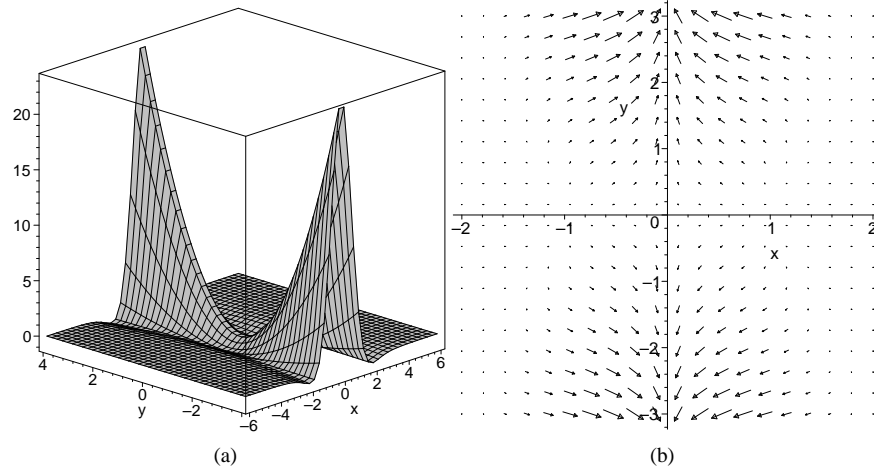
Figure 3.18: (a) The pressure profile p_2 and (b) the Lorentz force $\mathbf{j}_2 \times \mathbf{B}_0$ for the accelerating stagnation flow, now with free function $p_2\left(x_0, y_0\right)$ in equation (3.42) given by (3.44). The outflow is aligned with the y-axis, and corresponds to the channel of increasing pressure. This figure may be compared with figure 3.16.

non-ideal solution.

Equation (3.43) must be integrated numerically. Figure 3.17 illustrates the current, $\tilde{\mathbf{j}}_2$, in the planes $z = 0$, $y = 0$ and $x = 0$ and $z = 2$ (for clarity the full 3D grid has not been shown). It can be seen that the strongest currents are present in the regions where the plasma velocity $\mathbf{v}_1$ is changing rapidly in direction or magnitude. Thus in the central plane, $z = 0$, as shown in Figure 3.17(a), strong currents are found along the fast outflow jets (see Figure 3.15(a)). Above and below the central region strong currents are present around the lines $y = x$ for $z > 0$ (see Figure 3.17(b)) and $y = -x$ for $z < 0$ (by symmetry), corresponding to the flow channels illustrated in Figure 3.15(b) and (c). The current structure along these flow channels is seen to be complex, with oppositely directed current along and around the lines $y = \pm x$. Away from these regions the current is very weak and has an X-type structure in planes of $z = const$.

We can make use of the freedom to choose the free function $p_2\left(x_0, y_0\right)$ that arises in the integration for p_2 given by equation (3.42). This function may be chosen to alter the pressure profile, and consequently also the current $\mathbf{j}_2$. In particular, a form for $p_2\left(x_0, y_0\right)$ may be imposed such that the acceleration of the plasma is driven by the Lorentz force, $\mathbf{j}_2 \times \mathbf{B}_0$, rather than by the pressure gradient, $-\nabla p_2$.

One such example is obtained by adding the additional function given (in terms of the fieldline coordinates) by

$$p_2\left(x_0, y_0\right) = p_{20}\, e^{-x_0^2}\left(y_0^2 - x_0^2\right) \tag{3.44}$$

to the pressure p_2. The resultant pressure profile is illustrated in Figure 3.18(a), where it is seen that the pressure gradient is still directed along the outflow channel, but now acts against the direction of the flow. Therefore, the acceleration of the plasma is driven entirely by the Lorentz force, with magnetic energy being transfered to kinetic energy in the reconnection process. The Lorentz force is illustrated in Figure 3.18(b), where the perpendicular component of the current $\mathbf{j}_2$ has been deduced using the same method as described above. The divergence of $\mathbf{j}_{2\perp}$ along the z-axis remains zero with the inclusion of the extra factor in the

solution for p_2. Thus the reconnection rate in this case is still determined completely by the free function $\lambda(x_0, y_0)$, and may therefore be the same as in the previous pressure gradient driven model.

In both of the examples in this section we must impose a localised resistivity in order to ensure a localised non-ideal region. In principle the remaining quantities could then be determined numerically using the iterative scheme outlined in Section 3.2.

3.5   Summary

In this chapter we have carried out a perturbation expansion of the 3D stationary MHD equations in the limit of slow flow. In a series of examples the system has been solved explicitly up to third order, and a scheme outlined to allow a (numerical) solution at all higher orders to be obtained.

The expansion scheme allows for a decomposition of Ohm's law into an ideal and a non-ideal part at zeroth- and first-order, respectively, together with accompanying equations of motion. Such a decomposition of non-ideal, or particular, solutions and ideal solutions has been suggested by previous kinematic analyses (e.g. Hornig and Priest, 2003, Pontin et al., 2004, 2005b) but in this chapter we have shown that expressing solutions in this way is possible, under certain circumstances, even when the equation of motion is also included in the analysis.

In Section 3.2, by assuming the trivial solution for the zeroth-order terms (excluding the magnetic field), we were able to examine the non-ideal solution alone. This directly corresponds to the pure solutions examined by Hornig and Priest (2003). In the analysis of particular solutions we examined two different magnetic fields, corresponding to a uniform current and to a current localised along the separatrices of the basic magnetic field. In these solutions, counter-rotating flows above and below the non-ideal region are observed that are limited to within the HFT threading the non-ideal region. The same reconnection rate is observed in both examples, since the parallel electric field is, to some extent, independent of the choice of current. Further, with respect to the reconnection rate, the dimensions of the non-ideal region are important only along the reconnection line (i.e. the line of maximal $\Delta\phi_2$ across the non-ideal region, and identified here with the z-axis) – its extent and structure in the xy-plane is unimportant.

The structure of the plasma flow in the particular solution means that the reconnection is limited to affect the field lines within the HFT only. The inclusion of non-trivial solutions to the zeroth-order equations equates to the case of 'composite solutions' in Hornig and Priest (2003). A stagnation flow is natural to consider; such a flow would bring field lines into the non-ideal region, and so allow field line connectivity further away from this region to be changed, i.e. allow the reconnection process to have a global effect.

Examining the expansion scheme equations it is clear that the equation of motion provides a certain degree of coupling between the ideal and non-ideal solutions. Using some example flows, we have considered in Section 3.3 to what extent such a coupling restricts the form of ideal solution and have considered the effect of the ideal solution on the reconnection rate, evolution of flux and energetics. A particular class of ideal flows, for which the inertial term in the equation of motion can be expressed as a gradient, may be imposed on the particular non-ideal solution without altering the form of the current, parallel electric

field or (in consequence) the reconnection rate. For these flows the coupling between the two solutions is relatively weak, affecting only the pressure term in the non-ideal solution. A wide range of flows, both in strength and, more importantly, in profile, belong to this class of solution. They may be distinguished by their effect on the evolution of magnetic flux.

In general, stagnation flows are expected to be present if classical reconnection is to occur, since they allow thin current sheets to be built up and so localised non-ideal regions to become established. A variety of symmetric stagnation flows belong to the class of ideal flows that may be used to form composite solutions. These flows bring magnetic flux into the non-ideal region from large distances and subsequently remove the flux. Magnetic flux threading particular channels in the centre of the region shows similar behaviour to typical 2D reconnection, in the sense that field lines brought in toward the non-ideal region reconnect with field lines that were initially far away, and the separation of initially connected plasma elements increases in time after the flux has left the non-ideal region. In the same reconnection event, magnetic flux passing through other regions of the domain can be seen to undergo a slippage-like behaviour. Although the reconnection rate in the particular and composite reconnection solutions is quantitatively the same, its physical interpretation is quite different. The reconnection, which was completely internal for the particular solution, is now completely external for these stagnation flows, and this remains the case whether or not the flow crosses the separatrices of the magnetic field in the xy-plane.

In such symmetric examples there is no net transfer of magnetic energy to bulk energy of the plasma. Non-symmetric stagnation flows, however, such as those considered in Section 3.4 can convert magnetic energy into kinetic energy. These ideal flows show highly curved streamlines, with fast jets of plasma emerging from the central region. Although a stronger coupling between the ideal and non-ideal solutions is present in this situation, we have shown that, just as in the non-accelerating case, the ideal flow itself does not directly govern the reconnection rate, which is instead, within the limitations of this model, determined by a function that is free to be imposed on the solution. In a numerical simulation this free function, which determines in particular the parallel current along the reconnection line, will be defined by the boundary values for the magnetic field. We have shown how the choice of different free functions within the expansion scheme results in differing physical reconnection scenarios; by considering two particular free functions we have illustrated how an acceleration of the plasma may be driven by a Lorentz force or by a pressure gradient. In general, a combination of both effects is also possible.

Finally we note that the expansion scheme has been set up on an infinite domain and that the solutions are valid near the centre of the domain. In a real, finite, physical system, the type of solution obtained in a stationary reconnection event will depend on the initial and boundary conditions that are imposed. In addition, the dimensions of the non-ideal region will be dependent on the dynamics of the event prior to the onset of the stationary phase, for example on the process of current sheet formation. Thus the various choices that have been considered here for the free functions in the expansion scheme, and so the type of reconnection solution achieved in practice, will depend on such conditions. However, each order of the expansion includes enough free parameters to make the magnitude of the new contributions ($\mathbf{v}_i$, $\mathbf{B}_i$) essentially free, and independent of the lower-order solutions. We are hopeful therefore that the example solutions found are good approximations to full exact solutions, in that the infinite series represented in each case may be convergent (provided $M_e \ll 1$). Whether the solutions are dynamically accessible cannot be determined within the scheme.

Chapter 4

Flux-Tube Disconnection

Analytical models for 3D non-null reconnection have, so far, been based on a hyperbolic field geometry. However, as discussed in Section 2.2, in 3D it is the location of non-ideal terms rather than the field geometry that will determine the location of reconnection. In this chapter we present a model for flux-tube disconnection, where an elliptic geometry is taken for the magnetic field. The model is developed to describe a steady-state situation in which the two footpoints of a magnetic flux tube are being spun in opposite directions and in this stationary state a twist is present in the centre of the flux tube where a region of localised current is present and reconnection is taking place. A qualitative description of the systems evolution is presented in Section 4.2, with a detailed analytical model given in Section 4.3. The model may be categorised as an example of global non-null reconnection under *General Magnetic Reconnection*, a theory we summarize in Section 4.1. Several features of previous (hyperbolic) models of non-null reconnection are found.

The results of this chapter can be found in Wilmot-Smith and Priest (2007).

4.1   General Magnetic Reconnection

There are several features of 2D reconnection models, for example a plasma flow across the separatrices of the magnetic field, or a normal electric field component at the X-point, that have been proposed as general definitions for reconnection. It was not until more general, 3D, circumstances were considered that the appropriateness of each of these conditions became clear.

Schindler et al. (1988) first considered how applicable these ideas might be to 3D geometries, and argued that any general definition should be structurally stable, i.e. not depend on small modifications to the system under consideration. They proposed that a definition, first considered by Axford (1984), based on a change of connectivity of plasma elements due to a localised violation of the frozen-in field condition,

```
        ┌─────────────────────────┐
        │  BREAKDOWN OF MAGNETIC  │
        │       CONNECTION        │
        └─────────────────────────┘
```
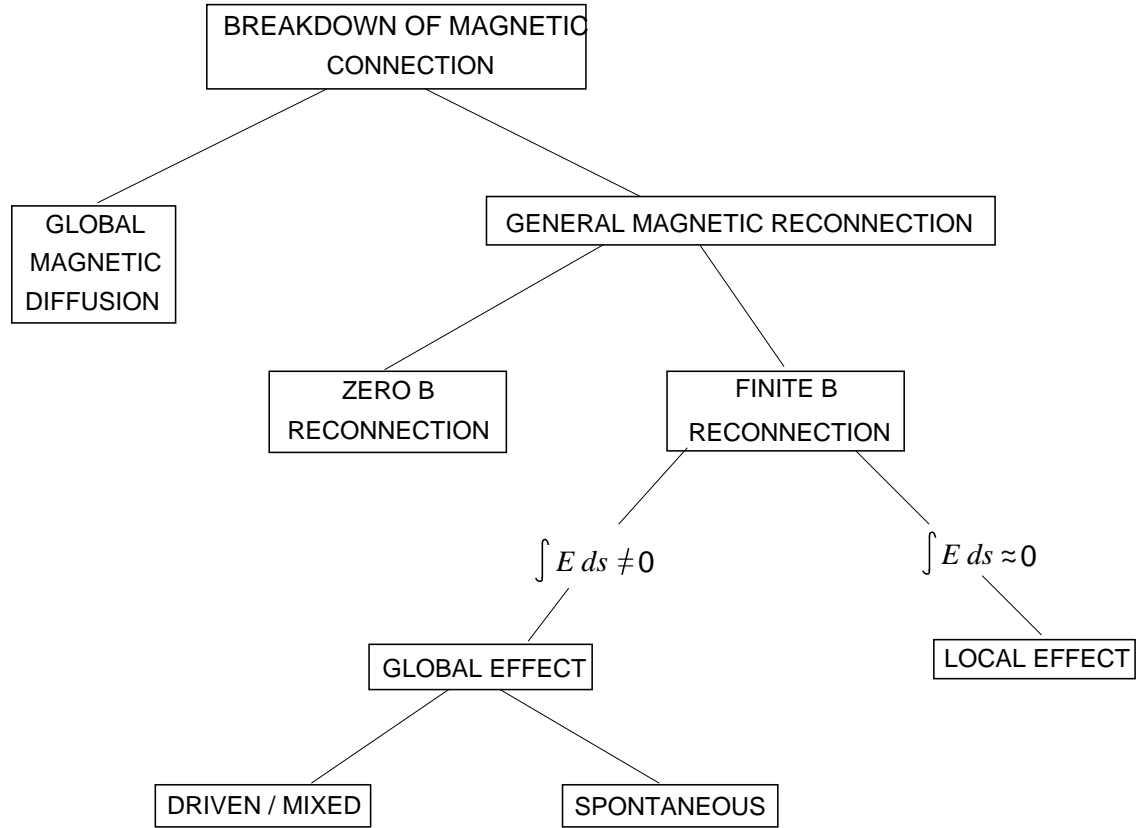
Figure 4.1: Classification of breakdown of magnetic connection according to Schindler et al. (1988). Various branches of General Magnetic Reconnection are shown. Reconnection is classed as *global* when a change in magnetic connectivity occurs for plasma elements that do not themselves pass through the non-ideal region.

should be used. This is the basis of *General Magnetic Reconnection* (GMR). The condition

$$\int E_{\parallel} dl \neq 0,$$

evaluated along a field-line, is required for GMR, being a generalisation to 3D of the 2D normal electric field component at an X-point. In order to distinguish between reconnection and diffusive processes, the additional requirement that the non-ideal term in Ohm's law (which itself is the cause of the breakdown of the frozen-in condition) be localised is also imposed. Equivalently, GMR applies only to situations where $R_{me} \gg 1$, i.e. the global magnetic Reynolds number is large. Figure 4.1 illustrates the regimes of breakdown of magnetic connection and so also the branches of general magnetic reconnection (Schindler et al., 1988). The breakdown of magnetic connection may be caused by a resistive term in Ohm's law, but also by other non-ideal terms, such as the pressure tensor.

Finite-B reconnection assumes the magnetic field does not vanish within the non-ideal region, and may be classified further as *local* or *global* according to how the change in connectivity arises. If a change in magnetic connectivity occurs for plasma elements that do not themselves pass through the non-ideal region then the process is global; otherwise it is local. The change in connectivity necessarily involves plasma

elements located on different sides of the non-ideal region, and reconnection occurs only for elements which are, at some time, connected to the non-ideal region.

As the authors pointed out, the separation of plasma elements that results from the reconnection process may be a factor in reconnection modelling, and a reason why several scenarios which fit into the GMR scheme have not been extensively modelled. Stagnation flows, which lead to large separations, may be a feature of 3D models not because they cross the separatrices of the field, but rather because of the separation of plasma elements they cause. Models of finite-B reconnection have shown that *counter-rotating* flows are a distinguishing feature of the 3D case (Hornig and Priest, 2003, Pontin et al., 2005a, Wilmot-Smith et al., 2006a), and that the orientation of stagnation flows with respect to the field structure is not important (Wilmot-Smith et al., 2007a).

Magnetic reconnection models in which the magnetic field has an O-type topology have not received much attention. Recently, however, De Moortel and Galsgaard (2006a,b) presented numerical simulations of 3D reconnection due to rotational and spinning motion of the footpoints of magnetic flux tubes. In their simulations stagnation flows were observed, together with an X-type current structure, although the magnetic field showed an O-type configuration in cross-sectional planes. We return to examine and extend these models in Chapter 5. Here we present a much simpler picture, which allows for analytical modelling, of reconnection that occurs as a result of the counter-rotation of the ends of a magnetic flux tube, which we refer to as *flux-tube disconnection*. A qualitative description of the process is outlined in the next section, with a more detailed model given in Section 4.3.

4.2   Qualitative Model

Consider a steady-state situation (Figure 4.2) where a magnetic flux tube, of radius a, has footpoints located at $z = \pm H$ and a typical vertical magnetic field strength b_0. Assume that the two footpoint ends are being rotated in different directions with speed v_0, and that, as a result of the counter-rotation, a twist in the field is produced within $z = \pm L$. That is, assume that within the non-ideal region the magnetic field may be written as

$$\mathbf{B} = B_\theta \hat{\boldsymbol{\theta}} + B_z \hat{\mathbf{z}}, \approx k b_0 \hat{\boldsymbol{\theta}} + b_0 \hat{\mathbf{z}},$$

where k is a constant indicating the order of magnitude ratio of the toroidal field strength to the guide field. The flow is assumed to be incompressible, which is satisfied automatically for a purely azimuthal plasma velocity that is independent of θ.

The localised poloidal field component results in a current, and therefore a non-ideal region, that is localised in all three dimensions. The current has a component parallel to the magnetic field, and does not close within the non-ideal region; we assume that the return current is diffuse and is spread over a sufficiently large volume that its local effect may be neglected. A sketch of the current structure is shown in Figure 4.3.

Several questions now arise in the analysis. How, in an order of magnitude sense, is the twist in magnetic field related to the driving plasma velocity v_0. Specifically, how do the parameters L and k, which determine
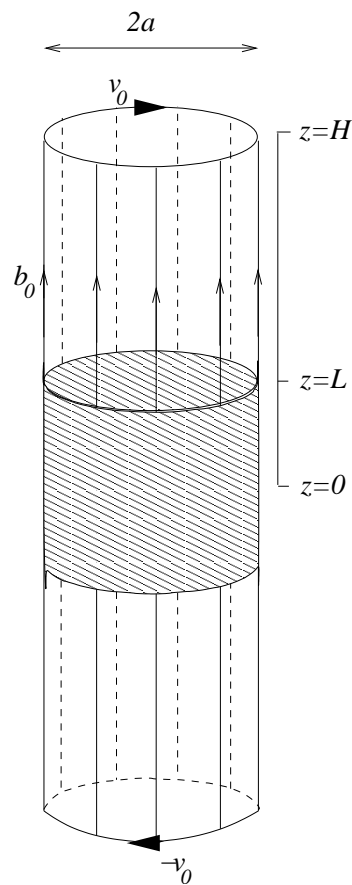
Figure 4.2: Sketch illustrating the model for flux-tube disconnection. A flux tube of radius a is anchored at its footpoints $z = \pm H$ which are rotated in opposite directions with speed v_0. The counter-rotation generates a localised twist within the flux tube in the shaded region, i.e. between $z = \pm L$.
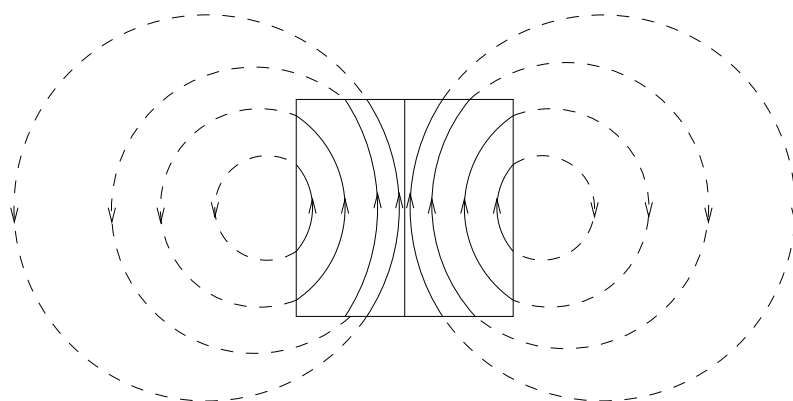
Figure 4.3: Sketch illustrating the form of the current generated by the counter-rotation of the flux-tube footpoints. The box indicates the boundaries of the non-ideal region. A strong current (solid black lines) gives rise to the localised non-ideal region, with the weak return current (dashed lines) being diffuse.
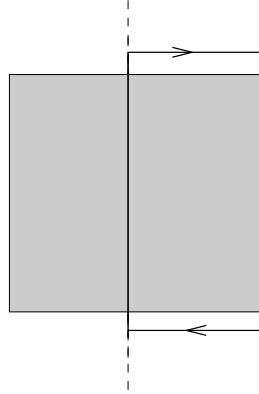
Figure 4.4: Path taken to consider a loop integral consisting of the central field line, a field line along the boundary of the non-ideal region (shaded) and two connecting radial lines. The integral of the electric field around the loop (solid black lines) must vanish due to the stationarity of the process. The central axis indicated by a dashed line.

the extent of the non-ideal region and the strength of the poloidal field, respectively, depend on v_0? Which parameters determine the rate of reconnection? How is the rate of reconnection dependent on the driving velocity v_0?

We can gain an insight into these questions by examining Ohm's law and Faraday's law for a steady state:

$$\mathbf{E} + \mathbf{v} \times \mathbf{B} = \frac{1}{\sigma}\mathbf{j},$$

$$\nabla \times \mathbf{E} = \mathbf{0},$$

where σ is the electrical conductivity. Consider the ideal region above and below $z = \pm L$. There $\mathbf{j} = 0$, and Ohm's law reduces to

$$E_r + v_0 b_0 = 0, \tag{4.1}$$

where E_r is the typical radial electric field. Similarly, along the central axis ($r = 0$) the plasma velocity is zero by symmetry and

$$E_z = \frac{1}{\sigma}j_z. \tag{4.2}$$

Now, $\nabla \times \mathbf{B} = \mu\mathbf{j}$ implies that along the axis we also have

$$j_z = \frac{1}{\mu}\left(\frac{B_\theta}{r} + \frac{\partial B_\theta}{\partial r}\right) \approx \frac{2kb_0}{\mu a}. \tag{4.3}$$

Next consider a loop integral, as illustrated in Figure 4.4, consisting of the part of the central field line from below to above the non-ideal region, a field line on the boundary of the non-ideal region, and two connecting radial lines. Integrating around this loop and using Faraday's law and using the symmetry of solutions above and below the z-axis gives

$$0 = \oint \mathbf{E} \cdot d\mathbf{l} \approx 2LE_z + 2aE_r, \tag{4.4}$$

since the electric field along the boundary of the non-ideal region vanishes. Substituting expressions (4.1),

(4.2) and (4.3) into relation (4.4) allows us to eliminate the electric fields E_r and E_z and obtain an expression for the plasma velocity in terms of the field parameters:

$$v_0 = \frac{2\eta k L}{a^2},$$ (4.5)

where $\eta = 1/(\mu\sigma)$ is the magnetic diffusivity. This expression allows us to determine the product kL when the radius of the tube (a) and the rotational driving velocity (v_0) are given. For example, if we keep the height of the non-ideal region (L) fixed, any increase in v_0 must be reflected by an increase in the poloidal field strength (k) i.e., the number of turns the field makes within the non-ideal region must increase. Similarly, we could have kept k fixed but increased L; this would also have the effect of increasing the number of turns the field makes within the non-ideal region. Therefore we deduce that the effect of an increase in rotation speed (v_0) is to increase the number of turns of the field, whether through a lengthening of the non-ideal region or by an increase in the number of turns of the field within the non-ideal region.

Equation (4.5) is the basic expression for the rotational velocity (v_0) in terms of the magnetic diffusivity (η), the dimensions (a, L) of the diffusion region and the ratio (k) of rotational to axial field strength. It is interesting to see how it differs from the corresponding simple expression ($v_0 = \eta/a$) for the inflow into a Sweet-Parker diffusion region, since here we have the extra factors k and L/a that arise from the three-dimensionality of our process. The first factor arises essentially because we have a twisting process and the second because the electric field components E_z and E_r differ in magnitude.

We may also make an estimate of the rate of reconnection ($d\Phi_{rec}/dt$), i.e. the rate of change of magnetic flux. This rate is given by the integral of the parallel electric field along the reconnection line, i.e. along the central axis:

$$\frac{d\Phi_{rec}}{dt} = \int E_{\parallel} dl \approx 2L E_z \approx \frac{4\eta k b_0 L}{a} = 2b_0 a v_0,$$ (4.6)

where the above expressions, (4.1), (4.2) and (4.3), have been used. This shows us that the rate of reconnection is proportional to the rotational driving velocity. The reconnection rate may be interpreted as the rate at which all the field lines within the flux tube are changing their connections, and so this estimate of the reconnection rate agrees with our intuitive understanding of the process. In dimensionless terms we have

$$\frac{d\bar{\Phi}_{rec}}{dt} = 2\frac{a}{H}\frac{v_0}{v_A}.$$ (4.7)

Thus the dimensionless reconnection rate is proportional to the Alfvén Mach number (v_0/v_A) of the driving flow and the ratio (a/H) of the non-ideal region radius (a) to the ambient scale height (H). Thus, if a/H and v_0/v_A are significant fractions of unity we have fast reconnection, i.e., at a significant fraction of the Alfvén speed; otherwise the reconnection is slow (see section 5).

In the next section we present an analytical model for the reconnection process described above. We show that the exact kinematic solution obtained there agrees with the intuitive understanding developed in this section.

4.3   Quantitative Model

We present here an axisymmetric analytical model for flux tube disconnection. The model is kinematic (i.e. the equation of motion is neglected) and stationary, and satisfies the following equations:

$$\mathbf{E} + \mathbf{v} \times \mathbf{B} = \frac{1}{\sigma}\mathbf{j}, \tag{4.8}$$

$$\boldsymbol{\nabla} \times \mathbf{E} = \mathbf{0}, \tag{4.9}$$

$$\boldsymbol{\nabla} \times \mathbf{B} = \mu\mathbf{j},$$

$$\boldsymbol{\nabla} \cdot \mathbf{B} = \mathbf{0},$$

$$\boldsymbol{\nabla} \cdot \mathbf{v} = \mathbf{0}.$$

Several of the previous 3D analytical models of reconnection which have helped to increase our understanding of the process have been kinematic (Lau and Finn, 1991, Hornig and Priest, 2003, Pontin et al., 2005b). They have demonstrated many features of 3D reconnection that are not present in 2D but which are also seen in numerical experiments (Pontin et al., 2005a) and dynamic analytical models (Wilmot-Smith et al., 2006a, 2007a). A typical feature of reconnection in astrophysical plasmas is that non-ideal regions are localised in 3D as a result of intense current concentration. In such regions the resistivity is expected to be enhanced by current-driven microinstabilities. We therefore consider here a magnetic field that leads to a localised current, and additionally impose a localisation of the resistivity. This is one of the features that distinguishes our model from previous kinematic models where a localised non-ideal region was obtained through an enhancement of the resistivity alone.

Working throughout in cylindrical coordinates (r, θ, z), the magnetic field is prescribed as

$$\mathbf{B} = 2b_0 k \frac{r}{a} \exp\left(-\frac{r^2}{a^2} - \frac{z^2}{L^2}\right)\hat{\boldsymbol{\theta}} + b_0\hat{\mathbf{z}}.$$

The azimuthal component of the magnetic field is localised and so generates a twist in the magnetic field close to the origin, while at large distances the field is uniform in the z-direction. The width of the flux tube is dependent on the parameter a, the extent of the twist in the z-direction on the parameter L, and the ratio of the toroidal field to the guide (or axial) field given by the parameter k. Some typical field lines are illustrated in Figure 4.5; note that each field line remains on a surface of constant radius.

This simple field configuration allows for a direct integration to find the equations of the field lines. This proves to be useful later, where we integrate along the field lines in order to obtain expressions for the remaining terms.

The equations, $\mathbf{R}(r_0, \theta_0, s) = (R, \Theta, Z)$, of the field lines passing through the point $(r_0, \theta_0, z = 0)$ are given by

$$R = r_0,$$
$$\Theta = 2b_0 k \frac{r_0}{a}\ s\ \exp\left(-\frac{r_0^2}{a^2} - \frac{b_0^2 s^2}{L^2}\right), \tag{4.10}$$
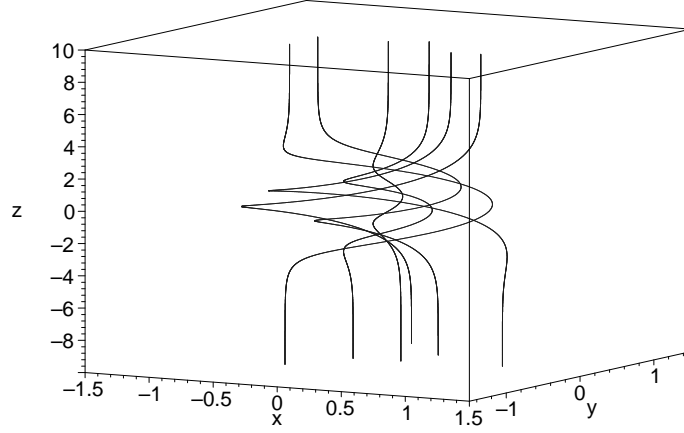
Figure 4.5: Some typical field lines threading the non-ideal domain, for parameters $k = 1$, $a = 1$, $L = 3$, $b_0 = 1$.

$$Z = b_0 s.$$

The inverse mapping, $\mathbf{R}_0 (r, \theta, s) = (R_0, \Theta_0, Z_0)$, is given by

$$
\begin{aligned}
R_0 &= r, \\
\Theta_0 &= 2 k b_0 s \frac{r}{a} \exp\left(-\frac{r^2}{a^2} - \frac{b_0^2 s^2}{L^2}\right), \\
Z_0 &= -b_0 s.
\end{aligned}
\tag{4.11}
$$

The twist of the flux tube generates closed poloidal rings of current, given by

$$
\mathbf{j} = \frac{4 b_0 k}{\mu a} \exp\left(-\frac{r^2}{a^2} - \frac{z^2}{L^2}\right) \left(\frac{rz}{L^2} \hat{\mathbf{r}} + \frac{a^2 - r^2}{a^2} \hat{\mathbf{z}}\right).
$$

An example is shown in Figure 4.6, where the current is seen to be is localised in three-dimensions around the origin, and has its greatest strength along the axis of the flux tube. Now the non-ideal term, $\frac{1}{\sigma} \mathbf{j}$ in Ohm's law (4.8) would already be localised given a uniform electrical conductivity, σ. Here, however, we choose to impose in addition a form for $1/\sigma$ leading to a localised magnetic diffusivity η. We take

$$
\eta = \frac{1}{\sigma_0 \mu} \exp\left(-\frac{4r^2}{a^2} - \frac{z^2}{L^2}\right).
\tag{4.12}
$$

Regions of intense current concentration are expected to give rise to enhanced diffusivity, and so this provides a motivation for the form for η chosen here. We take the non-ideal region, D say, to be inside the surface defined by $|\mathbf{j}|/\sigma = 0.02 \, (|\mathbf{j}|/\sigma)_{\max}$. The expression (4.12) has been chosen such that there is no return-current within D. As shown later, this is expected to be the case if the counter-rotational flows possess a single sign of rotation above the z-plane (and the opposite sign below it). With the localisation imposed on $1/\sigma$ the results presented here are qualitatively the same as in a model in which the return current is very diffuse.
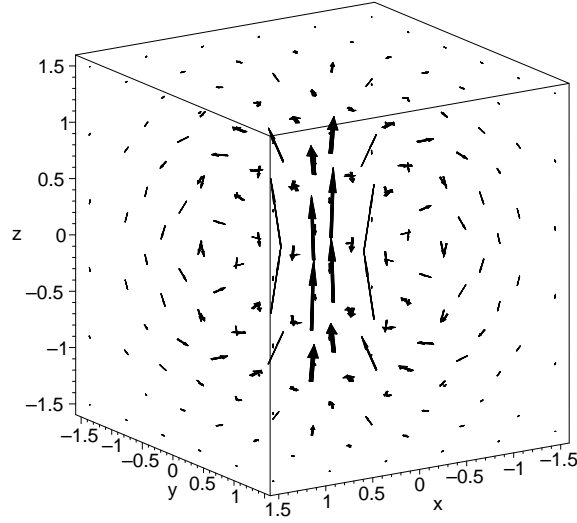
Figure 4.6: Vector-field illustration of the localised axisymmetric current (parameters $k = 1$, $a = 1$, $L = 1$, $b_0 = 1$, $\mu = 1$).

Combining (4.8) and (4.9) and taking $\mathbf{E} = -\boldsymbol{\nabla}\phi$ gives

$$-\boldsymbol{\nabla}\phi + \mathbf{v} \times \mathbf{B} = \frac{1}{\sigma}\mathbf{j}. \tag{4.13}$$

The non-ideal term $\eta\mathbf{j}$ is now known, and we are left to deduce ϕ and $\mathbf{v}$. The component of (4.13) parallel to the magnetic field is given by

$$-\boldsymbol{\nabla}\phi \cdot \mathbf{B} = \frac{1}{\sigma}\mathbf{j} \cdot \mathbf{B}$$

and so an expression for ϕ can be found by integrating along the magnetic field lines, expressions for which are given by (4.10). Starting the integration from the initial condition $\phi = \phi_0\left(r_0, \theta_0\right)$ at $z = 0$ we deduce that

$$\phi\left(r_0, \theta_0, s\right) = -\int_0^s \frac{1}{\sigma}\mathbf{j} \cdot \mathbf{B} \, ds + \phi_0\left(r_0, \theta_0\right). \tag{4.14}$$

An equivalent expression for ϕ in terms of (r, θ, z) can then be obtained using the inverse field line mappings given by (4.11).

The initial integration condition $\phi_0\left(r_0, \theta_0\right)$ is a free function that will affect the plasma velocity $\mathbf{v}$, and so, for a solution confined to a finite region, it represents a boundary condition on the solution. We choose here to set $\phi_0\left(r_0, \theta_0\right) \equiv 0$ since this is the condition needed for a purely counter-rotational plasma velocity that is anti-symmetric about $z = 0$. The corresponding potential, ϕ, is given as a function of r and z by

$$\phi = -\frac{\sqrt{2\pi}\, b_0 k L}{\sigma_0 \mu a^3}\left(a^2 - r^2\right) e^{-5r^2/a^2}\mathrm{erf}\left(\frac{\sqrt{2}z}{L}\right), \tag{4.15}$$

where $\mathrm{erf}\left(\xi\right)$ is the error function defined by

$$\mathrm{erf}\left(\xi\right) = \frac{2}{\sqrt{\pi}}\int_0^\xi e^{-u^2}\,\mathrm{d}u.$$
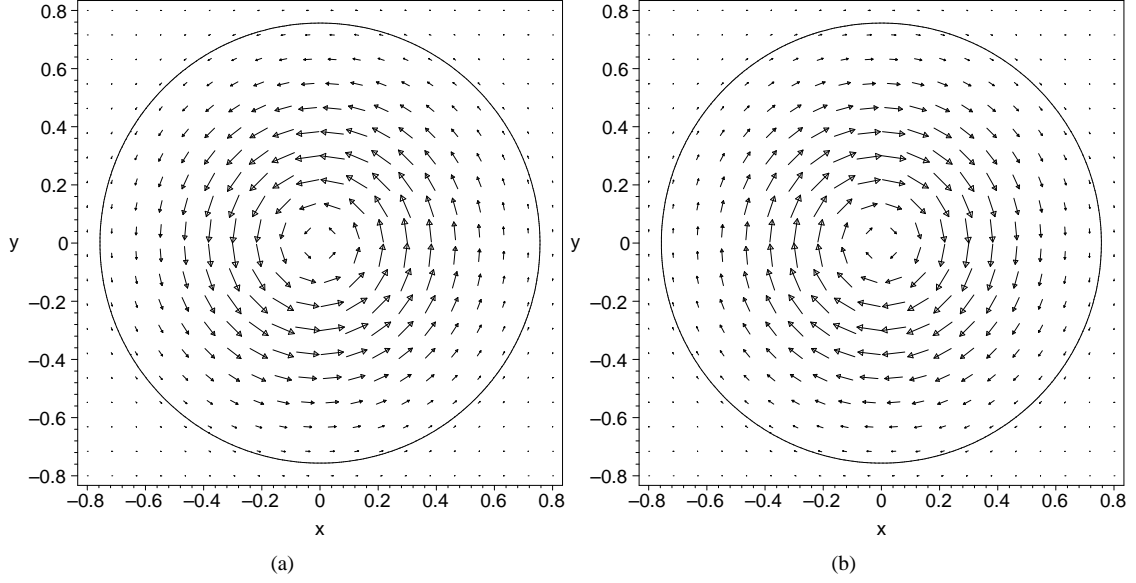
Figure 4.7: Counter-rotating flows (a) above ($z = 1$) and (b) below ($z = -1$) the central plane, $z = 0$. The solid line indicates the boundary 2% of the non-ideal region in the same planes (parameters $k = 1$, $a = 1$, $L = 3$, $b_0 = 1$, $\mu = 1$, $\eta_0 = 1$).

Thus, a jump in the electric potential across the non-ideal region exists, with the maximum potential difference being along the central field line. Outwith the non-ideal region the electric field is in the radial direction only, oppositely directed above and below central plane ($z = 0$), and confined within the flux tube consisting of field lines which thread the non-ideal region.

The component of the velocity perpendicular to the magnetic field can be deduced from (4.13) as

$$\mathbf{v}_\perp = \frac{(-\boldsymbol{\nabla}\phi - \mathbf{j}/\sigma) \times \mathbf{B}}{|B|^2}.$$

We use the freedom to add a component parallel to $\mathbf{B}$ to ensure $\nabla \cdot \mathbf{v} = 0$:

$$\mathbf{v} = \mathbf{v}_\perp - (\mathbf{v}_\perp)_z \frac{\mathbf{B}}{b_0}.$$

The resultant velocity field is in the azimuthal direction only and given by

$$\mathbf{v} = \frac{2\eta_0 kr}{a} e^{-5r^2/a^2} \left(\frac{\sqrt{2\pi}\,L}{a^4} \left(6a^2 - 5r^2\right) \mathrm{erf}\left(\frac{\sqrt{2}z}{L}\right) + \frac{2z}{L^2} e^{-2z^2/L^2} \right) \hat{\boldsymbol{\theta}},$$

where $\eta_0 = 1/\sigma_0\mu$. An example is illustrated in Figure 4.7. The flow is counter-rotational, i.e. rotates in opposite sense above and below the $z = 0$ plane (where it vanishes). The magnitude of the flow increases with distance from the central plane and becomes independent of height, z, in the ideal region. Non-zero flow is confined to the flux tube consisting of the field lines threading the non-ideal region.

How does this velocity compare with the order of magnitude estimate given by (4.5) in the previous section? Above and below the non-ideal region we may obtain an estimate of the typical plasma velocity

(which, in these regions, is independent of height) by finding the maximum value of $\mathbf{v}$ along a radial line. This maximum velocity turns out to be given by

$$v_{max} = \kappa \frac{\eta_0 k L}{a^2},\tag{4.16}$$

where κ is the constant given by

$$\kappa = \left(\frac{9 + \sqrt{177}}{20} \right) \sqrt{2\pi \left(75 - 5\sqrt{177} \right)} \exp\left(\frac{\sqrt{177}}{4} - \frac{15}{4} \right) \approx 5.327.\tag{4.17}$$

The expression (4.16) is in qualitative agreement with the order of magnitude estimate given by (4.5). We have, therefore, confirmed the intuitive estimate with the analytical model.

The motivation for our choice of η is now apparent. Since the component of the current parallel to the magnetic field is given by

$$j_\parallel = \frac{4 b_0 k}{\mu a^3} \left(a^2 - r^2 \right) \exp\left(-\frac{r^2}{a^2} - \frac{z^2}{L^2} \right),$$

there is a change in the sign of $j_\parallel$ at $r = a$. A uniform resistivity would then lead to flows in each $r = const.$ plane rotating in different senses for $r < a$ and for $r > a$. Although the magnitude of the rotational flow for $r > a$ would be small, we choose to set it to zero for simplicity, by imposing a profile for η that ensures the non-ideal region is contained within the surface $r = a$. We have therefore obtained a kinematic model for the qualitative description of flux-tube disconnection outlined in Section 4.2.

In this reconnection process all the field lines which thread through the non-ideal region are continually changing their connections, with each field line reconnecting to others within the same surface $r = r_0$. This is one of the features that distinguishes the 3D case from the 2D case where field lines are cut and reconnected at a single point, and therefore the reconnection rate has a different interpretation in 3D. The field line which has the maximum difference in potential above and below the non-ideal region is identified as the reconnection line. In the present model, for symmetry reasons, the reconnection line is the z-axis. The reconnection rate is given by

$$\frac{\mathrm{d}\Phi_{rec}}{\mathrm{d}t} = \int \mathbf{E}_\parallel \, dl = \int \mathbf{E} \cdot \mathbf{B} \, ds = \int_{-\infty}^{\infty} \frac{4\eta_0 b_0 k}{a} e^{-2z^2/L^2} dz = \frac{2\sqrt{2\pi}\eta_0 b_0 k L}{a},$$

or, after substituting for v_{max} from equation (4.16),

$$\frac{d\Phi}{dt} = \frac{\sqrt{2\pi}}{\kappa} \, 2 b_0 a v_{max}$$

where κ is the constant given by equation (4.17). Thus the reconnection rate in the kinematic model is, up to a constant factor, in agreement with the earlier qualitative estimate (4.6).

Previous analytical 3D reconnection models (see, for example, Hornig and Priest, 2003) have taken a uniform current and localised the non-ideal region through localisation of the resistivity η alone. Such models find that the reconnection rate is independent of the parameter controlling the radius of the non-ideal region. Here we find that with a localised current this parameter, a, does become important in determining

the reconnection rate.

4.4   Possible Implications of the Momentum Equation

Both the order of magnitude estimate (discussed in Section 4.2) and the analytical model (discussed in Section 4.3) for flux-tube disconnection are kinematic analyses, i.e. they neglect the implications of the momentum equation. We now consider, from a qualitative perspective, the extent to which the momentum equation may alter the solutions. It was shown in Sections 4.2 and 4.3 that there is some freedom present in the solutions presented. Specifically, the flux-tube may respond to an increase (decrease) in the magnitude of the rotational driving velocity v_0 either by an increase (decrease) in the length, l, of the non-ideal region, or by an increase (decrease) in the number of turns present within the flux tube or by a combination of both effects. We wish to examine whether this freedom is inherent to the 3D process, or whether it arises through neglect of the momentum equation.

Assume, then, that the qualitative model presented in Section 4.2 also satisfies the momentum equation,

$$\rho \left(\mathbf{v} \cdot \boldsymbol{\nabla} \right) \mathbf{v} = -\boldsymbol{\nabla} p + \mathbf{j} \times \mathbf{B}.$$

Consider the plasma pressure along a field-line bounding the flux tube. In the central plane ($z = 0$) the plasma velocity ($\mathbf{v}$) vanishes and so we may estimate the pressure at the edge of the tube as

$$\left(-\boldsymbol{\nabla} p \right)_{centre} + \mathbf{j} \times \mathbf{B} = \mathbf{0}$$

$$\Rightarrow | - \boldsymbol{\nabla} p|_{centre} = j_z B_\theta = \frac{2k^2 b_0^2}{\mu a}. \tag{4.18}$$

In a plane of constant z above the non-ideal region the Lorentz force vanishes and

$$\left(-\boldsymbol{\nabla} p \right)_{top} = \rho \left(\mathbf{v} \cdot \boldsymbol{\nabla} \right) \mathbf{v}$$

$$\Rightarrow | - \boldsymbol{\nabla} p|_{top} = \frac{\rho v_0^2}{a}. \tag{4.19}$$

Now, since the pressure must be constant along a boundary field line, the estimates for $| - \boldsymbol{\nabla} p|_{centre}$ and $| - \boldsymbol{\nabla} p|_{top}$ given by (4.18) and (4.19), respectively, must be equal, i.e. we have that

$$v_0 = \sqrt{\frac{2}{\mu \rho}} k b_0, \tag{4.20}$$

or, rewriting in terms of the azimuthal Alfvén velocity, $v_{A\theta} = k b_0 / \sqrt{2\mu\rho}$,

$$v_0 = 2 v_{A\theta}.$$

We may now return to the estimate for the plasma velocity v_0, given by equation (4.5), obtained in the

qualitative analysis of section 3, i.e.

$$v_0 = \frac{2\eta k L}{a^2}.$$

Equating this last expression for v_0 with that given by (4.20) determines the parameter L, which determines the length of the non-ideal region, in terms of the axial field strength and flux-tube radius as

$$L = \sqrt{\frac{1}{2\rho\mu}} \frac{b_0 a^2}{\eta}. \tag{4.21}$$

These estimates suggest that a change in the rotational driving velocity (v_0) results in a change in the azimuthal magnetic field. The length (L) of the non-ideal region is determined by the axial field strength and tube radius. The expression for L given by (4.21) also allows us to estimate the ratio, L/a, between the length and diameter of the non-ideal region,

$$\frac{L}{a} = \frac{a}{\eta} v_A = R_m,$$

where v_A is the Alfvén velocity, $v_A = b_0/\sqrt{2\mu\rho}$ and $R_m = v_A a/\eta$ is the magnetic Reynolds number based on the width of the flux tube. Thus the inclusion of the momentum equation in the qualitative analysis suggests that the length of the non-ideal region is very much greater than its width, resulting in a long thin current sheet.

4.5   Summary

In this chapter we have presented a stationary model for flux-tube disconnection. The model considers a straight magnetic flux tube which has a localised twist present in its central region as a result of a counter-rotational driving velocity imposed at the footpoints of the magnetic flux tube. The model has a non-ideal region which is localised in all three dimensions, and an electric field component parallel to the magnetic field is present within the non-ideal region. These two properties are those required for the process to be considered as an example of global general magnetic reconnection (Schindler et al., 1988). It differs in many respects from more traditional models of 2D and 3D reconnection; the magnetic field is not of X-type structure, and the field lines are continually cut throughout the diffusion region.

An order of magnitude analysis, presented in Section 4.2, allows us to understand, from a qualitative point of view, how the disconnection occurs. An increase in the rotational driving velocity of the footpoints results in an increase in the number of turns present within the twisted flux tube. The number of turns may be altered by increasing the strength of the poloidal field component, increasing the length of the non-ideal region, or by a combination of both effects. A similar qualitative estimate of the reconnection rate has also been made, which was shown to be proportional to the rotational driving velocity and to the magnetic flux of the tube, i.e. the product of the magnetic field strength and the radius of the flux tube.

In Section 4.3 we presented an analytical incompressible model of flux-tube disconnection. Just as with several such 3D reconnection models, the analysis is kinematic, in that the effects of the equation of motion have been ignored. Instead, the implications of Ohm's law and Faraday's law have been considered. The

analytical solutions confirm the estimates of the flux tube geometry and strength and reconnection rate in relation to the footpoint velocity. A qualitative estimate from the equation of motion in Section 4.4 implied that the ratio (L/a) of the diffusion region length to width is of order the magnetic Reynolds number. In turn this implies that normally the reconnection is slow and can only be fast when $L/H \approx R_m$.

Chapter 5

An MHD Experiment into the Effect of Spinning Boundary Motions on Misaligned Flux-tubes

In this chapter we describe a numerical experiment in which the nature of a 3D reconnection event is investigated. The experiment follows a different approach from the work described in Chapters 3 and 4 in that the non-ideal region is not localised in space in all three-dimensions and, as we will show, reconnection at a *quasi-separator* reconnection plays the important role in the process. We begin therefore in Section 5.1 by providing some additional theory behind and motivation for the experiment.

The results of this chapter can be found in Wilmot-Smith and De Moortel (2007).

5.1 Introduction

As mentioned in Chapter 2, separator reconnection (Priest and Titov, 1996) is thought to play a fundamental role in coronal heating, with observations directly suggesting separator reconnection is occurring in the corona (Longcope et al., 2005). The coronal magnetic field is anchored in the photosphere where surface motions act to displace the flux tubes, providing a Poynting flux through the base of the corona. The extremely high magnetic Reynolds numbers of the corona require very large gradients in the magnetic field to be built up before non-ideal processes can become important in localised regions and allow for energy release. Models for coronal heating therefore rely on the large-scale motions producing small-scale structure (Sweet, 1958, Parker, 1957). This may occur through the action of complex photospheric flow acting on simple coronal fields (Parker, 1972, van Ballegooijen, 1986, Galsgaard and Nordlund, 1996) or through the action of simple photospheric flows on complex coronal fields, as in the *coronal tectonics model* of Priest et al. (2002). The model describes each coronal loop as being anchored to the photosphere in

many discrete sources. Thus each loop consists of magnetic flux divided by separatrix surfaces into several distinct domains. Even simple motions of the flux sources act to form current sheets along the separatrices of the field. Reconnection then allows for dissipation of the current sheets and thereby a heating of the corona. In the 'minimum current corona' (MCC) model of Longcope (1996), flux tubes are represented by point magnetic charges in a manner that allows the pattern of flux-tube linkage to be analysed. It is shown that in the absence of reconnection, current ribbons form along magnetic separators. The MCC model finds an approximation to the current that forms along a separator in response to displacement of photospheric footpoints. When the stress along a separator (that results from the accumulated current) becomes too large, reconnection allows for the flux between domains to be changed and energy stored in the separator current released. The underlying assumption of models such as these is that the coronal field is able to evolve through a series of flux-constrained equilibria (Priest and Raadu, 1975, Titov, 1992).

There are now several numerical experiments that investigate separator reconnection in some detail, with particular emphasis placed on elementary heating events. Here, the effect of simple footpoint motions on current sheet formation and reconnection is considered. The relative motion of two magnetic sources which are not initially connected, but have an overlying background magnetic field, has been extensively numerically modelled (Galsgaard et al., 2000, Parnell and Galsgaard, 2004, Galsgaard and Parnell, 2005, Haynes et al., 2007). The flux sources interact through separator reconnection and a complex magnetic topology is observed.

Here we present 3D numerical simulations of an elementary heating event, which build on the papers of De Moortel and Galsgaard (2006a,b). In that series of papers the authors consider the interaction of two magnetic flux tubes as they are subjected to two distinct types of motion imposed on the boundary footpoints. The first is a large-scale rotating motion in which both of the footpoints on each of the boundaries are rotated and the second is a small-scale spinning motion in which each footpoint is spun while its position remains fixed. The magnetic flux tubes in the spinning case of De Moortel and Galsgaard (2006b) are initially perfectly aligned and hence remain so throughout the experiment. The experimental setup taken is therefore non-generic, representing a situation extremely unlikely to arise in the solar context. In the initial potential field extrapolation of perfectly aligned flux sources there are two flux-domains with a single boundary between them, while in any other situation where the flux tubes are not perfectly aligned there are four flux-domains and correspondingly four boundaries between domains. It is not clear whether in the misaligned case, with its additional boundaries and likely sites for current-sheet formation, the nature of the reconnection taking place will be the same as in the perfectly aligned case. In particular, the rate of reconnection could be quite different, with corresponding implications for coronal heating.

In this chapter we examine the relevant case for the solar corona where the magnetic flux tubes are misaligned, imposing the same spinning motions on the tube footpoints as De Moortel and Galsgaard (2006b). One aim of the chapter is to examine the nature of the 3D reconnection process that takes place (Section 5.3). Then in Section 5.4 we use some comparisons between data of one of the cases of De Moortel and Galsgaard (2006b) and our results to see how the nature of the reconnection differs for the two examples. We summarise our results in Section 5.5 but begin in the next section by briefly describing the numerical code and experimental setup.

5.2   Model Setup

We use a parallel numerical code to solve the dimensionless MHD equations in the form

$$
\begin{aligned}
\frac{\partial \mathbf{B}}{\partial t} &= -\nabla \times \mathbf{E}\,, \\
\mathbf{E} &= -\left(\mathbf{v} \times \mathbf{B}\right) + \eta \mathbf{j}\,, \\
\mathbf{j} &= \nabla \times \mathbf{B}\,, \\
\frac{\partial \rho}{\partial t} &= -\nabla \cdot \left(\rho \mathbf{v}\right)\,, \\
\frac{\partial}{\partial t}\left(\rho \mathbf{v}\right) &= -\nabla \cdot \left(\rho \mathbf{v}\mathbf{v} + \underline{\underline{\tau}}\right) - \nabla P + \mathbf{j} \times \mathbf{B}\,, \\
\frac{\partial e}{\partial t} &= -\nabla \cdot \left(e \mathbf{v}\right) - P\nabla \cdot \mathbf{v} + Q_{visc} + Q_{Joule}\,,
\end{aligned}
$$

where $\mathbf{B}$ is the magnetic field, $\mathbf{v}$ the plasma velocity, $\mathbf{E}$ the electric field, $\mathbf{j}$ the electric current, η the resistivity, $\underline{\underline{\tau}}$ the viscous stress tensor, ρ the density, P the pressure, e the internal energy, Q_{visc} the viscous dissipation and Q_{Joule} the Joule dissipation. In addition the ideal gas law is assumed, so that $P = \left(\gamma - 1\right)e = 2e/3$. The MHD equations have been non-dimensionalised. Dimensional quantities may be obtained if characteristic values of three quantities are chosen and the remainder obtained using the relations

$$
\begin{aligned}
v_0 &= \frac{l_0}{t_0}\,, \\
e_0 &= \rho_0 v_0^2\,, \\
B_0 &= v_0 \sqrt{\left(\mu_0 \rho_0\right)}\,, \\
T_0 &= \frac{\tilde{\mu} v_0^2}{R}\,, \\
E_0 &= v_0 B_0\,, \\
j_0 &= \frac{B_0}{\mu_0 l_0}\,,
\end{aligned}
$$

where the magnetic permeability, $\mu_0 = 4\pi \times 10^{-7}\mathrm{Hm}^{-1}$, $\tilde{\mu} = 0.6$ and the gas constant, $R = 8.3 \times 10^3 \mathrm{m}^2\mathrm{s}^{-2}\mathrm{K}^{-1}$. This is because in the non-dimensionalisation μ_0 has been set as $\mu_0 = 1$ and R to be equal to the mean molecular weight.

For a comprehensive description of the numerical code see Nordlund and Galsgaard (1997). Here we summarize some of its main features. A staggered mesh is used on which the variables are evaluated. The variables $\mathbf{E}$ and $\mathbf{j}$ are calculated at the centre of each edge of a unit cube while $\mathbf{B}$ and $\rho\mathbf{v}$ are calculated at the centre of each face and ρ and e at the body centre of the cube. To evaluate spatial derivatives a sixth-order finite difference scheme is employed; six operators are required $(\partial^{+}_{,[xyz]})$ that return the derivative of the variable at $\pm 1/2$ a gridpoint (in the appropriate direction). For example $\partial^{+}_{,x}$ is given by

$$
\begin{aligned}
\partial^{+}_{,x}\left(f_{i,j,k}\right) &= f'_{i+1/2,j,k} \\
&= \frac{a}{\Delta x}\left(f_{i,j,k} - f_{i+1,j,k}\right) + \frac{b}{\Delta x}\left(f_{i-1,j,k} - f_{i+2,j,k}\right) + \frac{c}{\Delta x}\left(f_{i-2,j,k} - f_{i+3,j,k}\right)
\end{aligned}
$$

where $a = 1 - 3b + 5c$, $b = -1/24 - 5c$ and $c = 3/640$, and others obtained by permutation of the indices. Since the result obtained is returned $\pm 1/2$ a gridpoint from the input values it may be that no subsequent spatial interpretation is necessary to find the value at the required location. If such an interpolation is necessary however then a fifth-order method is used, the further six numerical operators being $T^{\pm}_{[xyz]}$, say, where

$$T^{+}_{x}\left(f_{i,j,k}\right) \quad = \quad f_{i+1/2,j,k} \tag{5.1}$$
$$= \quad a\left(f_{i,j,k} + f_{i+1,j,k}\right) + b\left(f_{i-1,j,k} + f_{i+2,j,k}\right) + c\left(f_{i-2,j,k} + f_{i+3,j,k}\right) \tag{5.2}$$

where now $a = 1/2 - b - c$, $b = -1/16 - 3c$ and $c = 3/256$. To advance the solutions in time a third-order predictor-corrector method is used. The predictor is given by

$$f^{(*)}_{n+1} = a_1 f_{n-1} + \left(1 - a_1\right) f_n + b_1 \dot{f}_n,$$

and the corrector by

$$f_{n+1} = a_2 f_{n-1} + \left(1 - a_2\right) f_n + b_2 \dot{f}_n + c_2 \dot{f}^{(*)}_{n+1}.$$

In the above,

$$\begin{aligned}
a_1 &= r^2, \\
b_1 &= \Delta t_{n+1/2}\left(1 + r\right), \\
a_2 &= 2\left(1 + r\right)/\left(2 + 3r\right), \\
b_2 &= \Delta t_{n+1/2}\left(1 + r^2\right)/\left(2 + 3r\right), \\
c_2 &= \Delta t_{n+1/2}\left(1 + r\right)/\left(2 + 3r\right), \\
r &= \Delta t_{n+1/2}/\Delta t_{n-1/2},
\end{aligned}$$

where $\Delta t_{n+1/2} = t_{n+1} - t_n$ and $\Delta t_{n-1/2} = t_n - t_{n-1}$. In addition, the code uses artificial fourth-order viscosity and magnetic resistivity ('hyper-resistivity' and 'hyper-viscosity') terms to try and limit diffusion to short length-scales but still handle the development of numerical instabilties.

In the experiment described here we place two positive sources (which we label A and B for convenience) on the lower boundary of the domain, aligned with the x-axis, and two negative sources (labelled a and b) on the upper boundary, aligned with the y-axis:

$$B_z\left(x, y, z = 0\right) \quad = \quad e^{-r_1^2/r_0^2} + e^{-r_2^2/r_0^2}, \tag{5.3}$$
$$B_z\left(x, y, z = 1\right) \quad = \quad e^{-r_3^2/r_0^2} + e^{-r_4^2/r_0^2}, \tag{5.4}$$

where $r_0 = 0.065$, $r_1^2 = \left(x - 0.3\right)^2 + \left(y - 0.5\right)^2$, $r_2^2 = \left(x - 0.7\right)^2 + \left(y - 0.5\right)^2$, $r_3^2 = \left(x - 0.5\right)^2 + \left(y - 0.3\right)^2$, and $r_4^2 = \left(x - 0.5\right)^2 + \left(y - 0.7\right)^2$. In addition, on both the upper and lower boundaries we take $B_x = B_y = 0$. These sources are shown in Figure 5.1.

The above are initial conditions on the magnetic field and throughout the experiment each of the four flux sources is spun, those on the lower boundary in a counter-clockwise direction and those on the upper

(a)

(b)

(c)
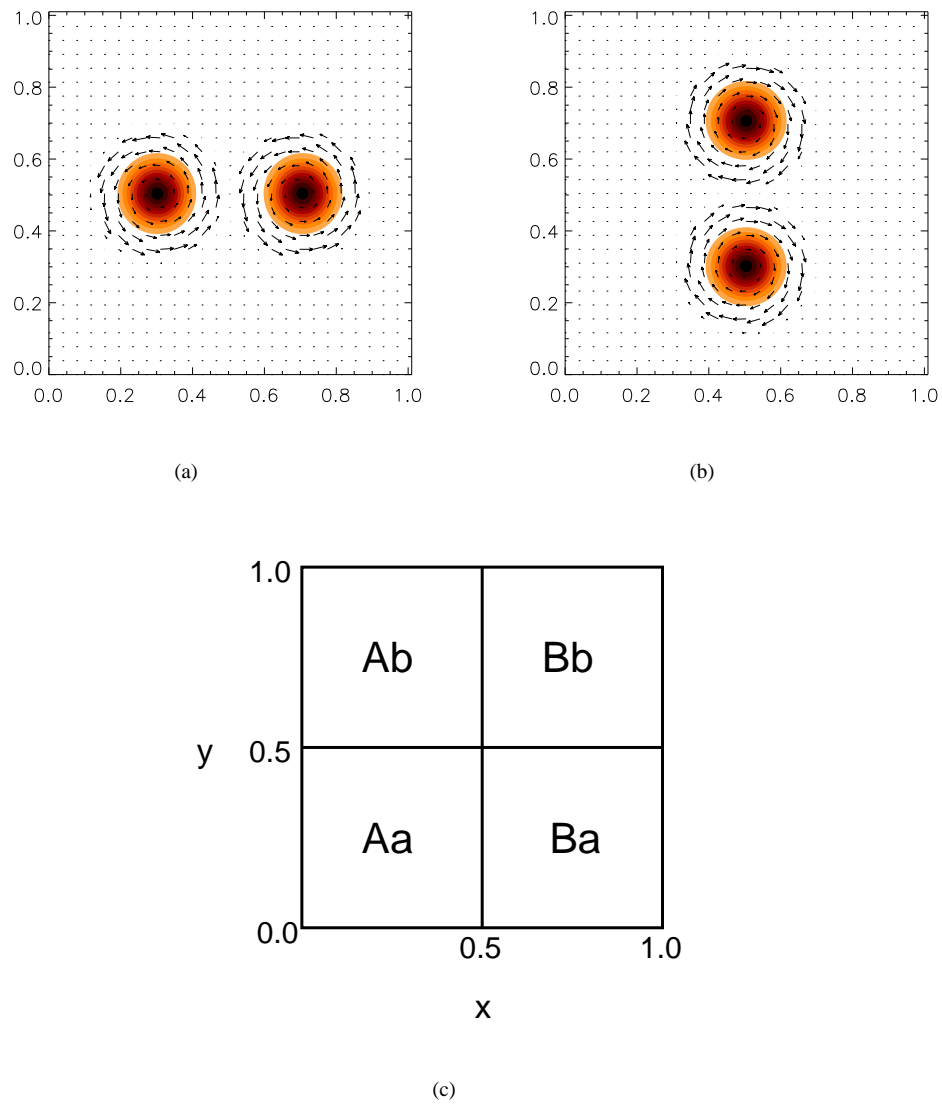
Figure 5.1: Contours plot illustrating $|\mathbf{B}|$ on (a) the lower and (b) the upper boundaries of the domain. Superimposed are vectors of the imposed spinning driving velocity in the same planes. The flux sources are labelled A (left-most source) and B (right-most source) on the lower boundary and a (lower source) and b (upper source) on the upper boundary. As seen in (c) there are initially four regions of differing magnetic flux connectivity in the domain, with flux connecting sources A and a labelled Aa, and similarly for Ab, Ba and Bb.

boundary in a clockwise direction:

$$v_\theta\left(r, z = 0\right) = v_0 r_1 [1 + \tanh\left(p\left(1 - qr_1\right)\right)] + v_0 r_2 [1 + \tanh\left(p\left(1 - qr_2\right)\right)], \tag{5.5}$$

$$v_\theta\left(r, z = 1\right) = -v_0 r_3 [1 + \tanh\left(p\left(1 - qr_3\right)\right)] - v_0 r_4 [1 + \tanh\left(p\left(1 - qr_4\right)\right)], \tag{5.6}$$

where $v_0 = 0.02222$, $p = 16.8$ and $q = 5.6$. This velocity has been chosen such that the shape of the flux sources on the boundaries is maintained as they are spun, so that the source profile given by equations (5.1) and (5.2) holds throughout the experiment. In the descriptions of the experimental results we refer to the *spin angle*; this measures the angle in radians by which the sources have been spun from their initial positions. Note that the chosen driving velocity is very slow compared with the typical Alfvén velocity.

Using these initial conditions on the magnetic field at the boundaries of the domain, a potential field is calculated to fill the domain and imposed as an initial condition. The misalignment of the four sources results in the region being divided into four distinct flux domains, as shown for the central plane ($z = 0.5$) in Figure 5.1(c). The magnetic flux strength decreases rapidly away from the centres of the sources but there are nevertheless no real magnetic null-points within the domain so that there exist only *quasi*-separators and *quasi*-separatrices.

The dynamical evolution of the system is obtained by using the numerical code described to solve the non-ideal MHD equations, in a 128^3 Cartesian box. Periodic boundary conditions are imposed on the sides of the box. The resultant evolution of the system is described in the following sections.

5.3 Experimental results

In this chapter we choose to focus on the basic dynamical evolution of the system, placing particular emphasis on the reconnection mechanism that takes place. Therefore we consider first, in Section 5.3.1, the character of the magnetic flux connectivity and how it develops with spin angle. We proceed in section 5.3.2 to describe the nature and evolution of the current concentrations before considering the plasma velocities and implications for the reconnection mechanism in Section 5.3.3.

5.3.1 Magnetic Flux Connectivities

We start by examining the behaviour of the magnetic flux with spin angle. With the positions of the magnetic source centres on the lower and upper boundaries fixed, the effect of the spinning foot-point motions is to drive the magnetic field away from potential and may therefore result in magnetic reconnection between the sources.

Figure 5.2 gives a simple, qualitative overview of how the magnetic flux in the domain evolves as the sources on the boundary are spun. Some illustrative field lines have been traced from the two sources on the lower boundary, coloured red if they are associated with source A and green for source B. In the initial potential field, shown in Figure 5.2 (a), flux from each of the lower sources is divided equally between the
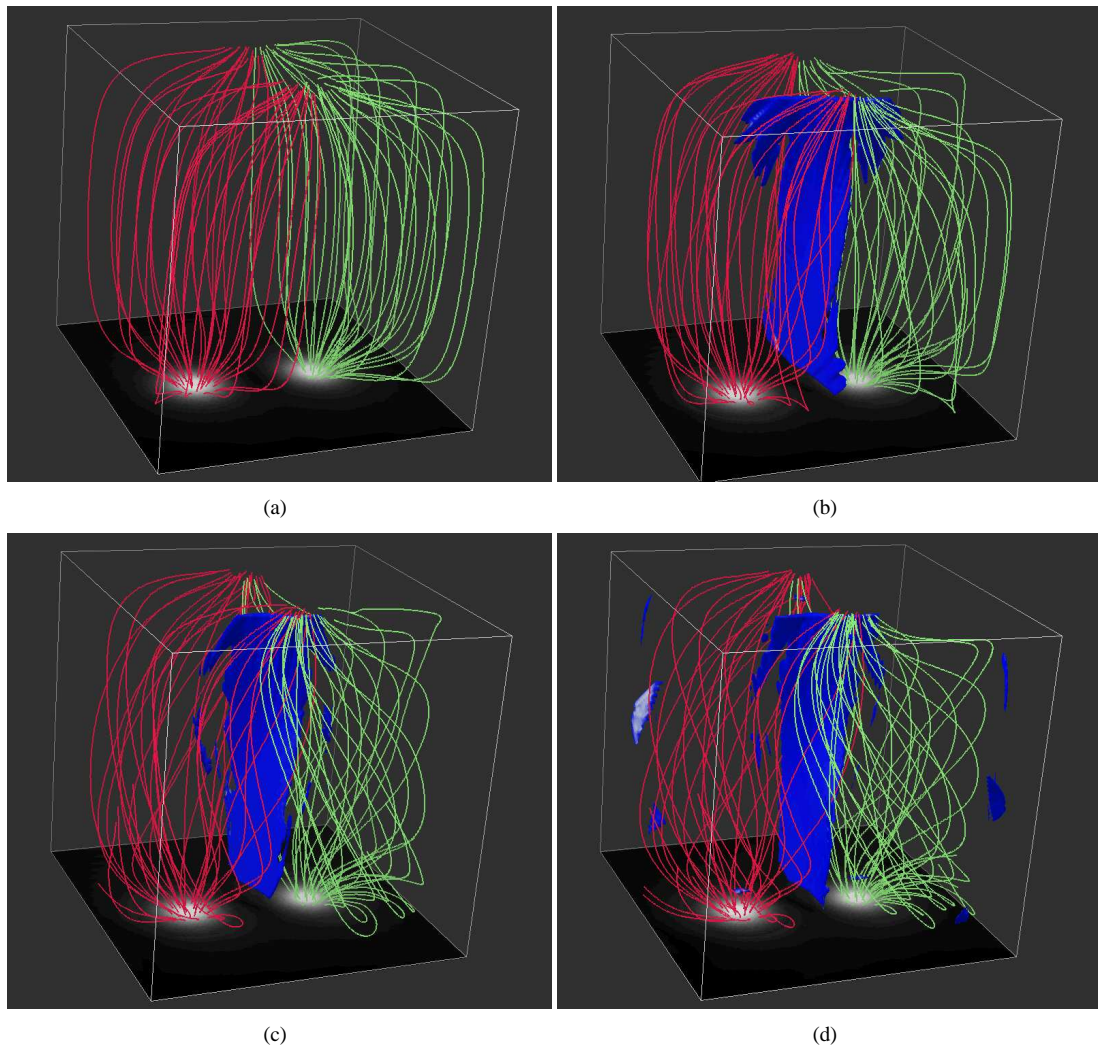
Figure 5.2: Selected field lines traced from the two sources on the lower boundary, at spin angles (a) $\theta = 0$ (b) $\theta = 0.79$ (c) $\theta = 1.87$ and (d) $\theta = 2.64$. Those traced from source A are coloured red and those from source B coloured green. The field lines are seen to become increasingly twisted with spin angle and, in addition, it is seen that the initially equal distribution of flux from a single source on the lower boundary between both sources on the upper boundary becomes unequal with increasing spin-angle. Over-plotted are isosurfaces of current; a twisted current sheet is seen to form in the centre of the domain.
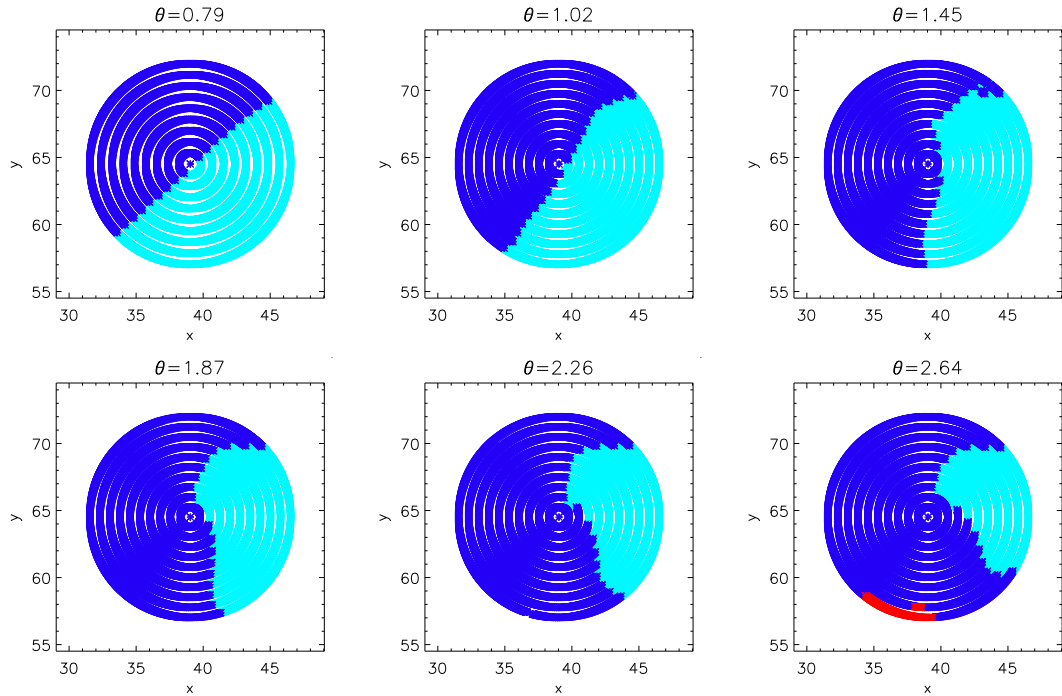
Figure 5.3: Connectivity of a source, A, say, on the lower boundary with spin angle. Flux with connectivity Aa is shown in light blue, flux with connectivity Ab is shown in dark blue and flux which leaves the box in red.

two upper sources. As the sources are spun the magnetic flux in the domain becomes increasingly twisted, as seen in the sequence of images 5.2 (b-d). In addition, the magnetic flux connectivities of the sources change with increasing spin angle; by the end of the experiment, flux from source A (B) is predominately connected to source b (a). This property is reflected in the traced field lines of 5.2 (d). Superimposed on the same diagrams are (the same) isosurfaces of (strong) current. Note that, for clarity, current in the three grid cells closest to each of the boundaries has been removed from the diagrams. Early in the experiment, a twisted current sheet is seen to form in the centre of the domain, extending vertically throughout the box, and this current sheet persists throughout the simulation. We will return to examine the twisted current sheet, but now proceed to examine the evolution of the magnetic flux connectivity in more detail.

We begin by considering the evolution of connectivity of the magnetic sources themselves. It is important to note that the sources are non-ideal and we are, therefore, unable to follow the evolution in time of individual field lines exactly at these locations. Instead, for each spin-angle we trace a large number of field lines from the sources on the lower boundary. For each such field line we deduce its magnetic connection on the upper boundary and the amount of magnetic flux associated with it. In Figure 5.3, field lines have been traced from source A to the upper boundary and coloured dark blue if they are connected to source b (i.e. if their magnetic connectivity is of type Ab), light blue if they are connected to source a (i.e. if their magnetic connectivity is of type Aa) and red if they leave the box. As suggested already by the traced field lines of Figure 5.2, the total magnetic flux of type Aa is seen to decline with spin angle, whilst that of type Ab is seen to increase. The reconnection mechanism behind these transitions will be discussed later.
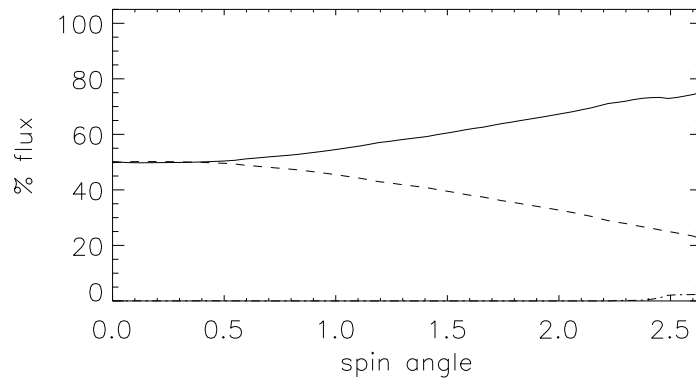
Figure 5.4: Change in magnetic flux connectivity with spin angle of source A (B) on the lower boundary. The solid line shows the percentage of flux with connection Ab (Ba), the dashed line the percentage of flux with connection Aa (Bb) and the dot-dashed line the percentage of flux from source A (B) that leaves the box.

We can use the information obtained in the field line tracing to deduce the percentage of flux from a source on the lower boundary connected to each of the two sources on the upper boundary. Figure 5.4 shows the change in these quantities with spin angle, together with the percentage of flux which leaves the box. We deduce that reconnection begins at spin angle $\theta \approx 0.5$ and the amount of flux with connectivity Aa (Ab) subsequently decreases (increases) linearly with spin angle until $\theta \approx 2.3$, close to the end of the experiment, when flux begins to leave the box. At the end of the experiment 22.3% of the flux from source A is connected to source a, so we can therefore deduce that at least 27.7% of the flux in the source has been reconnected by spin angle $\theta = 2.64$. There remains a possibility that a greater percentage of flux has reconnected if flux of type Ab reconnects at any stage in the experiment (with flux of type Ba) to form flux of type Aa. We later consider the likelihood of such events.

Given then that the magnetic flux connectivity inside the domain is changing as the spin-angle increases, we now examine how these changes become evident in the central plane, $z = 0.5$. We trace a large number of the field lines passing through the central plane, determine the connection of each field line on both the upper and the lower boundary, and assign the field line a colour according to its magnetic connectivity. Note that the tracing is now begun *at* the central plane rather than the source footpoints. By showing these colours in the central plane we generate a diagram in which the central plane is colour-coded according to the magnetic connectivity of the flux that pierces it. Figure 5.5 illustrates this connectivity for a sequence of increasing spin angles, with contours of electric current superimposed onto the same diagrams to enable us, at a later stage, to determine the role of the current in the flux evolution.

It can be seen from Figure 5.5 that even by spin-angle $\theta = 0.65$, before reconnection has had a significant effect on the initially equal distribution of flux types, the arrangement of flux in the central plane has been altered by the spinning motions. The four types of flux no longer meet at a point, but rather types Bb (red) and Aa (light blue) meet along a central line with types Ab (dark blue) and Ba (yellow) no longer coming into contact. A current structure has been seen to form between some, but not all, of the boundaries between the various flux domains. As the spin-angle increases, the area of the central plane pierced by flux
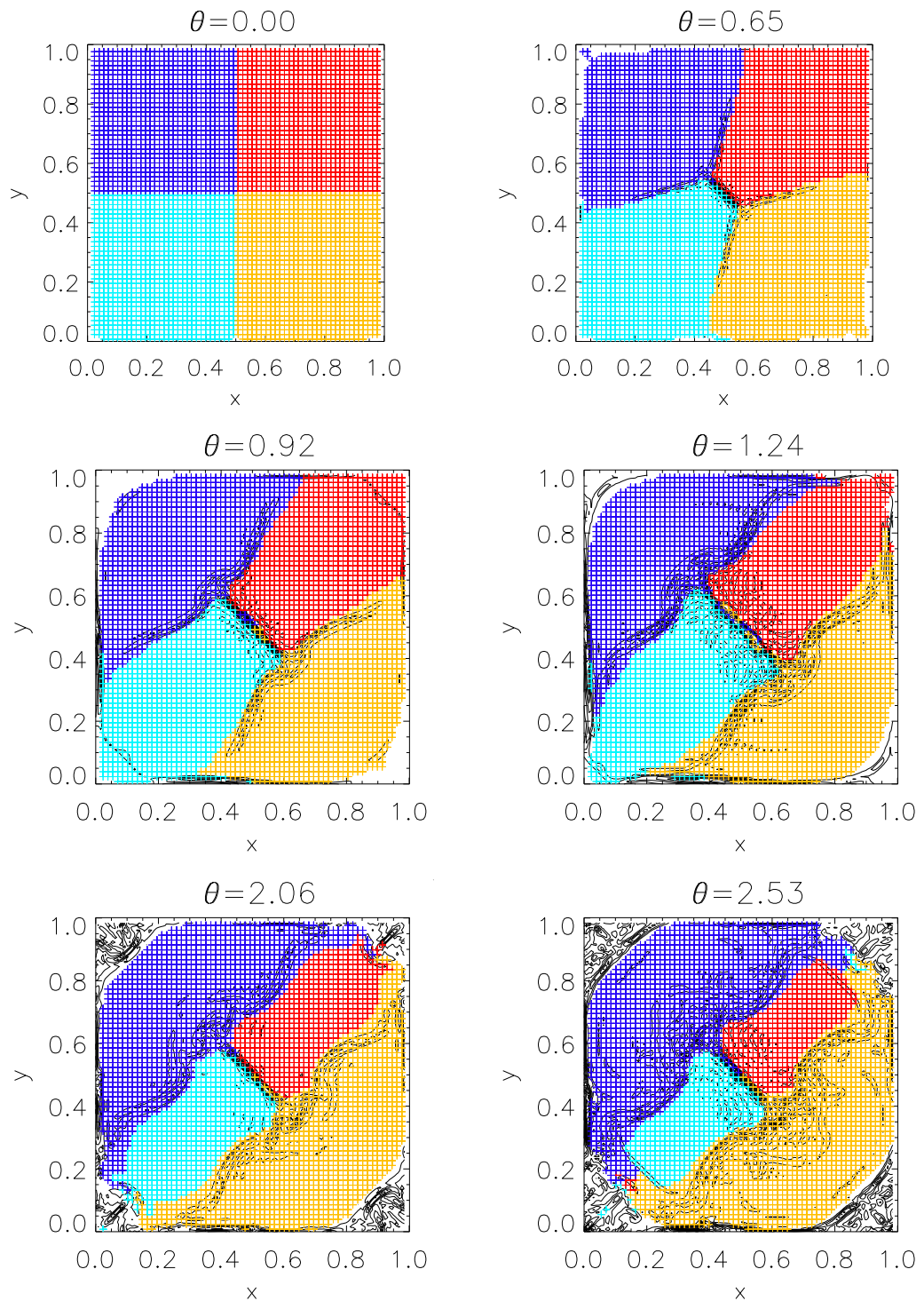
Figure 5.5: The figure shows a sequence of images at increasing spin-angles in which the magnetic flux passing through the central plane, $z = 0.5$, is coloured according to its magnetic connectivity. Flux with connectivity Aa is indicated in light blue, Ab in dark blue, Bb in red and Ba in yellow. Flux not associated with any of these connectivity types is not coloured. Over-plotted are contours of current density in the same plane.
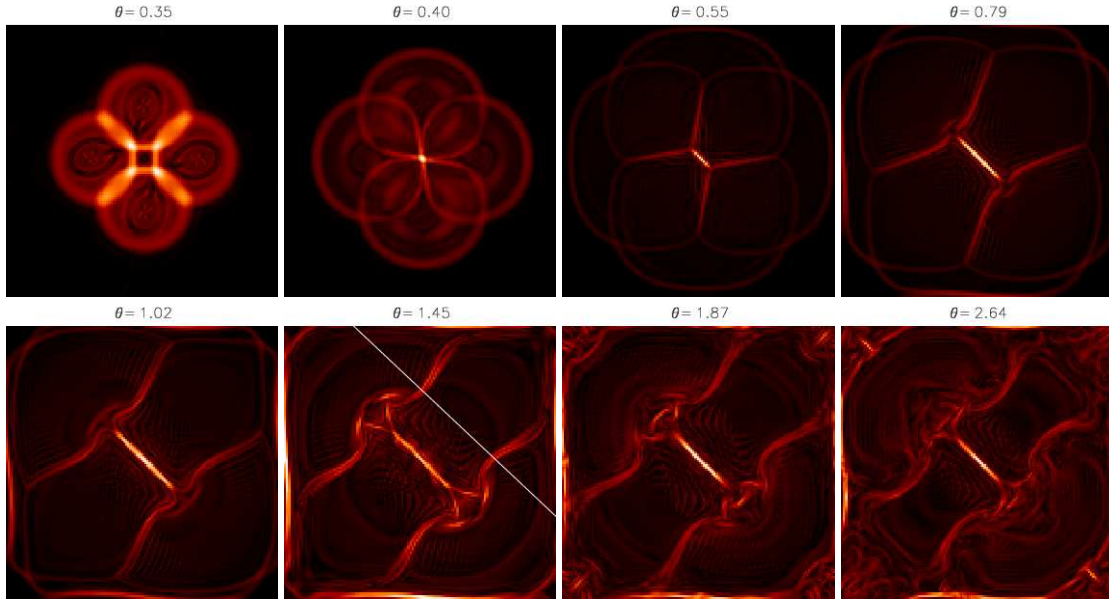
Figure 5.6: Sequence of images showing contours of current in the central plane $z = 0.5$ at increasing spin angles. Four wings of current are seen to extend from a strong current sheet in the centre of the domain. At later spin-angles Y-shaped cusps are seen to develop at the ends of the current sheet, seen here for example at $\theta = 1.45$. (The white line outlines a cross-section described later in the text.)

types Ab and Ba increases also. This is certainly not due in its entirety to compression or expansion effects of the flux tubes since we have already found the connectivities of the sources themselves to be changing as a result of magnetic reconnection. At later spin angles ($\theta \geq 1.70$) we observe that the flux types Aa and Bb are no longer in contact with the boundary, being entirely enclosed by the remaining flux types. We note that the strong central current sheet coincides exactly with the boundary between the flux types Aa and Bb but that the weaker 'wings' of current emanating from the central twisted sheet do not perfectly outline the remaining boundaries between the various flux types. We return to this point, together with a more detailed description of the current structure, later in this section.

Before doing so, we note that there are several reasons why some of the magnetic flux near the boundary of the $z = 0.5$ plane is not associated with any of the four flux types. The magnetic sources on the upper and lower boundaries decay exponentially with distance from the centre of the source and we have defined a particular (and, to a certain extent, artificial) radius at which we consider each source to end (namely $2r_0$). Thus, flux traced from the mid-plane falling outside this radius (on either the upper or the lower boundaries) is not considered to be associated with a particular flux source. In addition, toward the end of the simulation, a certain amount of magnetic flux from each of the four sources leaves the box and may do so after having passed through the central plane. These effects are not important in our consideration of the dynamical evolution of the system.

5.3.2   Current Evolution

The spinning motions imposed on the foot-points of the flux sources act to spin up the flux in each of the domains and so generate a shear at each of the interfaces between domains. We have already noted that, as seen in Figure 5.2, a strong current sheet, extending vertically throughout the box, forms early on in the experiment. Comparison with the current contours superimposed on the flux connectivity plots of Figure 5.5 confirms that this is a quasi-separator current sheet which has formed at the interface between the four flux domains. The sheet is twisted in the vertical direction as a result of the $\pi/2$ misalignment of the upper and lower sources. In addition, we can see from Figure 5.5 that four 'wings' of current emanate from the central current sheet and that these wings approximately outline the boundaries between domains.

To examine the nature of the currents within the domain in more detail we consider the central plane, $z = 0.5$, and show in Figure 5.6 contours of current in that plane for a sequence of increasing spin-angles. The drop in the spinning velocity at the outside of the flux sources is seen to result in four 'rings' of current at early spin-angles, with the strongest current seen at the intersections of the rings where the interaction of spinning motions produces a shearing effect. By $\theta = 0.55$, the central current sheet together with four wings of current has formed; this characteristic shape persists throughout the remainder of the simulation. The initial rings of current have been forced outwards by magnetic pressure. This causes a build up of current on the side boundaries of the box which ultimately allows flux to leave the box. The wings of current may be identified with quasi-separatrix current sheets early on in the experiment when they perfectly outline the boundaries between the flux domains and are seen to grow with spin-angle, extending close to the boundaries of the domain. The current structure at these early stages of the experiment is therefore similar to that predicted by Green (1965). As reconnection begins and the evolution is no longer quasi-static, we observe (Figure 5.5) that the wings of current do not align with the change of flux connectivity. By considering the variation of certain quantities along a perpendicular section to the structures, we identify them now as contact discontinuities (see, for example Priest, 1982). Taking spin-angle $\theta = 1.45$ as an example, we plot in Figure 5.7 the tangential and normal components of the magnetic field, plasma velocity and current, together with the vorticity, density and total pressure along a line (illustrated by the white line in Figure 5.6) perpendicular to the current wings in the central plane. It is seen that there is no plasma flow across (i.e. normal to) the structures but that a discontinuity in the tangential velocity component exists. In addition, the total pressure is continuous along the entire cross-section whilst the density shows a jump across both the current structures (such a density jump is arbitrary in the theory of contact discontinuities) and there is a normal field component across the structure so distinguishing it from a tangential discontinuity. In order to determine why there is a discrepancy between the locations of the quasi-separatrices and of these wings of current we must first consider the nature of both the central current sheet and the reconnection mechanism. We therefore return to this point later.

Consider now the evolution of the quasi-separator current sheet. We will refer to its extent in the z-direction as 'height', its length in the xy-plane as 'length' and the remaining dimension, its thickness in the xy-plane as 'width'. As seen in the cross-sections through the current structure (Figure 5.6), after its initial formation, the length of the sheet increases with spin angle. The growth in length is almost linear until, at $\theta \approx 1.1$, the ends of the sheet (in the horizontal direction, along the $y = -x$ line) bifurcate to form two Y-type structures which lie along the quasi-separatrices of the field. No further lengthening of the
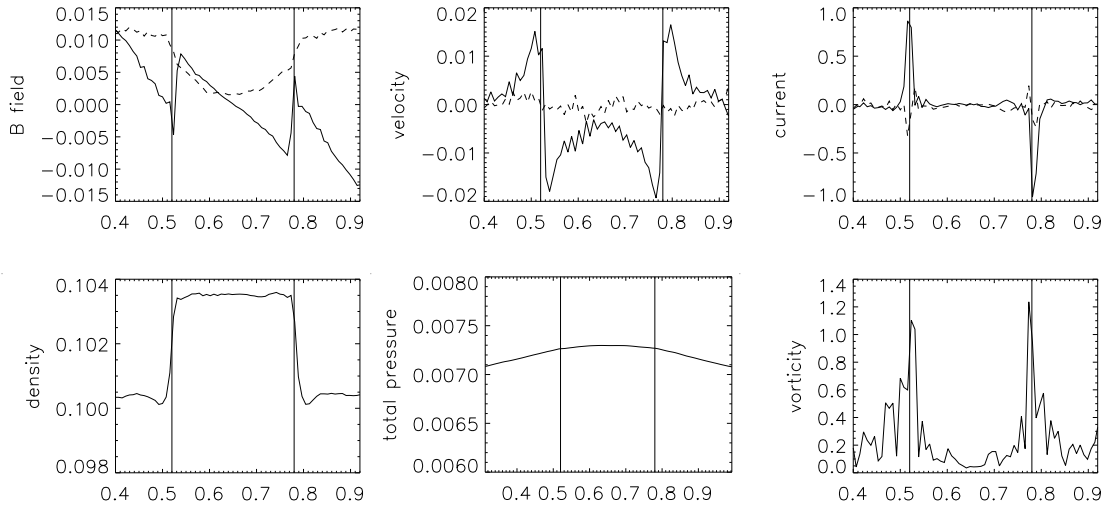
Figure 5.7: Tangential (solid lines) and normal (dashed lines) components of the magnetic field, velocity and current (upper plots) together with the density, total pressure and $|\nabla \times \mathbf{v}|$ (lower plots) along the line $y = 1.3 - x$ at spin-angle $\theta = 1.45$ for the central plane $z = 0.5$. The vertical lines denote the location of the current 'wings' along that line (as seen in Figure 5.6). The variations of these quantities are evidence for a contact discontinuity at these locations.

sheet occurs, indeed it shrinks slowly with further increase in spin angle. The current is predominately in the $\hat{\mathbf{z}}$-direction and this component changes sign at both ends of the sheet, as shown in Figure 5.8 where spin-angle $\theta = 2.26$ has been considered as an example. In two-dimensional situations, reversed currents near the ends of diffusion regions have been observed in numerical experiments (Biskamp, 1986) and are seen to slow down the outflowing jets in these cases. We therefore proceed to examine the nature of the plasma velocities.

5.3.3 Plasma Velocities and Reconnective Behaviour

We show, in Figure 5.9, vector field plots of (v_x, v_y) in the central plane at various spin-angles (note that the third velocity component, v_z is an order of magnitude less than both v_x and v_y). At early spin-angles, $\theta = 0.35$ for example, the velocity in the central plane is clearly similar to that imposed on the upper and lower boundaries, with four counter-rotational flow regions present. The intersection of these regions results in a stagnation flow profile stronger than the remaining rotational components and it is this stagnation flow which dominates the later velocity profiles. Plasma flows into, and is ejected from, the central current sheet. The inflow streamlines are seen to be curved and diverging. The outflow, particularly at later spin angles, is diverted out along the quasi-separatrices of the field.

Let us now consider the nature of the inflow region in more detail, paying particular attention to the magnetic field and gas pressure. We show in Figure 5.10 profiles of the gas pressure and magnetic pressure in the inflow region for the central plane. We observe the gas pressure to be decreasing as the plasma flows in toward the quasi-separator current sheet, suggesting the inflow is undergoing an expansion. In addition
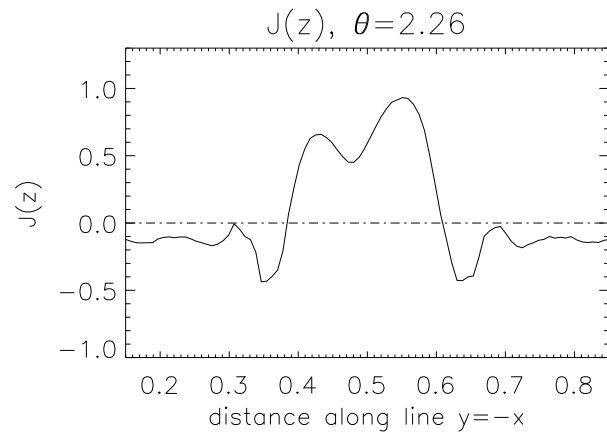
Figure 5.8: Strength of the z-component of the electric current in the central plane $z = 0.5$ along the line $y = -x$ which passes along the central current sheet. A spike of reversed current is seen at both ends of the sheet.
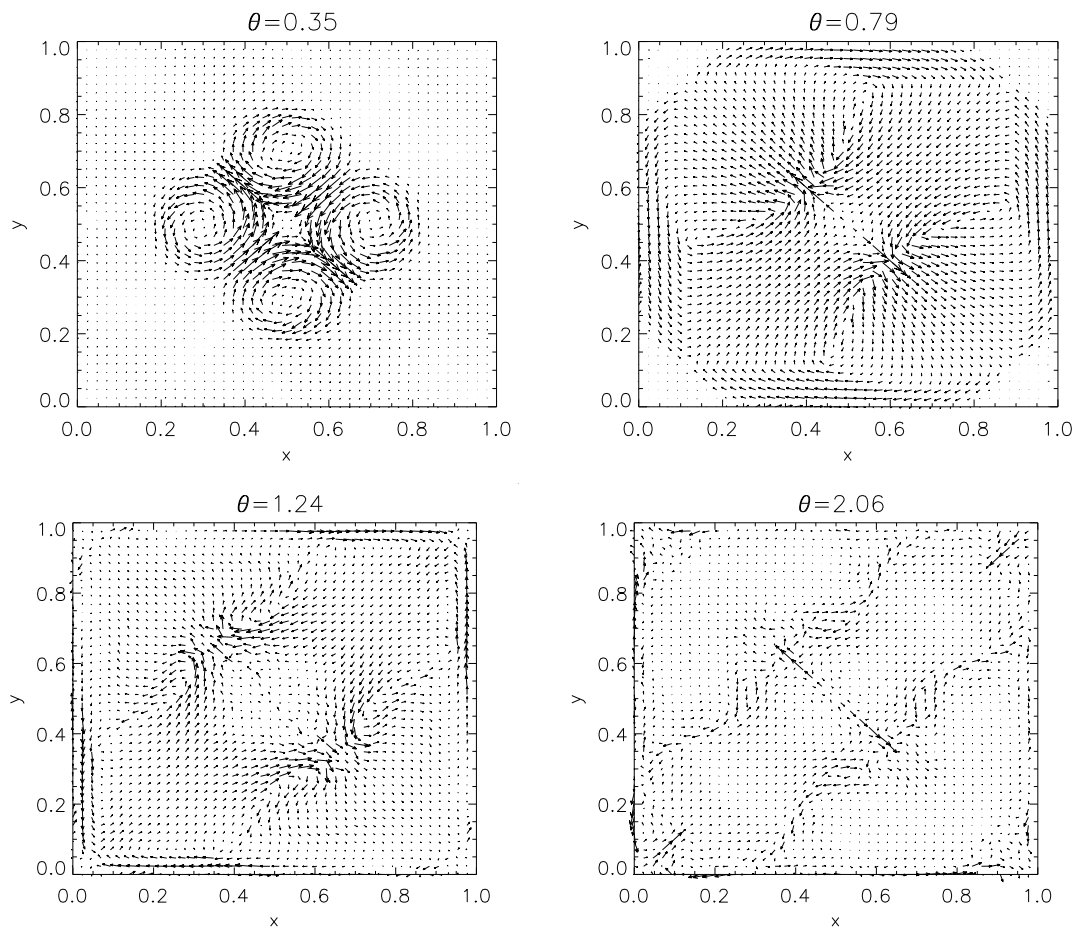
Figure 5.9: Plasma flows in the central plane, $z = 0.5$ for a sequence of increasing spin-angles showing the key stages in the velocity evolution. A stagnation flow forms with strong outflow jets along the central current sheet.
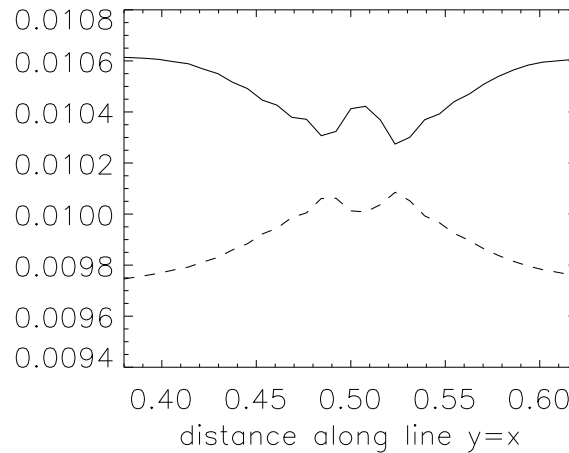
Figure 5.10: Behaviour of the gas (solid line) and magnetic (dashed line) pressures in the inflow region. Here a cut along the line $y = x$ has been taken at spin angle $\theta = 1.37$ for the central plane $z = 0.5$. The gas pressure is seen to decrease whilst the magnetic pressure increases.

the reverse behaviour is observed in the magnetic pressure profile which increases toward the current sheet so that the expansion may be further characterised as of the slow-mode type.

Combining all these pieces of information we note that the situation is strongly reminiscent of the *flux pile-up* regime (Priest and Forbes, 1986) with its characteristically long diffusion regions. This model was extended further in the non-uniform theory of Priest and Lee (1990) to also take reversed current spikes and separatrix plasma jets into account. Shocks in their (incompressible) model are rather weak and indeed we cannot consider any of the structures in this 3D experiment as true shocks. There are, however, several differences between the 2D theory and this 3D model. In the reconnection process, magnetic flux of types Aa and Bb are brought together and reconnect across the central quasi-separator current sheet to form flux of types Ab and Ba. However, as distinct from the 2D theory, in this 3D case the magnetic field has an O-type structure in cross sections of constant z (Figure 5.11(b)) and it is the vertically orientated flux that is reconnected. Thus reconnection can occur all along the quasi-separator current sheet and the location of reconnection will depend on where the flux comes into contact with the sheet. With reconnection occurring everywhere along the sheet, significant amounts of magnetic flux is being carried into the sheet close to the centre of the domain. Figure 5.11(a) shows four particular field-lines which illustrate this process, together with contours of current in the central plane. The sheared field-lines in the inflow regions (the red line of type Bb and light blue line of type Aa) are carried into the central current sheet where they reconnect. The strong outflow then carries the reconnected field lines out of the current sheet and they are seen to have less shear (the dark blue line of type Ab and yellow line of type Ba), with these example lines being almost straight. Note that the field lines shown in this figure are for illustrative purposes only and all taken at the same spin-angle, i.e. they do not represent the same lines pre- and post-reconnection.

The magnetic flux that pierces the central plane close to the contact discontinuity is twisted in such a way that it passes through the quasi-separator current sheet towards the top or bottom of the box (Figure 5.12)
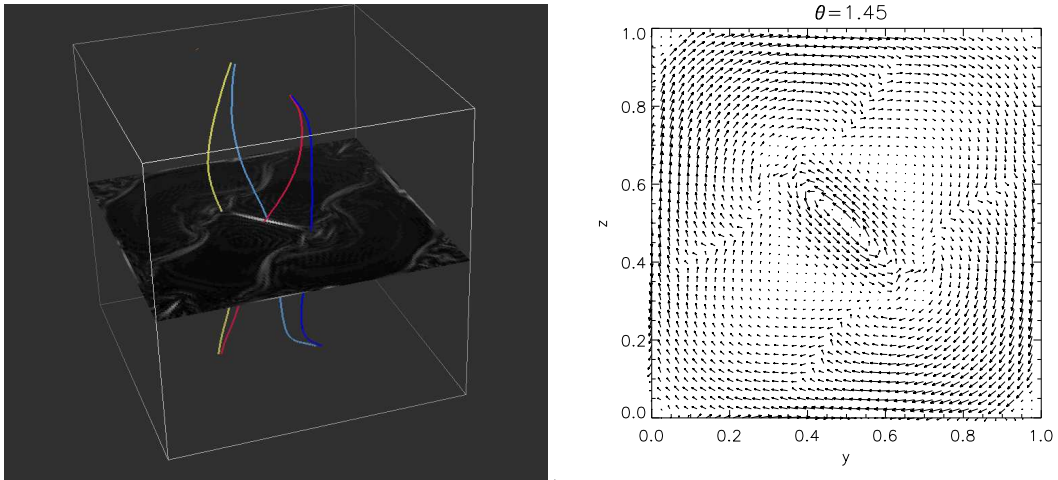
Figure 5.11: (a) Four illustrative field-lines being carried into the central current sheet before reconnection (red, light blue) and away from the sheet having reconnected (dark blue, yellow), together with contours of current in the central plane. The post-reconnection field lines are seen to have less shear than the pre-reconnection lines. (b) An X-type field structure is present only in vertical cross-sections, while in horizontal sections, such as that illustrated here, the field has an O-type topology.

and reconnects there. Thus the reason behind the misalignment of the wings of current (identified with contact discontinuities) and separatrices of the field becomes evident. Reconnection is taking place along the entire height of the quasi-separator current sheet but this change of connectivity is not immediately apparent at different heights within the domain. The contact discontinuities themselves are an artifact of the initial flux distribution and the spinning motions imposed on that distribution. They outline the divide between flux types which would have existed had no reconnection taken place.

5.4 Discussion

Examining in more detail the flux connectivity diagrams for the mid-plane (shown in Figure 5.5), an interesting pattern of behaviour is seen within the central current sheet at intermediate spin-angles (see $\theta = 0.92, 1.24$ for example). As an illustration, an enlargement of this region is shown at spin-angle $\theta = 1.19$ in Figure 5.13 (*left*). Although in Section 5.3 we have somewhat loosely referred to the 'quasi-separator current sheet', this diagram, with its regions of 2D isolated flux-connectivity type, indicates the magnetic connectivity of the region is really very complex, and only becomes simple again in later stages of the experiment (as shown in Figure 5.13 (*right*)). This effect does not result from a lack of resolution of the current sheet in the later stages; the current sheet remains well-resolved throughout the experiment through the use of hyper-resistivity (see Nordlund and Galsgaard, 1997). A detailed investigation into the magnetic topology of a particular 3D MHD reconnection experiment was carried out by Haynes et al. (2007), where a sequence of bifurcations was identified which resulted in the initial field topology becoming increasingly complex, before eventually simplifying in the later stages of the experiment. From the preliminary investigations presented here, it seems that a complex pattern of magnetic connectivity is also present in this system. It would be interesting to carry out a more detailed investigation into the connectivity pattern and
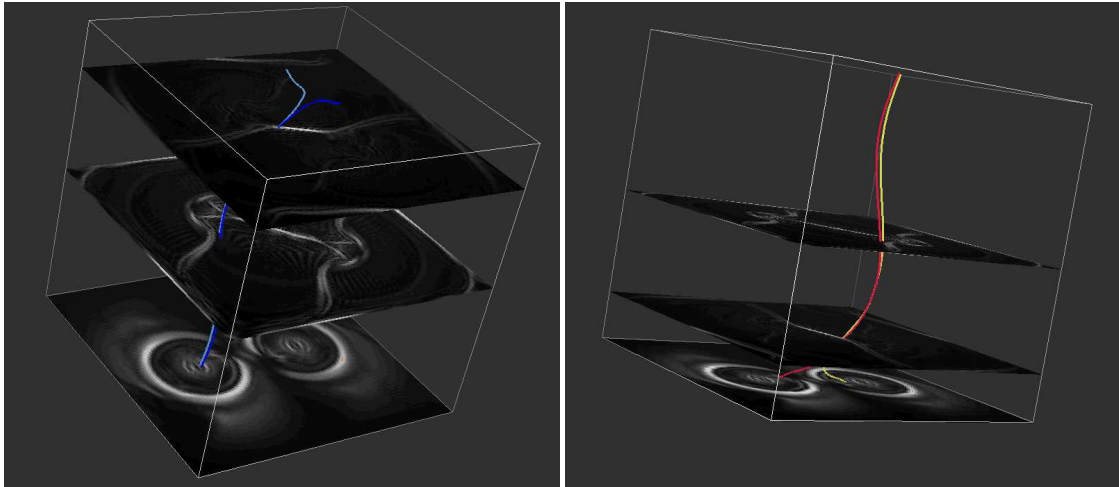
Figure 5.12: Magnetic field lines traced from the central plane ($z = 0.5$) close to the separatrices of the field and away from the quasi-separator current sheet in that plane. The field lines pass through the quasi-separator current sheet toward the top (left hand figure) or bottom (right hand figure) of the box where they reconnect. Superimposed are contours of current in various planes of constant height.

its evolution and consider the implications for the reconnection process. This, however, is beyond the scope of the simple descriptive content of this chapter.

As discussed in Section 5.1, one of the motivations to consider reconnection in these misaligned flux tubes is to make a comparison with the case of the same spinning footpoint motions imposed on perfectly aligned flux tubes, as described by De Moortel and Galsgaard (2006b) and, in particular, to examine how the nature of reconnection differs between the two situations.

The spin-angle for the onset of reconnection is $\theta = 1.46$ in the aligned case and $\theta = 0.40$ in this misaligned situation. The difference in spin-angle ($\Delta\theta = 1.06$) corresponds to a time difference in the solar corona of 0.6 hours (for a discussion of how the non-dimensional quantities described in this experiment relate to coronal parameters see De Moortel and Galsgaard (2006a)). This is a significant difference between the two cases given that the coronal recycling time is estimated to be as little as 1.4 hours.

The likely reason behind the disparity in reconnection onset times can be found by comparing the plasma velocities and build-up of current in the two experiments. In the misaligned case, the imposed boundary flows propagate into the box in such a way as to form a stagnation-flow early in the experiment, as shown at $\theta = 0.35$ in Figure 5.9. However, in the aligned case, the counter-spinning boundary flows effectively cancel as they propagate into the mid-plane, and so a stagnation-flow is only initiated at a later stage through the effect of magnetic pressure. Stagnation-flows have the effect of amplifying current concentrations and, accordingly, a build-up of sufficient current to allow for reconnection to take place occurs sooner in the misaligned case. The evolution of maximum $|\mathbf{j}|$ in a central square of side-length 0.4 and in the mid-plane ($z = 0.5$) with spin-angle is shown, for both experiments, in Figure 5.14(*left*). Although the initial current development begins in both experiments at the same spin angle, the initial growth is faster for the misaligned case. In both situations there then follows a period where the maximum current decreases with spin angle before undergoing a second phase of increase. In the aligned case it is
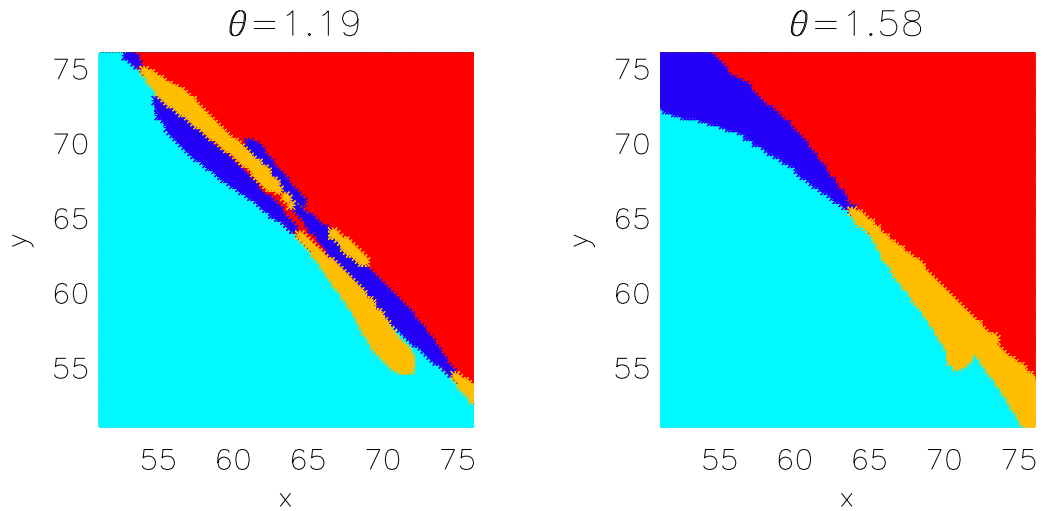
Figure 5.13: Flux connectivities in a central square within the mid-plane encompassing the non-ideal region, for (*left*) $\theta = 1.19$ and (*right*) $\theta = 1.58$. The colour scheme is the same as that for Fig. 5.5. A complex topology is present in the early stages of the experiment, becoming much simpler as the spin-angle increases.
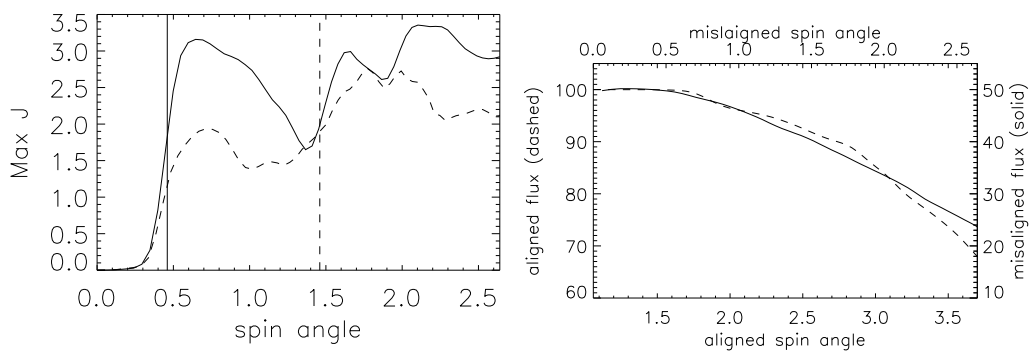
Figure 5.14: (*left*) The change in maximum current (within the central square of side 0.4 in the $z = 0.5$ plane) with spin angle. The thick solid line represents the case of $\pi/2$ misaligned flux sources and the thick dashed line the case of aligned flux sources. The vertical lines mark the spin angle at which reconnection begins in both cases. (*right*) Flux connectivities for the misaligned (solid line) and aligned (dashed line) cases, as described in the main body of the text.

only in this second phase of current growth that reconnection begins (vertical dashed line).

The next important comparison is in how, once initiated, the rate of reconnection differs between the two setups. In order to make this comparison we consider how the percentage of flux with certain connectivities changes with spin angle. In the misaligned case flux with connectivity Aa is considered. This flux-type initially constitutes 50% of the flux from source A, and the percentage decreases with spin-angle after reconnection begins. For the aligned case the percentage of flux remaining at its original flux source is considered (for one of the sources on the lower boundary). This is initially 100% of the flux in the source and again decreases with spin-angle after the onset of reconnection. These quantities are represented in Figure 5.14(*right*) where the x-axes for both cases have been aligned in such a way that the onset of reconnection is coincident. We see that during the initial phase of reconnection the rate of decrease of flux of the considered connectivity is very similar in both cases. This suggests that the same reconnection mechanism may be responsible for the evolution of both systems. As spin-angle increases a change in the gradient of flux connectivity occurs in the aligned case, at aligned spin-angle $\theta = 2.8$, indicating flux is now changing connectivity faster. Examining the flux evolution in that experiment in more detail we observe that this discrepancy is due to flux *leaving* the box, i.e. additional reconnection occurring across the boundaries of the domain, rather than a change in the reconnection mechanism within the central current sheet. Thus it is interesting to note that although the current sheet has a greater cross-sectional length in the aligned than the misaligned case (with the additional flux domains in the misaligned case restricting current sheet growth), this does not result in a different rate of reconnection.

One notable difference found between the two experiments is in the geometry of the central current sheet. In the aligned case the sheet is straight, while in the misaligned case a twisted sheet forms as a result of the $\pi/2$ difference in orientation of the upper sources. In the misaligned case the initial potential field contains four distinct flux domains which allows for the subsequent development of quasi-separatrix current sheets; these are necessarily absent in the aligned experiment (or, alternatively, can be considered as coincident with the quasi-separator current sheet). However we have shown that the quasi-separatrix current sheets in the misaligned case, which later become contact discontinuities, are not important in the reconnection process itself. The comparable reconnection rates found in the two experiments confirms this to be the case and is further evidence that the reconnection process is concentrated in the quasi-separator current sheet.

Finally we note that there are several limitations in the experimental setup. Perhaps the most important of these is in the plasma β which, since the field strength decreases rapidly moving away from the upper and lower boundaries toward the centre of the domain whilst the gas pressure profile is initially uniform, is significantly higher than that found in the solar corona. In addition, the experiment ends at $\theta = 2.64$ when periodic boundary conditions begin to affect results. This could be seen as a shortcoming; perhaps further interesting dynamics would have been found at later spin angles. However, bearing in mind the counter-spinning nature of the drivers, we can consider the true rotation of a single source to be $\theta = 2 \times 2.64$, already a significant angle compared with observed solar-like flux rotations (see, for example, Brown et al., 2001). As mentioned several times, the magnetic sources themselves are non-ideal and so a certain amount of slippage of the field occurs within each source. Although we do not consider such behaviour to be of great consequence on the global field-evolution, the non-idealness does prevent us from tracking the behaviour of individual field-lines with spin-angle. It would be highly informative to examine such behaviour and

worthwhile therefore to re-run the experiment with an ideal boundary condition imposed. Such a condition could be achieved by specifying a suitable resistivity profile, as considered, for example, by Pontin et al. (2005a).

5.5   Summary

We have described a simple numerical experiment in which the magnetic footpoints of two, initially potential, intertwined flux tubes are spun, while their positions remain fixed. Magnetic flux is divided into four domains and the footpoint motions act to twist the flux and create current sheets at the boundaries between the domains. A central twisted quasi-separator current sheet forms early on in the experiment and a stagnation flow develops. The flow brings oppositely directed flux in toward the quasi-separator current sheet and reconnection takes place everywhere along it. The quasi-separator current sheet grows in cross-sectional length before its endpoints bifurcate to form Y-type points. In planes of constant height the situation strongly resembles the 2D nonlinear reconnection models of Priest and Lee (1990), with their fast reconnection rates. Strong jets of plasma flow across the magnetic separatrices and regions of reversed current are found close to the ends of the diffusion region. The full three-dimensionality of the experiment modifies the regime, with the magnetic field having a locally 2D O-type structure. In addition, the field topology is found to be highly complex. One time-dependent effect is that the current sheets which initially form along the boundaries between flux domains (i.e. quasi-separatrix current sheets) move away from these boundaries as the sources are spun and reconnection begins to occur. They are, at later spin angles, instead identified as contact discontinuities.

The experiment described here can be compared with the non-generic case of aligned magnetic flux tubes given by De Moortel and Galsgaard (2006b). Any degree of misalignment of the magnetic flux tubes has a significant effect on the magnetic connectivity of the system, since four flux domains will initially be present (instead of just two in the aligned case). In both experiments a central quasi-separator current sheet forms in the centre of the domain and in the misaligned case, the current structure is modified by the presence of four wings of current that initially outline the additional separatrices of the field. Once reconnection begins, however, the rate at which magnetic flux changes its connectivity is very similar for both cases. Indeed reconnection in the misaligned case is found to occur only along the central quasi-separator current sheet; the extra wings of current are not found to modify the process. These two observations suggest the same reconnection mechanism to be operating in both cases. An important difference is found regarding the onset time for reconnection. It is found that strong currents develop at earlier spin-angles in the misaligned case and that, as a result, magnetic reconnection begins sooner; mapping the relevant spin-angles to coronal timescales the onset time is found to be 0.23 hours in the misaligned case but 0.85 hours in the aligned case. Combining this chapter and De Moortel and Galsgaard (2006b) the two most extreme situations of flux-tube alignment have been considered and we are able therefore to deduce the implications for any general case. We expect reconnection to begin sooner the more tangled the initial magnetic flux-tubes but for it to proceed at the same rate once initiated.

Chapter 6

Low-Order Dynamo Models

6.1 Introduction

Direct evidence of solar magnetic activity through the observations of sunspots dates back to the early 1600s, with indirect evidence coming from both measurements of cosmogenic radioisotopes in tree rings and ice cores over the past 10,000 years. A systematic record of activity in other late-type stars began in 1966 with the Mt. Wilson Ca II H+K project (Duncan et al., 1991, Baliunas et al., 1995, Saar and Brandenburg, 1999). The survey has given rise to many studies on the dependence of activity with such large-scale parameters as stellar age, mass and rotation rate.

The stars in the Mt Wilson survey show several distinct types of activity. Baliunas et al. (1995) divided the stars into four categories based on the variability in their emission: those with no significant variability, those with long-term changes in emission (on a timescale greater than 20 years), those with irregular emission and those with cyclic variation. The Sun itself falls into the final category. The activity periods in the cyclic stars range from around 20 years to just 2.5 years, so the Sun's own average cycle period of 11 years falls in the centre of the observed range. Considering the sign reversal of the magnetic field along with the 11-year sunspot cycle gives a periodicity of 22 years for the solar magnetic cycle. Detailed examination of the sunspot cycle record shows a variation in the length of the activity period from 9 to 14 years, with a longer term modulation of the cycle on a period of about 80 years (the Gleissberg cycle) believed to be present. In addition, the Sun has undergone several grand minima (Beer et al., 1998), the last of which being the Maunder minimum during 1645-1715 AD (Eddy, 1976, Hoyt and Schatten, 1996). Proxy data, for example ^{10}Be in ice-cores (Wagner et al., 2001), indicate a statistically significant spectral peak with frequencies corresponding to approximately 205 and 2100 years. It is possible, therefore, that Grand Minima may occur in clusters with a period of just over two-hundred years and that the clusters reoccur on a timescale of 2100 years. There is not currently enough data to allow us to infer similar events in other stars.

From a physical point of view, magnetic activity in solar-type stars is likely to be a result of hydro-magnetic dynamo action (Parker, 1955, Ossendrijver, 2003). Writing $\mathbf{B} = B_r \mathbf{e}_r + B_\theta \mathbf{e}_\theta + B_\phi \mathbf{e}_\phi$ it is

conventional to discuss the origin of global stellar fields in terms of their toroidal ($B_r\mathbf{e}_r + B_\theta\mathbf{e}_\theta$, in the direction of the differential rotation) and poloidal ($B_\phi\mathbf{e}_\phi$) components. A mechanism for the generation of toroidal field from the poloidal component (known as the Ω-effect; Parker 1955) and for the subsequent regeneration of poloidal field from the toroidal component (the α-effect; Parker 1955) must exist. Solar observations, for example the tracking of surface features such as sunspots, indicate a differential rotation, with the equator rotating faster than the poles. Helioseismology has shown this persists throughout the convection zone (Schou et al., 1998), with the rotation varying mostly latitudinally. In a thin layer between the convection zone and the radiative layer – known as the tachocline – a strong radial shear in the angular velocity exists. Thus differential rotation in the solar interior generates the toroidal field by stretching the poloidal field lines, a process known as the Ω-effect. It also acts to amplify the toroidal field, and if the Ω-effect occurs largely in the tachocline layer then flux storage (due to the sub-adiabatic temperature gradient and consequent suppression of buoyancy there) can occur over timescales sufficiently long for strong fields to be built. Evidence of surface differential rotation has been found in other stars and it is very likely that these persist to greater depths, as in the Sun. Thus, the Ω-effect is possibly a common mechanism for toroidal field generation in stars.

For the re-generation of the poloidal field from the toroidal component several mechanismas have been invoked: for example, a convective alpha-effect throughout the convection zone based on the twisting of toroidal fields by helical turbulence (Parker, 1955, Steenbeck and Krause, 1969, Gilman and Glatzmaier, 1981, Brandenburg et al., 1990, Tobias, 1997); an α-effect in or near the tachocline arising from instabilities in the plasma flows or buoyantly rising magnetic flux tubes (Ferriz-Mas et al., 1994, Schmitt et al., 1996, Thelen, 2000, Dikpati and Gilman, 2001) and the decay of tilted bipolar sunspot pairs near the solar surface, known as the Babcock-Leighton mechanism (Babcock, 1961, Leighton, 1969, Durney, 1997, Dikpati and Charbonneau, 1999, Nandy and Choudhuri, 2002, Chatterjee et al., 2004).

Many solar and stellar dynamo models have been proposed that try to account for the flux production, cycle period and amplitudes (Durney, 1997, Brooke et al., 2002, Bushby, 2003, Chan et al., 2004, Charbonneau et al., 2004, and references therein), as well as other well-known features observed on the Sun, such as the equatorward drift of sunspots during the cycle and the evolution of the surface radial field; some have included related (and possibly integral) processes such as magnetic buoyancy and meridional circulation (Ferriz-Mas et al., 1994, Nandy and Choudhuri, 2002, Chan et al., 2004, Charbonneau et al., 2005). These models range from detailed numerical simulations to extensive sets of partial differential equations with various physical motivations. Full simulations of the dynamo process with high magnetic Reynolds numbers are currently out of reach computationally — although see Brun et al. (2004) for a global simulation of dynamo action in a turbulent rotating spherical shell. Much work has centered on mean field dynamo theory, with axisymmetric α-ω dynamos attracting the most attention.

A self-consistent magnetohydrodynamic treatment of many of the mechanisms thought to be behind stellar dynamos, such as differential rotation and other large-scale flows, is a formidable task. In addition, it is highly likely that the nature of the dynamo, for any given star such as the Sun, has evolved over the lifetime of the star with the evolution of the properties of its convection zone, primarily mediated through spin-down and angular momentum losses via stellar winds (Mestel and Spruit, 1987). Therefore a brief consideration of some of the important parameters that determine the behaviour of stellar dynamos is useful (for more detailed discussions, see, for example, Noyes et al. (1984b) and Montesinos et al. (2001)).

A measure of the efficiency of the dynamo mechanism is the dynamo number (N_d) – the ratio of the source terms to the dissipative terms in the dynamo equations – which depends on various physical properties of the stellar convection zone. Another important parameter that essentially describes the evolutionary state of stellar convection zones is the Rossby number, R_o. It can be shown that $N_d \sim 1/R_o{}^2$ (see, for example, Durney and Latour, 1978). Since the rotation period, depth of stellar convection zones and convective turn-over time evolves with stellar evolution, both N_d and R_o are expected to change over any given star's lifetime. Specifically as stars age, their Rossby number increases with the corresponding increase in rotation period. It has been shown that the groups of stars with irregular and regular activity are distinguished by their Rossby number (Noyes et al., 1984a, Hempelmann et al., 1996). Stars with $R_o < 1$ show irregular and strong emission, while the regular and constant stars are those with $R_o > 1$. A possible explanation for this division is to explain the magnetic activity as being governed by a nonlinear dynamical system whose output changes from constant to periodic to chaotic as a governing parameter (such as the dynamo number) linked to rotation is increased. The intensive computational nature of full numerical dynamo models means that a full exploration of their behaviour in a wide range of parameter space is not easily achievable. In this thesis we adopt a different and parallel approach. We construct simple models which may have a similar underlying mathematical structure as that found in the full system. This enables us to explore a wide range of parameter space in the models, corresponding to the wide variety of stellar behaviour that is expected to be governed by the same physical principles. Studies of this kind are therefore complementary to works such as those cited in the earlier paragraph.

The construction of low-order models of the solar dynamo has traditionally utilised one of two alternative approaches. The first is to derive sets of Ordinary Differential Equations (ODEs) via a truncation of the Partial Differential Equations (PDEs) of mean-field electrodynamics (Zeldovich et al., 1983, Martens, 1984, Weiss et al., 1984, Jones et al., 1985, Schmalz and Stix, 1991, Roald and Thomas, 1997, Covas and Tavakol, 1997). This approach has the advantage that each term in the truncated set of ODEs has an obvious physical interpretation as it has been derived from an analogous term in the PDEs. The lowest order truncation, resulting in just two governing ODEs, is known not to produce dynamo action, which is in itself suggestive of a drawback of such a truncation procedure, namely that the dynamics associated with truncated models is often fragile and sensitive to the level of truncation.

A second approach is to construct low-order models based on normal-form equations utilising the theory of nonlinear dynamics, either by using symmetry arguments or by bifurcation analysis (Tobias et al., 1995, Knobloch and Landsberg, 1996). Here the dynamics found can be shown to be generic and therefore robust. However, the drawback in this case is that the physical interpretation of a set of low-order equations is less transparent as there is no obvious physical analogue for a given term in the equations.

We explore both approaches here. In the next section we examine a robust model derived using normal-form theory. In the following chapter, Chapter 7, we adopt a novel approach to the lowest-order truncation of the full PDEs, taking the physical separation of source terms known to exist in the solar dynamo into account in a simple way. As a result the two ODEs obtained by truncation of the PDEs are converted into two delay differential-equations (DDEs) and dynamo action is then found.

The results of this chapter are based on Wilmot-Smith et al. (2005a) and Wilmot-Smith et al. (2007b).

6.2 Construction of the Model

The model considered in this chapter is an extension of that derived in Tobias et al. (1995). In that paper, a third-order model was derived using a Poincaré-Birkhoff normal form for a saddle-node–Hopf bifurcation, to obtain a system exhibiting generic and therefore robust behaviour. This normal form was chosen since it has a bifurcation structure that gives qualitatively similar behaviour to that observed in stars as solutions along a cut through parameter space are examined.

Considering stellar magnetic activity observations we expect, qualitatively speaking, that, as the evolution of a star is tracked backwards in time (i.e. as its rotation rate increases), periodic cyclic solutions will bifurcate from a steady free-field state in a supercritical Hopf bifurcation. These regular cyclic solutions will, in turn, give way to trajectories lying on a two-torus after a supercritical secondary Hopf bifurcation, reflecting periodic solutions with amplitude modulation in time. Finally, this activity should become chaotically modulated to account for those stars with irregular activity. Indeed, such a bifurcation structure is mirrored in mean-field PDE models as the non-dimensional measure of rotation rate (the dynamo number D) is increased (Tobias, 1996, Pipin, 1999, Bushby, 2005).

In the model of Tobias et al. (1995), the magnetic field was decomposed in the usual way into its toroidal part, represented by x, and its poloidal part, represented by y. The third coordinate of the system, z, represents all the hydrodynamics of the system, including as differential rotation and convection. Though a consideration of normal-form theory, the basic system is taken to be given by

$$
\begin{aligned}
\dot{z} &= \mu - z^2 - \left(x^2 + y^2\right), \\
\dot{x} &= \left(\lambda + az\right)x - \omega y, \\
\dot{y} &= \left(\lambda + az\right)y + \omega x.
\end{aligned}
\tag{6.1}
$$

For $\mu > 0$ the equations (6.1) have have two fixed points, P^+ and P^-, given by the solutions to $x = 0, y = 0, z = \pm\sqrt{\mu}$. These correspond to field-free, purely hydrodynamic, solutions where the flows are statistically steady and arise from the saddle-node bifurcation at $\mu = 0$. Thus the parameter μ controls the hydrodynamics of the system, so is related to effects such as thermal forcing and rotation. The term $(x^2 + y^2)$ in the $\dot{z}$-equation, being quadratic in the magnetic field, represents the back reaction of the Lorentz force on the field. Its coefficient has been chosen to be less than zero so that the secondary Hopf bifurcation is supercritical.

By setting $z = 0$, we see that λ gives the growth-rate (i.e. strength of the dynamo action) of x and y and ω the basic cycle frequency (the location of the bifurcation curves in the model is independent of ω). In a more complicated PDE model these features would be linked with the dynamo number.

For the system of equations (6.1) the secondary Hopf bifurcation is found to be degenerate and, to break this degeneracy, a cubic term must be added to the model. A cubic term, cz^3, was added to the $\dot{z}$ equation and to take $c < 0$ so that solutions on the z-axis remain finite. This inclusion introduces another fixed point to the system, again on the z-axis and and associated additional line of saddle-node bifurcations (at $\mu = 4/27c^2$).

The system derived thus far is axisymmetry essentially two-dimensional – it may be written in cylindrical polars as:

$$
\begin{aligned}
\dot{z} &= \mu - z^2 - r^2 + cz^3, \\
\dot{r} &= \lambda r + azr, \\
\dot{\phi} &= \omega.
\end{aligned}
$$

The addition of a symmetry-breaking term would add physical realism to the system and making the system fully three-dimensional would allow for chaotic dynamics. For these reasons the authors chose to add a cubic term to the $\dot{x}$ equation to break the normal form axisymmetry. However, the exact choice of term is arbitrary and the term chosen in Tobias et al. (1995) is one proportional to $(x^2 + y^2) z$, the motivation being to preserve the invariance of the z-axis. Thus the system of ODEs now takes the form

$$
\begin{aligned}
\dot{z} &= \mu - z^2 - (x^2 + y^2) + cz^3, \\
\dot{x} &= (\lambda + az)x - \omega y + dz(x^2 + y^2), \\
\dot{y} &= (\lambda + az)y + \omega x.
\end{aligned}
\tag{6.2}
$$

See Tobias et al. (1995) for further details of the model's derivation.

In order to demonstrate the type of behaviour that such a model yields, Tobias et al. (1995) fixed all parameters except for λ and μ and chose a parameterized path through the $\lambda - \mu$ plane to demonstrate the bifurcation structure of the model. In summary, the showed that, as the controlling parameter was increased, purely hydrodynamic solutions lost stability in a primary Hopf bifurcation to oscillatory solutions. In turn these gave way to quasiperiodic solutions, where the basic cycle is modulated on a longer timescale and solutions lie on a two-torus in phase-space. Further increase in the parameter led to a breakdown of the torus and a transition to chaos. The solution then took the form of active periods, interspersed chaotically with minima. Such solutions are associated with close-approach to an invariant manifold and near heteroclinicity.

However, as noted by Ashwin et al. (2004), a limitation of the model is that the choice of term to break the normal form axisymmetry in Tobias et al. (1995) results in a loss of equivalence of the system under the transformation $x \rightarrow -x, y \rightarrow -y$ which corresponds to $B \rightarrow -B$. In this chapter we choose an alternative term, which does not suffer from the above disadvantage, to break the axial symmetry. Again, the exact choice of cubic term is arbitrary; available terms are, for example, x^3, xz^2, xy^2, xyz, $(x + y) z^2$ etc. Similarly the choice made in Tobias et al. (1995) of including this term in the $\dot{x}$ equation was arbitrary, the $\dot{y}$ equation would also be suitable. In view of these considerations we choose to add a term proportional to $(x^3 - 3xy^2)$ to the $\dot{x}$-equation and one proportional to $(3x^2y - y^3)$ to the $\dot{y}$-equation. Thus the model becomes

$$
\begin{aligned}
\dot{z} &= \mu - z^2 - (x^2 + y^2) + cz^3, \\
\dot{x} &= \lambda x - \omega y + azx + d(x^3 - 3xy^2), \\
\dot{y} &= \lambda y + \omega x + azy + d(3x^2y - y^3).
\end{aligned}
\tag{6.3}
$$

This new system of equations is invariant under the transformation $x \rightarrow -x, y \rightarrow -y$ and the z-axis remains invariant – these are the two basic properties to be satisfied by the symmetry-breaking term. The physical motivation behind our exact choice becomes clear when the system is written in cylindrical polars:

$$
\begin{aligned}
\dot{z} &= \mu - z^2 - r^2 + cz^3, \\
\dot{r} &= (\lambda + az)r + dr^3 \cos(2\phi), \\
\dot{\phi} &= \omega + dr^2 \sin(2\phi).
\end{aligned}
\tag{6.4}
$$

In the following section we examine some of the properties of this model.

6.3   Results

We examine the behaviour of the system as λ and μ are varied and fix the parameters a, c, d, and ω as

$$
a = 3, \quad c = -0.4, \quad d = 0.4, \quad \omega = 10.25.
$$

Following Tobias et al. (1995) we have chosen to fix $a = 3$ and $c = -0.4$ so that both the line of saddle-node bifurcations at $\mu = 4/27c^2$ and secondary Hopf bifurcations at $\lambda = -2a/3c$ are far from the origin as shown in Figure 6.1. As with system (6.2) the choice of ω does not greatly alter the bifurcation structure, but it does change the ratio of the modulation cycle to the underlying cycle. We have chosen $\omega = 10.25$, since it results in a ratio similar to that observed in the Sun.

To allow us to choose a suitable path through parameter space along which to study solutions of (6.3) we examine the bifurcation set for the system; this is shown in Figure 6.1(a). We see that the line of secondary Hopf bifurcations, which for $d = 0$ was identical to the positive μ-axis, has moved leftward in our new model (6.3). A heteroclinic region, which is shaded in the diagram, replaces the degenerate heteroclinic bifurcation that exists when $d = 0$, as in Tobias et al. (1995). We have not indicated all the bifurcations lying inside this wedge owing to the complexity of the region, some details of which are described in for example Champneys and Kirk (2004). The main dynamical features observed are described as follows, and a small section is illustrated in Figure 6.1(b).

Trajectories within this region lie on a torus, and the rotation number associated with each orbit may be either rational or irrational. In the case of a rational rotation number, p/q ($p, q \in \mathbb{Z}$), since the z-axis is invariant under the flow, the orbit will turn q times around the z-axis and p times around the primary periodic orbit before closing in on itself. This resonance phenomenon does not occur when the rotation number is irrational; in this case no point on the torus is revisited in a finite time. The resonance regions are found to be slim tongues which open out smoothly from the secondary Hopf bifurcation, and are bounded by curves of saddle-node bifurcations of periodic orbits (Kirk, 1991). Some of these curves are illustrated in Figure 6.1(b), although since a tongue exists for each rational number p/q, there is a countable number in total. Horseshoes are introduced into the flow, resulting from the heteroclinic crossings of the stable and unstable manifolds of two of the fixed points, and this can lead to chaotic dynamics within the region (Kirk,
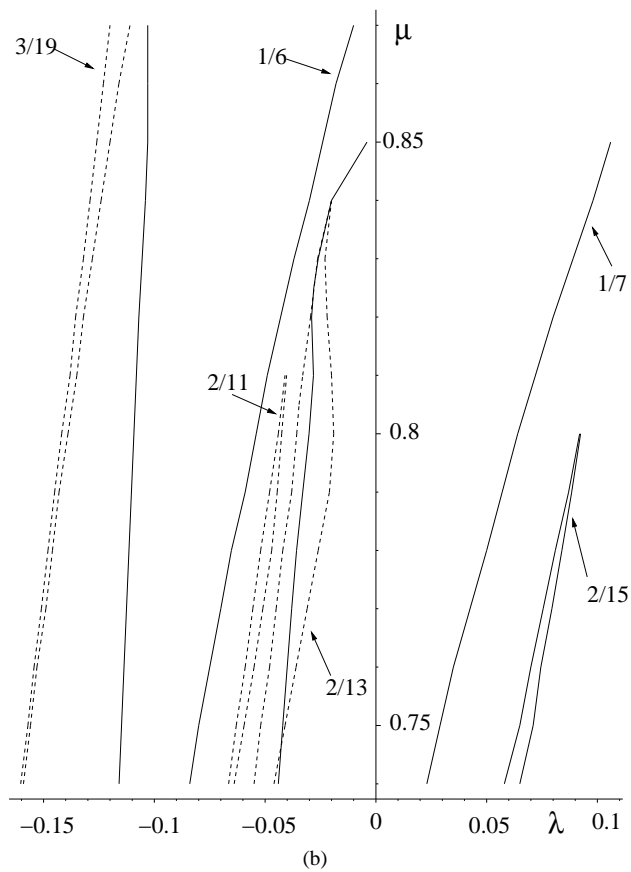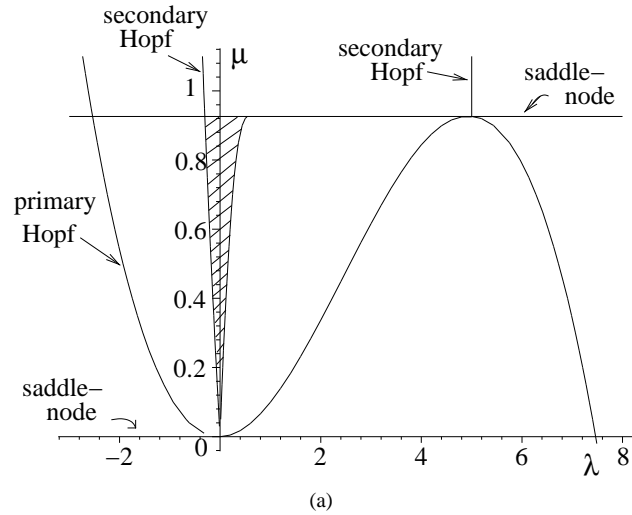
Figure 6.1: Bifurcation curves for Equations (6.3) with $a = 3$, $c = -d = 0.4$, and $\omega = 10.25$. (a) Global bifurcation set (with bifurcations in the shaded region omitted.) (b) Boundaries of some of the resonance tongues, with fractions indicating the order of each resonance.
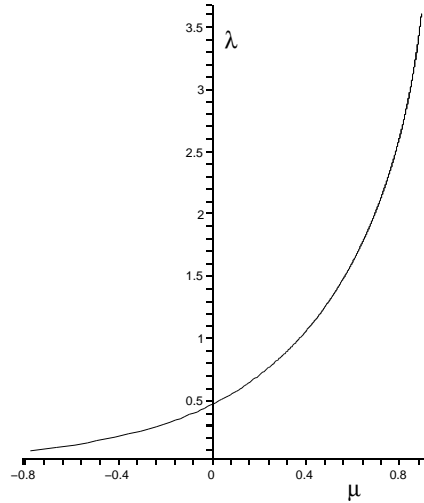
Figure 6.2: The one-parameter path in the λ–μ plane, given by (6.5), along which solutions are examined. The direction of increasing Ω is in the positive y-direction.

1991).

To illustrate the new dynamics, we examine the model's behaviour along a one-parameter path in the λ–μ plane, chosen so that solutions along the path mimic the observed stellar behaviour as rotation rate is increased. We choose the parameterization

$$\mu = \sqrt{\Omega}$$
$$\lambda = \frac{1}{4}\left[\left(\ln\left(\Omega\right) + \frac{3}{2}\right)\exp\left(-\frac{\Omega}{100}\right)\right], \tag{6.5}$$

where $\Omega \in [0, \infty)$. Clearly the path satisfies the requirement $\mu > 0$. It passes through the primary Hopf bifurcation to the left of the μ-axis and then through the heteroclinic region, staying close to the μ-axis (which is where the complicated dynamics occur). The path then tends back to this axis to give stable dynamo action as $\Omega \to \infty$. The path is illustrated in Figure 6.2.

In this section we present the numerical results obtained by integrating the system (6.3) using the Runge-Kutta Fehlberg numeric method in MAPLE. Although we can loosely think of Ω as representing the effects of rotation on the system, we cannot link it directly with any physical parameters such as the Rossby number. As we shall show, the behaviour of the system of equations (6.3) along the parameterized path (6.5) is similar to that found by Tobias et al. (1995).

For small Ω, all trajectories are attracted to one of the fixed points that correspond to purely convecting states. Magnetic instability sets in at $\Omega = 7.69 \times 10^{-3}$ with a primary (supercritical) Hopf bifurcation, so that periodic trajectories are apparent, a typical example of which is shown in Figure 6.3. The radius of the periodic orbit grows as Ω is increased, giving solutions for the magnetic field (represented here by x^2) that grow in amplitude with increasing Ω. The period of oscillation remains approximately constant

(a)

Figure 6.3: Magnetic activity solution for (6.3) as a function of time along the parameterized path (6.5) at $\Omega = 0.1$. A small amplitude oscillation is present, whose amplitude grows as Ω is increased.

throughout, since it is controlled largely by the variable ω, with small perturbations to the period arising from the axisymmetry breaking ter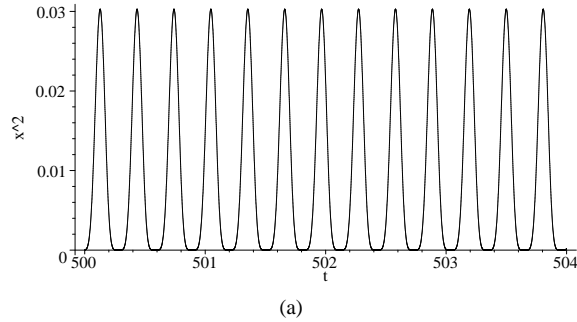m. As the amplitude of the magnetic field grows, the Lorentz force becomes important, varying periodically with half the period of the field, as does the velocity.

At $\Omega = 0.214$ (where $\lambda < 0$), the path crosses the line of the secondary Hopf bifurcation, where a torus bifurcates from the periodic orbit. The solutions for $x(t)$ and $y(t)$, which were periodic before the secondary Hopf bifurcation are now also modulated on a longer timescale, which results in an oscillatory magnetic field with significant amplitude variations in time. At $\Omega = 0.76$, for example, solutions are quasiperiodic, as shown in Figure 6.4 (a,c). Nearby to such quasiperiodic trajectories, the path also moves through various resonance regions, an example of which is shown in Figure 6.4 (b,d) where $\Omega = 0.74$. The solutions for $x(t)$ and $y(t)$ appear to be qualitatively similar but we see that the trajectory winds exactly six times around the z-axis in one period before returning to its original location. Near the frequency-locked regions where the winding numbers are irrational but close to a rational p/q, the orbit can spend most of its time in a phantom periodic orbit from which it occasionally unlocks.

Quasiperiodic solutions do not persist far from the secondary Hopf bifurcation, with the resonance tongues closing off as it is approached. As Ω is increased the torus grows and begins to approach the invariant z-axis. In addition the torus becomes less smooth, with first wrinkles, then folds developing on the attractor. The dynamics are qualitatively unchanged by the saddle-node bifurcation, reached at $\Omega = (0.9\bar{2}5)^2 \approx 0.8573$, although two of the three stationary points that existed until this point are destroyed in the bifurcation. The resonance tongues that are associated with the frequency locking of the flow persist (despite the breakdown of the torus), giving rise to windows of periodicity along the trajectory. The effect of the transition to chaos is best illustrated by taking Poincaré sections through the plane $y = 0$. We show this in Figure 6.5, where the appearance of folds on the section marks a transition to chaos. The modulation of the underlying cycle in the time series for x and y becomes irregular.

The activity cycle, represented here by x^2, shows irregular bursts of activity followed by variable lengths of no activity. The time series for z (which represents the velocity) oscillates between values near to the two stationary points $z = \pm\sqrt{\mu}$. An example is shown in Figure 6.6.

As Ω is further increased an interesting phenomena is observed; solutions with an intermittent character are present, such as that illustrated in Figure 6.7. The time-series for $x(t)$ and $y(t)$ flip between different

(a)   (b)

(c)   (d)
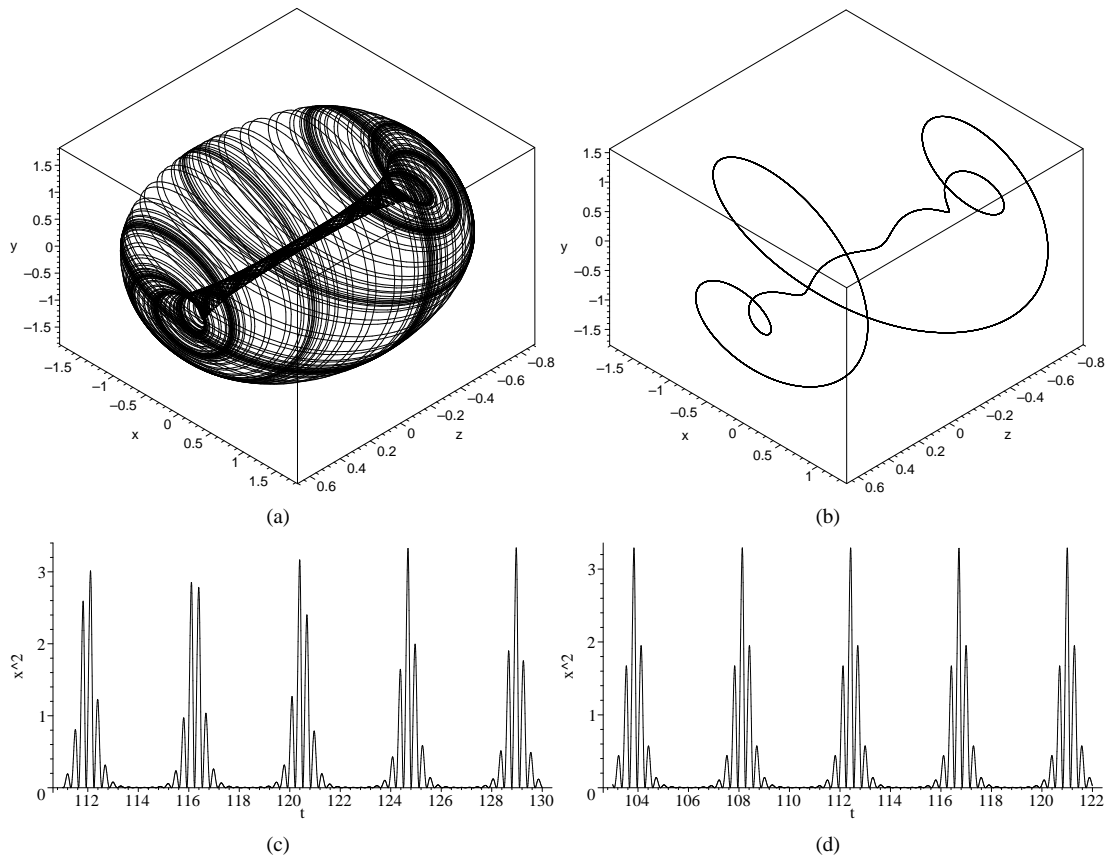
Figure 6.4: Solutions along the parameterized path (6.5). The 3D trajectory plot is shown for (a) the quasiperiodic solutions at $\Omega = 0.76$, and for (b) the frequency locking at $\Omega = 0.74$. The corresponding activity cycles, represented by x^2, are shown, with (c) $\Omega = 0.76$ and (d) $\Omega = 0.74$.

(a)   (b)   (c)
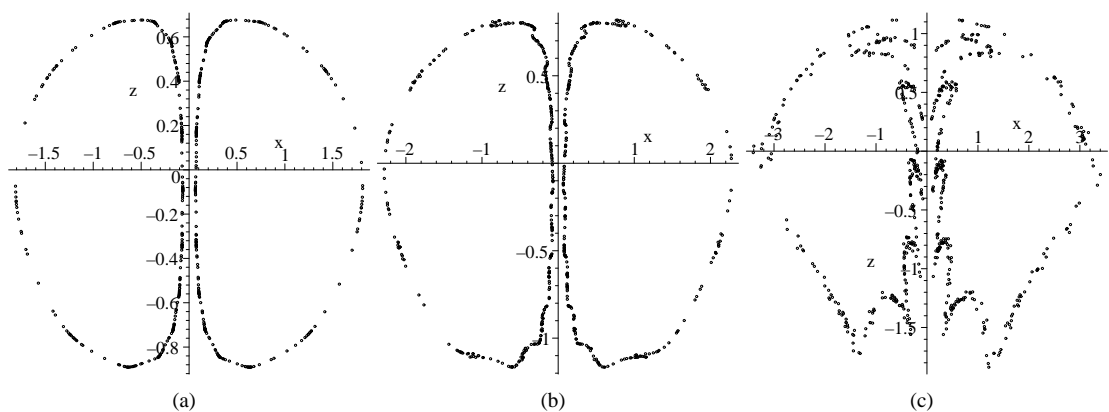
Figure 6.5: Poincaré sections through the plane $y = 0$. (a) At $\Omega = 0.76$ the section is well defined and smooth. (b) At slightly larger values of Ω, wrinkles start to appear on the attractor, illustrated here for $\Omega = 1.68$ (c) The transition to chaos is evidenced by folds appearing on the attractor, shown here for $\Omega = 3.64$.
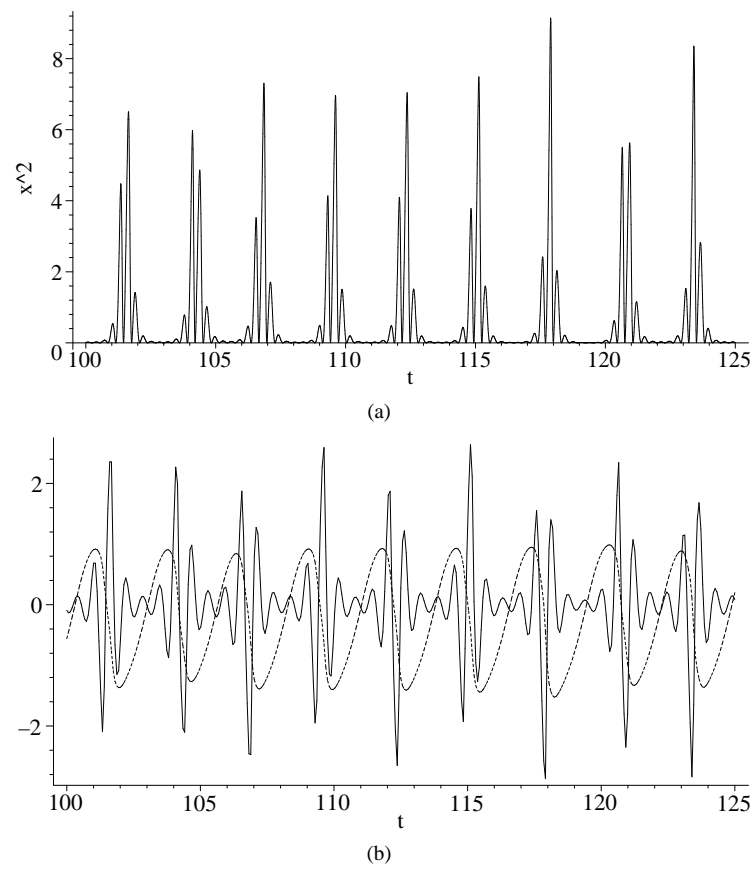
Figure 6.6: Chaotic solutions along the parameterized path (6.5) at $\Omega = 3.64$ showing (a) the activity cycle, characterised by bursts of activity between varying periods of very low activity, and (b) $x(t)$ (solid) and $z(t)$ (dotted).
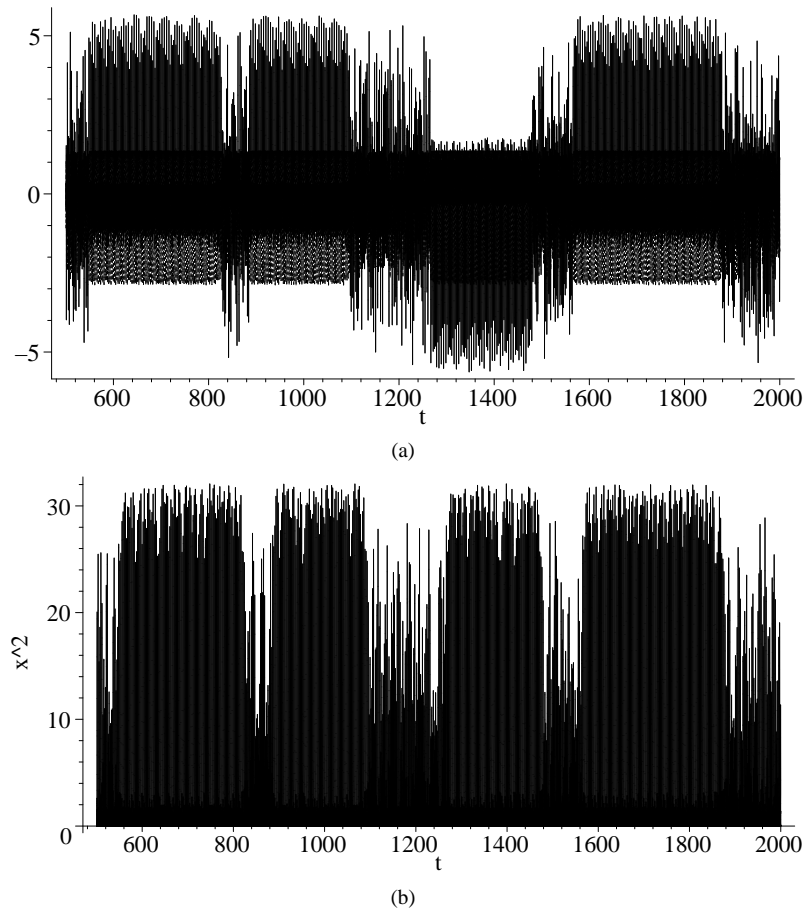
Figure 6.7: Example solutions along the parameterised path at $\Omega = 11.023$, with (a) the time series for $x(t)$ and (b) the resultant magnetic activity cycle. Solutions are found to have an intermittent nature.

states which leads to a magnetic activity cycle with episodes of reduced and enhanced magnetic activity.

6.4   Summary

Our understanding of stellar magnetic activity in solar-like stars and its dependence on parameters such as the Rossby number is deepening through studies such as the H-K project at the Mt Wilson Observatory. The magnetic activity found in this survey divides stars naturally into those with constant emission, periodic emission, irregular emission and long term changes in emission (Baliunas et al., 1995). Younger stars, which rotate relatively rapidly and have higher dynamo numbers, tend to be those with irregular emission, while older slower rotators (which have low dynamo numbers) tend to show periodic or regular emission (Hempelmann et al., 1996).

Stellar dynamos are governed by highly complex non-linear systems of equations, the modelling of which has been approached in a number of ways, from various types of mean field model to elaborate numerical simulations. A partial understanding of the bifurcation structure of such models can be gained

by studying low-order models, consisting of coupled nonlinear ordinary differential equations. Using such a theoretical model one can explore qualitatively the effect of increasing rotation by looking at a system's behaviour in parameter space, for example by increasing the dynamo number. For slow rotators (small dynamo numbers) we would expect to observe a field-free state, with a sequence of bifurcations leading to periodic, quasiperiodic, and finally irregular emission as the dynamo number is increased.

Here we have extended the model of Tobias et al. (1995) to include an axisymmetry-breaking term that maintains the underlying symmetry, $B \rightarrow -B$, that corresponds to reversal of the field. Many of the parameters can be tied loosely to physical effects; however, since the system has not been derived directly from a set of governing equations we cannot relate them directly to physical parameters such as the Rossby number. We have demonstrated that the bifurcation sequence proposed by Tobias et al. (1995) is present in the new system of equations, with solutions going from field-free to periodic, quasiperiodic and chaotic as the forcing parameter is increased. Furthermore we have identified a new type of solution that is characterised by the occurrence of long and deep minima interspersed with increased chaotic activity with clusters of shorter minima.

These results are of interest as they can be related to observations, as discussed above. Moreover the results presented here are robust and so can be related to the bifurcations that are found in more complicated (but less transparent) models based on Partial Differential Equations. Such an analysis of simplified mathematical systems can scientifically complement those numerical studies that attempt to model fully either a particular stellar system, or, at a more ambitious level, solve the full set of magnetohydrodynamic dynamo equations. They can even give a guide as to the types of behaviour to be expected in such systems.

Chapter 7

A Time-Delay Model for Solar and Stellar Dynamos

In this chapter we propose a physically motivated model for solar and stellar dynamos. As with that of the previous chapter, the simple nature of the model allows us to explore a wide range of parameter space. We begin in Section 7.1 by providing a physical motivation to consider delay differential equations in dynamo modelling.

The results of this chapter can be found in Wilmot-Smith et al. (2006b).

7.1   Introduction

Which of the various proposed α-effect mechanism(s) is (are) dominantly at work in stellar interiors such as the solar convection zone is a matter of debate. It is certain however that the various α-effects proposed (see Section 6.1) operate at different layers in the convection zone (Mason et al., 2002) where they may, or may not, spatially coincide with the Ω-effect. The latter, for the Sun, is believed to be primarily in the tachocline layer. For a dynamo mechanism with a spatial segregation of the two source layers for the Ω and α-effects it is clear that there must be an efficient means of communication (through flux transport) between the two distinct source regions (see Figure 7.1 for a discussion on the spatial geometry of the problem). Magnetic buoyancy plays a role in this by transporting strong toroidal flux from the base of the convection zone to the upper layers (i.e., from the Ω-effect layer to the α-effect layer). How the dynamo loop is closed through flux transport from the α-effect layer back to the Ω-effect layer differs from one model to another, based on which α-effect mechanism the model invokes.

For an α-effect operating in the tachocline, which is also the location of the Ω-effect, the spatial co-incidence implies that the communication between the source layers is almost instantaneous, i.e., toroidal field generated by the Ω-effect is immediately available for regenerating the poloidal field. In the interface
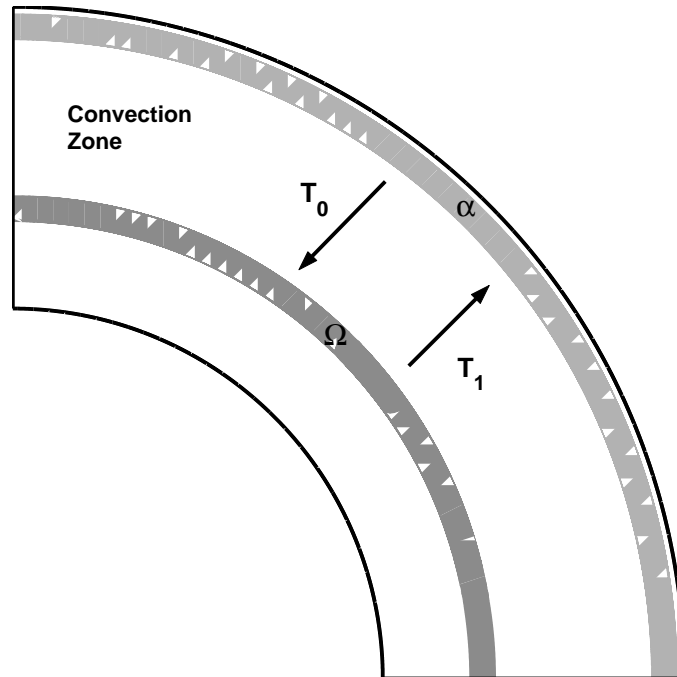
Figure 7.1: A cartoon depicting the concept of flux transport time delays in the interior of a solar-like star. This meridional cut (in the r–θ plane) shows the convection zone and some part of the radiative interior. A region of strong shear in the differential rotation (such as the solar tachocline) is depicted in dark gray – the dynamo Ω-effect (which generates toroidal field from the poloidal component) acts in this layer. The dynamo α-effect (which regenerates poloidal field from the toroidal component) is shown here in light gray and acts in a layer located near the surface; the location of the α-effect layer depends on which physical mechanism is invoked to account for it (see text). For the dynamo to function, communication between the two segregated dynamo source layers should take place via some means of flux transport. This process involves unavoidable time delays. In this paper, the time taken for poloidal flux to be transported from the α-effect layer to the Ω-effect layer and toroidal flux to be transported from the Ω-effect layer to the α-effect layer, are quantified in the time delays T_0 and T_1, respectively.

dynamo (Parker, 1993) – based on the convective α-effect – a negative convective α-effect is located in the convection zone only, below which the Ω-effect operates in the tachocline. A discontinuity in the magnetic diffusivity occurs across the interface between the tachocline and the convection zone. The separation of sites for the generation of poloidal and toroidal field means they interact primarily through diffusion or turbulent flux pumping (Tobias et al., 2001) – which is the primary transporter of flux from the α-effect layer in the convection zone back to the Ω-effect in the tachocline. The same spatial physical structure characterises dynamos based on an α-effect due to buoyancy instabilities and located just above the tachocline or in the base of the convection zone (Ferriz-Mas et al., 1994). A larger segregation of the two source layers differentiates the spatial physical structure of the Babcock-Leighton mechanism, where a positive α-effect acts in the surface layers. In this case it is advective flux transport by meridional circulation (see Nandy, 2004, for a review) and to some extent turbulent pumping, that transports the surface poloidal flux to the tachocline where the Ω-effect resides. An unavoidable time-delay – due to the finite time required to transport magnetic flux from one source region to another – materializes in those dynamo models that have physically distinct source layers. In this chapter, we aim to explore the role of this time-delay in solar and

stellar dynamo activity.

The removal of all spatial dependence in low-order ODE models' description of the field evolution gives an implied instantaneous communication between the two field components (toroidal and poloidal) that would not occur in spatially segregated models. The introduction of certain time delays in a system of ODEs, so converting them to a set of delay differential equations (DDEs), can take account of such a spatial segregation. Indeed time-delays are intrinsic to PDE models that include meridional circulation, since this circulation effectively introduces a delay that is comparable to the cycle period.

The notion of time-delay has earlier been studied in the context of a finite delay in the feedback of the magnetic fields on the dynamo source terms (Yoshimura, 1978). Time delay dynamics have also been examined in the specific case of the Babcock-Leighton model via the use of one-dimensional iterative maps (Durney, 2000, Charbonneau, 2001) that include the long time delay between the production of toroidal field from poloidal field, but ignore dissipative effects. Results have been shown to be in good agreement with spatially extended numerical models (Charbonneau et al., 2005). Thus, in addition to stochastic forcing and dynamical nonlinearity, the possibility arises that observed irregularities in solar and stellar cycles may result from the effect of time delays in the underlying physical processes that generate these cycles.

In this chapter we introduce time-delays into a set of truncated dynamo equations, thereby constructing a time-delayed system that includes both dissipative effects (which are absent in 1D iterative maps), and a delay in both the conversion processes (from toroidal to poloidal component and vice-versa). The underlying physical mechanism remains relatively transparent and can, in general, be applied to study dynamo models based on a diverse set of α-effect mechanisms. In this model, a low or vanishing time-delay physically resembles a scenario in which the dynamo α-effect and Ω-effect are spatially coincident. Finite time delays properly account for the two-layer character of dynamos based on spatially segregated source regions and the role that magnetic flux transport (e.g., mediated via meridional circulation or magnetic buoyancy) plays in these models. It is shown that the introduction of time delays can have a considerable effect on the dynamics and lead to significant fluctuations in cycle amplitude.

We begin in Section 7.2 by deriving the model before examining its behaviour in two important parameter regimes in Section 7.3. One regime is that for which the time delay is smaller than the dissipative timescale. We characterise solutions in this regime, where the effect of the time-delays dominates over that of dissipation, as *flux transport dominated*, and find that relatively regular activity identifies these solutions. The case where the time delay is larger than the dissipative timescale is characterised as the *diffusion dominated* regime, and we find irregular activity is more easily excited in this case. We discuss the implications of our results for solar and stellar dynamos and summarize the results in Sections 7.4 and 7.5.
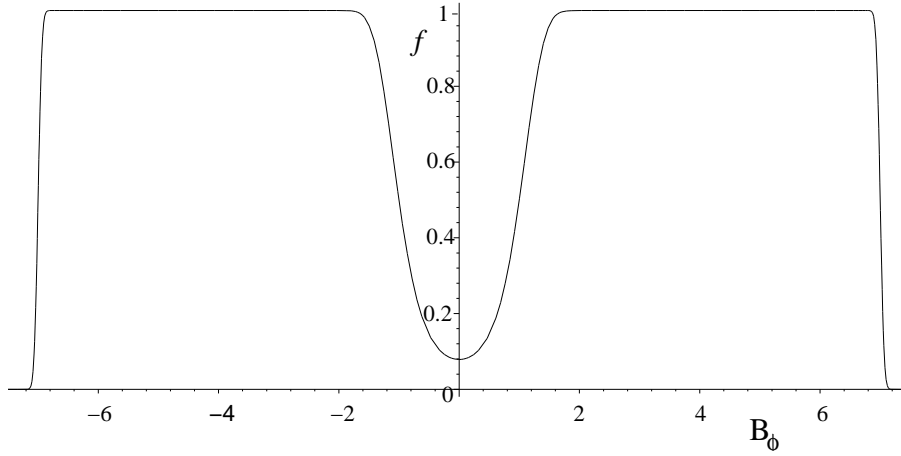
Figure 7.2: Dependence of the quenching factor, f ($f = \alpha/\alpha_0$), on toroidal field strength, for the parameters $B_{min} = 1$, $B_{max} = 7$.

7.2   Model Setup

Considering only the source and dissipative processes in the dynamo mechanism and through a truncation via removal of all spatial dependence, we obtain the equations

$$\frac{dB_\phi}{dt} = \frac{\omega}{L}A - \frac{B_\phi}{\tau_\phi},$$

$$\frac{dA}{dt} = \alpha B_\phi - \frac{A}{\tau_p},$$

where B_ϕ represents the toroidal field and A the poloidal field. In this simplest possible case the evolution of each component is a result of the combination of a source process (first term on the R.H.S. of the above equations) and a diffusive process (second term on the R.H.S.). For the toroidal field the source process is a conversion from the poloidal field (the Ω-effect), dependent on the differential rotation ω (not to be confused with the rotation rate), and the length scale over which it acts, L (the length of the tachocline, for example). Diffusion of the field itself, occurring through ohmic decay, is parameterised by τ_ϕ – which represents the diffusion timescale for the toroidal field. The evolution of the poloidal field is also a combination of two similar actions; diffusion, with τ_p representing the diffusion timescale for the poloidal field, and a source in the conversion from toroidal field via the α-effect.

To account for alpha-quenching we take a general form for α given by $\alpha = \alpha_0 f$, where α_0 is the amplitude of the α-effect and f is the quenching factor approximated here by the non-linear function

$$f = \frac{[1 + \mathrm{erf}(B_\phi^2(t) - B_{min}^2)][1 - \mathrm{erf}(B_\phi^2(t) - B_{max}^2)]}{4}. \tag{7.1}$$

Figure 7.2 illustrates a typical profile for f. The form for f has been chosen such that the function α that represents the alpha-effect has an upper threshold limit (related to B_{max}) above which $\alpha = 0$ and, similarly, a lower threshold limit (related to B_{min}) below which $\alpha = 0$. The motivation for the including

a possible lower operating limit, B_{min}, comes from the suggestion of a critical threshold in the toroidal field in stellar interiors over which toroidal flux ropes become magnetically buoyant and rise up into the alpha-effect source region (Durney, 1995). This lower threshold due to magnetic buoyancy limits field strengths and has been shown to play a crucial role in determining the amplitude of dynamo activity (Nandy, 2002). An upper limit to the field strengths on which the alpha-effect operates is, in mean-field models, associated with *alpha-quenching* where the Lorentz force associated with strong toroidal fields impedes the small-scale helical turbulent motions. In the Babcock-Leighton mechanism the upper limit stems from the ineffectiveness of the Coriolis force on strong toroidal flux tubes. Simulations of rising flux tubes suggest that tubes with strength greater than around $100kG$ will rise to the solar surface without the tilt crucial in imparting the poloidal field (D'Silva and Choudhuri, 1993, Fan et al., 1994). The exact form chosen for f is arbitrary (just as is the algebraic form for alpha-quenching in traditional mean-field models of the solar cycle). We discuss in Section 7.4 the implications of making different choices.

In a dynamo with spatially segregated source regions, communication between the two layers would not be instantaneous as in the above equations. To take account of this, two physically motivated distinct time delays are introduced into the equations; the first being a time delay for the conversion of poloidal field into toroidal field, T_0, and the second a time delay for the conversion of toroidal field into poloidal field, T_1 (see Figure 7.1). Time delays will appear in all conversion processes, and so the equations become

$$\frac{dB_\phi(t)}{dt} = \frac{\omega}{L}A(t - T_0) - \frac{B_\phi(t)}{\tau_\phi}, \tag{7.2}$$

$$\frac{dA(t)}{dt} = \alpha_0 f(B_\phi(t - T_1)) B_\phi(t - T_1) - \frac{A(t)}{\tau_p}. \tag{7.3}$$

Thus a system of two coupled DDEs has been obtained to describe the dynamo, with the only nonlinearity being the parameterisation of the source term for the poloidal field. The time delays signify that the generation of any component of the magnetic field (on the L.H.S. of the above equations), at a given instant in time, is dependent on the magnitude of the other component of the magnetic field (appearing in the first term on the R.H.S.) at an earlier time – corresponding to the time delay. Thus, this system of DDEs has an in-built memory mechanism capable of "remembering" the values of magnetic fields from an earlier time equal to the time delays. We show in Section 7.3 that growing solutions to these equations are possible.

The time delay T_0 accounts for the time taken for a poloidal flux tube to be transported from the site of its production back to the tachocline. In the Babcock-Leighton mechanism the meridional circulation advects surface poloidal field back to the the tachocline (which, from mid-latitudes at the surface to mid-latitudes at the tachocline, takes on the order of 10 years). Often invoked in the high magnetic Reynolds number (R_m) regime, this class of advection-dominated models assumes that there are negligible dissipative losses during this transport. The meridional circulation then governs T_0 in Babcock-Leighton models. We might expect the delay to be shorter in the interface dynamo (with downward flux transport accomplished by turbulent flux pumping – which again has negligible dissipative effects during transport), particularly if the α-effect is deep-seated. The time delay should be vanishingly small for spatially coincident source layers (with both the Ω and α-effects in the tachocline, for example). Note that to some extent, poloidal flux can be brought down to the Ω-effect layer through simple spatial diffusion (as opposed to other mechanisms, this also destroys the flux during transport). If indeed the spatial diffusive transport is faster and more efficient

than all other means of transport, then T_0 should correspond to the spatial diffusion timescale and one has to account for dissipation during flux transport (see Section 7.4 for a discussion on this). The important point to remember is that, if there are competing mechanisms for flux transport, the one with the shortest timescale should be the governing one (as this would be most efficient).

The time delay T_1 accounts for the time taken for a toroidal flux tube to buoyantly rise to the site of poloidal field production. The timescale for the buoyant rise of a flux rope from the interior to the photosphere is rather short, being of the order of three months, and so $T_1 \ll T_0$. However, $T_{0,1} \neq 0$ in any model for which there is a spatial segregation between the two layers.

The diffusion timescales for the poloidal and toroidal field are given by

$$\tau_p = \frac{L_{SCZ}^2}{\eta_p}, \quad \tau_\phi = \frac{L_{SCZ}^2}{\eta_\phi},$$

where L_{SCZ} is the width of the solar convection zone (in general, it should be the separation of the two source layers); $L_{SCZ} = 0.3R_\odot \sim 2.1 \times 10^8$m. If we take the toroidal diffusivity, η_ϕ to be equal to the poloidal diffusivity, η_p, then $\eta_\phi = \eta_p \sim 10^{12}$ cm^{2}s^{-1} a widely accepted value, and so $\tau_{p,\phi} \sim 13.8$ years. Alternatively, due to the strong, coherent nature of the solar toroidal magnetic field that can suppress the magnetic diffusivity by as much as two orders of magnitude, we might have $\eta_\phi < \eta_p$ (for a discussion see Chatterjee et al., 2004), so increasing τ_ϕ to $\tau_\phi \sim 1380$ years.

Given the simplified nature of the model, the use of solar parameter values in the system would not be helpful in any attempt to quantify dynamics. Rather, the brief discussion of their values is intended to provide an indication of the comparative magnitudes of the terms, which is shown later to be critical in determining dynamics.

As an aid to understanding the underlying structure of the model, we can reduce the system (7.2, 7.3) to a single second-order equation for B_ϕ by differentiating (7.2) and substituting (7.3) for $dA(t - T_0)/dt$ (note the evaluation at the delayed time $(t - T_0)$). This, among others, generates a term proportional to $A(t - T_0)$ which in turn is substituted for by (7.2). The resulting equation is

$$\frac{d^2 B_\phi}{dt^2} + \left(\frac{1}{\tau_\phi} + \frac{1}{\tau_p} \right) \frac{dB_\phi}{dt} + \frac{1}{\tau_p \tau_\phi} B_\phi = \frac{\alpha_0 \omega}{L} f\left(B_\phi \left(t - T_0 - T_1 \right) \right) B_\phi \left(t - T_0 - T_1 \right), \qquad (7.4)$$

which can be supplemented by (7.2) for the solution of $A(t)$. The system (7.2, 7.4) is equivalent to (7.2, 7.3) and therefore has the same set of solutions.

The time delays T_0 and T_1 appear in (7.4) as a sum, so it appears to be their sum that is important in determining the dynamics. If the right-hand side of (7.4) is set to zero the equation becomes that of a damped oscillator. In the case where $\tau_p = \tau_\phi$ the oscillator is critically damped, while in all other cases it is over-damped. Thus, for toroidal field strengths outside of the range where f is non-zero, we might expect the system to behave as a damped oscillator. For toroidal field strengths within the range where f is non-zero, the term on the right-hand side of (7.4) is important. We will show in Section 7.3 that some analogies of the full system with a damped driven oscillator can be made.

To examine solutions to this system we numerically integrate the equations, basing the code on the NDelayDSolve.m package in Mathematica. An initial solution to the problem in the range $t \in [-T_{max}, 0]$ is specified, where $T_{max} = \max\{T_0, T_1\}$. The effect of various initial conditions is discussed as the solutions are presented.

The model is relatively simple, but gives rise to a wide range of dynamic behaviour. Here some parameter regimes are examined which suffice to illustrate the complexity the system is capable of displaying and its relevance to our understanding of solar and stellar dynamos. From (7.4) the sum of the two time delays is expected to be important in determining the dynamics. Therefore, we examine two extreme cases in particular. One case is where $\tau_{p,\phi} \gg T_0 + T_1$, which we call the flux transport dominated regime and consider in Section 7.3.1. The case $\tau_{p,\phi} \ll T_0 + T_1$, is called the diffusion dominated regime and is considered in Section 7.3.2. In both of these regimes we will consider solutions for positive and negative dynamo number, N_D (which is related to the Rossby number as $N_D \propto 1/R_o^2$) (Durney and Latour, 1978). In particular we will consider the effect of increasing $|N_D|$ since from stellar observations a change in the dynamics is expected across a parameter space covering a range of N_D (and consequently R_o) values.

7.3   Results

Setting $T_0 = T_1 = 0$ in equations (7.2) and (7.3) corresponds to a dynamo model in which there is no time delay in the magnetic flux transport between the two source regions (a situation that could result when the source regions are spatially coincident and there is no time delay involved in the α-quenching mechanism via the Lorentz feedback). In this two-dimensional system, when the condition $\tau_p, \tau_\phi > 0$ is applied, we obtain only two qualitatively different solutions; either A and B_ϕ both decay to zero, or they are both attracted to a non-zero fixed point of the system. These fixed points are given by solutions, $A(t) = a$, $B_\phi(t) = b$, such that $f(b) = L/(\alpha_0 \omega \tau_\phi \tau_p)$ and $a = Lb/\omega\tau_\phi$. Thus the solutions described in the following sections all arise from the inclusion of time delays in the model. We note that in the linear analysis of the dynamo equations Parker (1955) found wave-type solutions when the spatial derivatives are explicitly accounted for. The time delays we will introduce later compensate for the information lost by simplifying the spatial terms as we have above.

When at least one of the time delays is non-zero, oscillatory solutions to the system may be obtained. In the solar case the strength of the toroidal field is much greater than the poloidal field. This can always be reproduced for non-zero solutions by taking $|\omega_0/L| > |\alpha_0|$. Although $\langle B_\phi \rangle > \langle A \rangle$ may also be achieved in some parameter regimes with $|\omega_0/L| < |\alpha_0|$, these cases are more limited. The parameters B_{min} and B_{max} will be fixed throughout as $B_{min} = 1$, $B_{max} = 7$. Qualitatively similar solutions to those outlined below can be attained with different particular values of B_{min} and B_{max}; see Section 7.4 for a further discussion of this point.

7.3.1 Flux Transport Dominated Regime

Solutions obtained in the regime where the diffusion timescales are large compared to the time delays ($\tau_p, \tau_\phi > T_0 + T_1$) are examined in this section. Physically, this scenario means that the flux transport (mediated by either, or the collective action of, meridional circulation, magnetic buoyancy and turbulent flux pumping) occurs efficiently and within a duration of time over which dissipative effects are not important.

In this model the dynamo number is given by $N_D = \alpha_0 \omega \tau_p \tau_\phi / L$. We begin by examining solutions for $N_D < 0$, taking $\omega < 0$, $\alpha_0 > 0$, and take a sequence of increasing absolute value of dynamo number N_D (and therefore decreasing Rossby number R_o). This corresponds to increasing the rotation rate of the star. The cut through parameter space given by $\omega/L + 2\alpha_0 = 0$ is taken, so that the relative strength of the source terms for poloidal- and toroidal-field production remain the same, and all other parameters are fixed as

$$\tau_\phi = 15, \ \tau_p = 15, \ B_{min} = 1, \ B_{max} = 7, \ T_0 = 2, \ T_1 = 0.5, \ \text{and} \ \omega/L + 2\alpha_0 = 0.$$

The initial solutions are specified as the constant $(B_{min} + B_{max})/2$ for both A and B_ϕ.

On this sequence a periodic orbit bifurcates from the fixed point at the origin when $N_D = -12.696$. The orbit then becomes periodically modulated, so that B_ϕ and A both show oscillatory behaviour, with amplitudes modulated on a longer timescale. The amplitude of modulation increases along the parameter path, but B_ϕ lies within the range $[-B_{max}, B_{max}]$ for all time. An example is shown in Figure 7.3, where $N_D = -13.01$. For $N_D < -17.11$ solutions for B_ϕ are no longer contained within the range $[-B_{max}, B_{max}]$. Solutions are now periodic, with both A and B_ϕ showing cyclic behaviour, with a constant period and amplitude, a typical example of which is illustrated in Figure 7.4. The rising phase of both solutions is steeper than the declining phase, and a sharp change in the first derivatives of both A and B_ϕ can be seen during each declining phase.

Both the period and amplitude of the oscillation increase with increasing $|N_D|$, as shown in Figure 7.5. There is a linear dependence of amplitude on dynamo number over several orders of magnitude, while the period of the cycle varies logarithmically. As is evident from Figure 7.6, an increase in the sum $T_0 + T_1$ also increases both the periods and amplitudes. Solutions remain qualitatively the same as those illustrated in Figure 7.3 until $T_0 + T_1 \sim 50$.

Next we consider solutions for positive dynamo number, $N_D > 0$. Again periodic solutions to the system can be obtained, but there are important distinctions to be made from the case $N_D < 0$. On increasing the dynamo number the first bifurcation leads to periodic solutions in which both $A(t)$ and $B_\phi(t)$ are of single sign only, and $B_\phi(t)$ is not contained within the range $[-B_{max}, B_{max}]$. A typical example is illustrated in Figure 7.7. The characteristic steep rising phase of the cycle and slower declining phase remain, as does the sharp change in derivative of A and B_ϕ at the end of each declining phase. The same qualitative dependence of cycle amplitude and period on both total time delay and $|N_D|$ as that for $N_D < 0$ is recovered.

Some analogies of solutions in this regime to a damped driven oscillator can be made to help explain

Figure 7.3: Time series, in the flux transport dominated regime, for (*top*) the poloidal field, (*middle*) the toroidal field, and (*bottom*) the magnetic activity (energy), B_ϕ^2, for dynamo number $N_D = -13.01$ and the parameters $\tau_\phi = 15$, $\tau_p = 15$, $B_{min} = 1$, $B_{max} = 7$, $T_0 = 2$, $T_1 = 0.5$, $\omega/L = -0.34$, and $\alpha_0 = 0.17$.
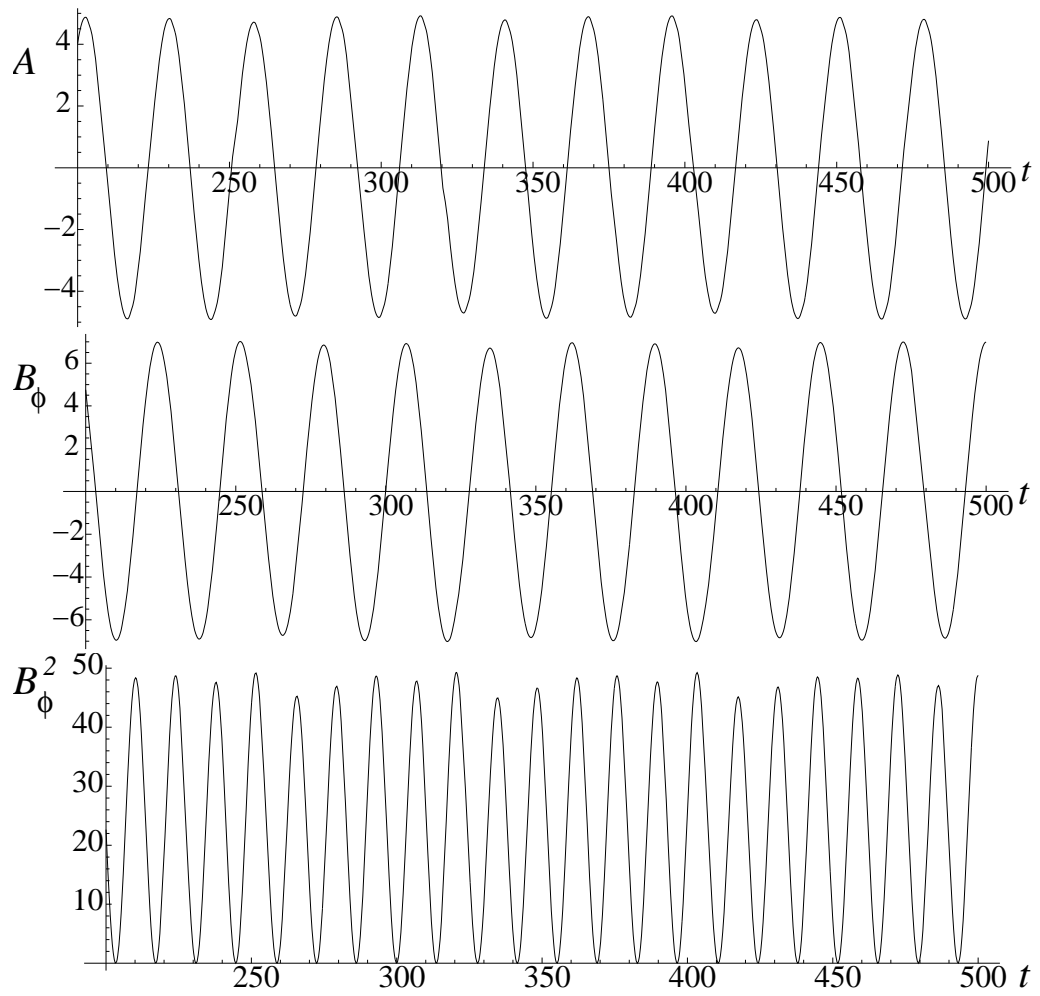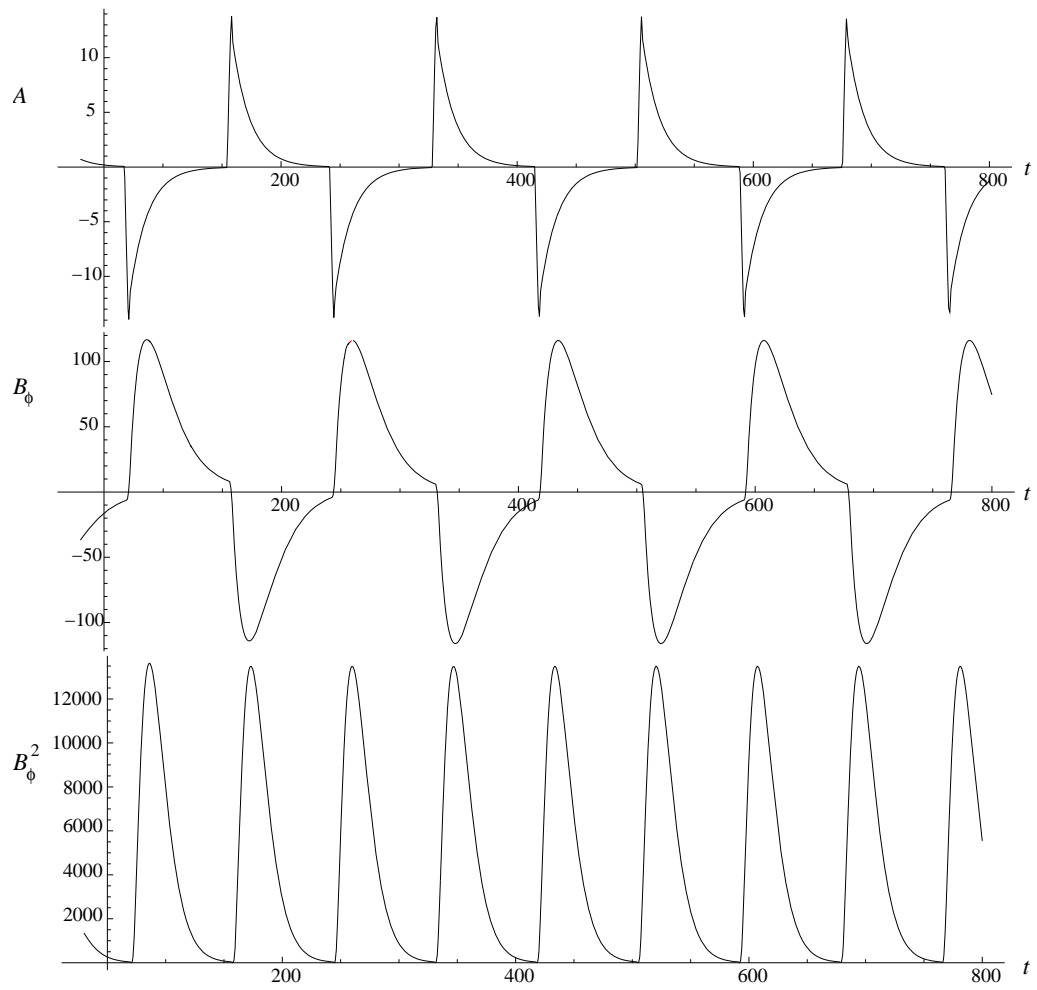
Figure 7.4: Typical time series for $N_D < 0$ in the flux transport dominated regime for (*top*) the poloidal field, (*middle*) the toroidal field, and (*bottom*) the magnetic activity. Here the parameters $\frac{\omega}{L} = -1.5$, $\alpha_0 = 0.75$, $B_{min} = 1$, $B_{max} = 7$, $\tau_\phi = 15$, $\tau_p = 15$, $T_0 = 2$, and $T_1 = 1/2$ have been used.
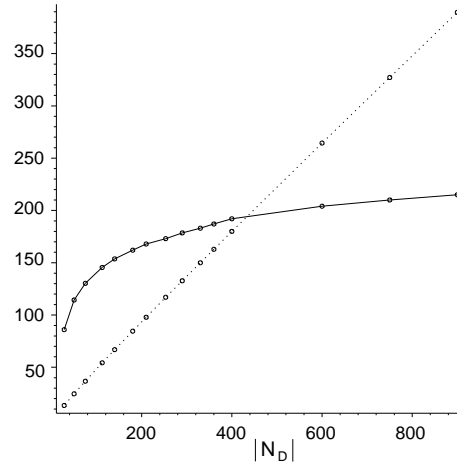
Figure 7.5: Change of cycle period (solid line) and amplitude (dashed line) with the magnitude of the dynamo number, $|N_D|$, in the flux transport dominated regime for $N_D < 0$. The parameters are $\tau_\phi = 15$, $\tau_p = 15$, $B_{min} = 1$, $B_{max} = 7$, $T_0 = 2$, $T_1 = 0.5$ and $\omega/L + 2\alpha_0 = 0$.
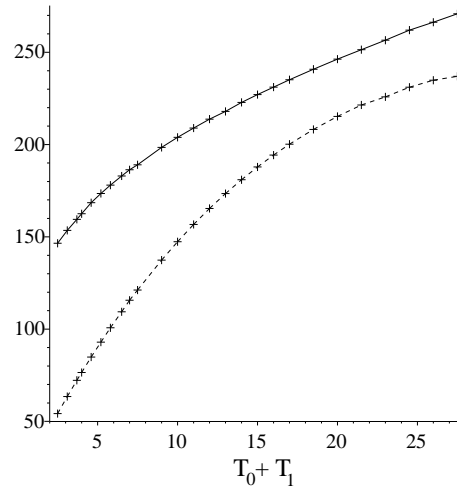
Figure 7.6: Change of cycle period (solid line) and amplitudes (dashed line) with time delay $T_0 + T_1$, in the flux transport dominated regime for $N_D < 0$. The parameters are $\tau_\phi = 15$, $\tau_p = 15$, $B_{min} = 1$, $B_{max} = 7, \omega/L = -1$, $\alpha_0 = 0.5$ and $T_0 = 4T_1$.
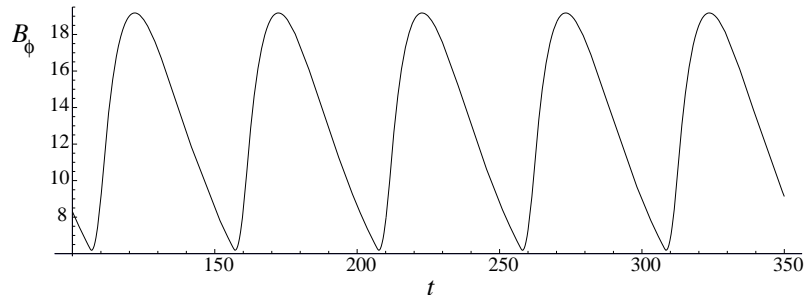
Figure 7.7: Typical time series for the toroidal field for $N_D > 0$ in the flux transport dominated regime. The parameters $\frac{\omega}{L} = -0.5$, $\alpha_0 = -0.2$, $B_{min} = 1$, $B_{max} = 7$, $\tau_\phi = 15$, $\tau_p = 15$, $T_0 = 2$, and $T_1 = 1/2$ have been used, and the initial solution $B_\phi(t) = -5$, $A(t) = -5$ over the range $t \in [-2.5, 0]$ taken.

these properties. Recall that a driven oscillator with periodic driving force can be described by the equation

$$\frac{d^2x}{dt^2} + \frac{b}{m}\frac{dx}{dt} + \frac{k}{m}x = -\beta\cos\left(\Omega t\right),$$

(where $\beta > 0$), which has the steady state solution

$$x(t) = \frac{\beta}{\sqrt{\frac{b^2\Omega^2}{m^2} + \left(\frac{k}{m} - \Omega^2\right)^2}}\cos\left(\Omega t + \Phi\right),$$

where Φ represents the phase shift and is given by

$$\Phi = \operatorname{arccot}\left(\frac{\Omega^2 m - k}{\Omega b}\right). \tag{7.5}$$

The non-zero time lags mean that the right-hand side of equation (7.4) is out of phase with the solution. Thus, this term acts as a driver to the system while $B_\phi(t - T_0 - T_1)$ is within the range $[-B_{max}, B_{max}]$, which we call the *forcing region*.

For negative dynamo number, along the sequence of increasing $|N_D|$, the first bifurcation results in a periodic solution contained entirely within the range $[-B_{max}, B_{max}]$. Thus for this solution $f \sim 1$ and $B_\phi(t) = B_0\cos(\Omega t)$. If $f = 1$ in (7.4), taking $\tau_p = \tau_\phi = \tau$ and assuming the driver acts purely sinusoidally as $B_0\cos(\Omega(t - T_d))$ where $T_d = T_0 + T_1$, we have

$$B_\phi(t) = \frac{-N_D B_0}{1 + \Omega^2\tau^2}\cos\left(\Omega\left(t - T_d\right) + \operatorname{arccot}\left(\frac{\Omega^2\tau - \frac{1}{\tau}}{2\Omega}\right)\right).$$

This expression must be equivalent to our assumption, $B_\phi(t) = B_0\cos(\Omega t)$, and so equating the two expressions gives

$$\Omega T_d = \operatorname{arccot}\left(\frac{\Omega^2\tau - \frac{1}{\tau}}{2\Omega}\right), \tag{7.6}$$

$$\frac{-N_D}{(1 + \Omega^2\tau^2)} = 1, \tag{7.7}$$

We may use this equivalence to explain the value at which the periodic orbit bifurcates from the fixed point and also the frequency of the resultant oscillation. For the parameter values used above, $T_d = 2.5$, $\tau = 15$, equation (7.6) implies $\Omega = 0.228$, for which the corresponding oscillation period is $P = 27.58$. Given this value for Ω, N_D can be deduced from equation (7.7) as $N_D = -12.67$. These values correspond closely to the bifurcation value found in the simulations of $N_D = -12.696$, for which the simulated period was $P = 27.54$. Since $\cos\left(\Omega t + \Phi\right) = -\cos\left(\Omega t + \Phi + \pi/2\right)$ we might also expect to obtain periodic solutions for $N_D > 1$. Instead, growing solutions are found and indeed, for $f = 1$, there exist solutions to equation (7.4) of the form $B_\phi(t) \sim \exp(\lambda t)$ with real $\lambda > 0$ precisely when $N_D > 1$.

When the dynamo number is sufficiently high that solutions are no longer contained within the range $[-B_{max}, B_{max}]$, the analogy with the driven oscillator may still be used, now with the driver acting only intermittently on the solution. Qualitatively, the cycle may be described as follows. The driver starts acting on the system at a time $T_0 + T_1$ after the solution $B_\phi(t)$ enters the forcing region, and continues to act until

a time $T_0 + T_1$ after the solution $B_\phi(t)$ has left the forcing region. This corresponds to the steep rising phase of the cycle. After this time the term on the right-hand side of equation (7.4) is zero and it becomes that of a damped oscillator. After reaching a maximum in its absolute value the solution then decays, until $B_\phi(t - T_0 - T_1)$ again enters the forcing region, where a sudden change in the gradient of $B_\phi(t)$ occurs as the driver again starts to act on the system.

The sign of the term on the right-hand side of equation (7.4) determines the nature of the driving. If this term has negative sign when it acts on the system then the solution will be driven in the $-B_\phi$ direction, whereas if the term has positive sign then the solution will be driven in the $+B_\phi$ direction. The lengthly diffusive time-scales when compared to the time-delays ensure $B_\phi(t - T_0 - T_1)$ is of the same sign as $B_\phi(t)$ when $B_\phi(t)$ decays to $\pm B_{max}$. Thus, if $N_D < 0$ the solution is forced in the same direction as the decay, and a change in the sign of solution occurs. If $N_D > 0$ then the solution is forced against the direction of decay, and the resulting solutions are of single sign only.

This mechanism predicts an increase in the amplitude of the cycle if, for example, the strength of the driving is increased, or if the driving term acts on the system for a greater length of time. An increase in dynamo number $|N_D|$ by keeping $\tau_{p,\phi}$ fixed and increasing both α_0 and ω/L has the effect of increasing the amplitude of the forcing, since the term on the right-hand side of (7.4) depends upon the product $\alpha_0\omega/L$. Over several orders of magnitude, as shown in Figure 7.5, there is a linear relationship between the cycle amplitude and the product $\alpha_0\omega/L$. Letting $\tau_p = \tau_\phi = \tau$ say, using (7.4) we expect the decay to be governed by $\exp\left(-t/\tau\right)$. Thus, with greater amplitude it will take a longer time for the system to decay and re-enter the forcing region. This timescale agrees closely with values found in the simulations, and predicts a period increasing logarithmically with amplitude, as is seen in Figure 7.5. The length of time the driving term acts on the system will depend on the sum of the time delays, since the driving term acts on the system until a time $T_0 + T_1$ after the solution $B_\phi(t)$ has left the forcing region. Thus an increase in the sum of the time delays also increases the amplitude of oscillation, as shown in Figure 7.6, and accordingly the period of oscillation.

It is worthwhile here to compare the behaviour of this time-delayed system with numerical simulations of spatially extended solar dynamo models with realistic internal rotation profiles; specifically, those Babcock-Leighton models in which meridional circulation acts as a transporter of flux between the two source regions. If the circulation is fast (and so the time delay small) the dynamo is more efficient and its period is smaller. Conversely, if the circulation is slow (and time delay large), the period is higher (see Hathaway et al. (2003) for solar observations which support this argument, and Nandy (2004) for a review on the role of meridional circulation in determining the period and amplitude of such dynamo models). Also, for slow circulation speeds (corresponding to large time delays in our model), although subject to the condition that the circulation timescale is still shorter than the diffusion timescale, since magnetic fields stay in the source regions for a longer time, the inductive effect results in higher amplitudes, in agreement with the results of our time-delayed system.
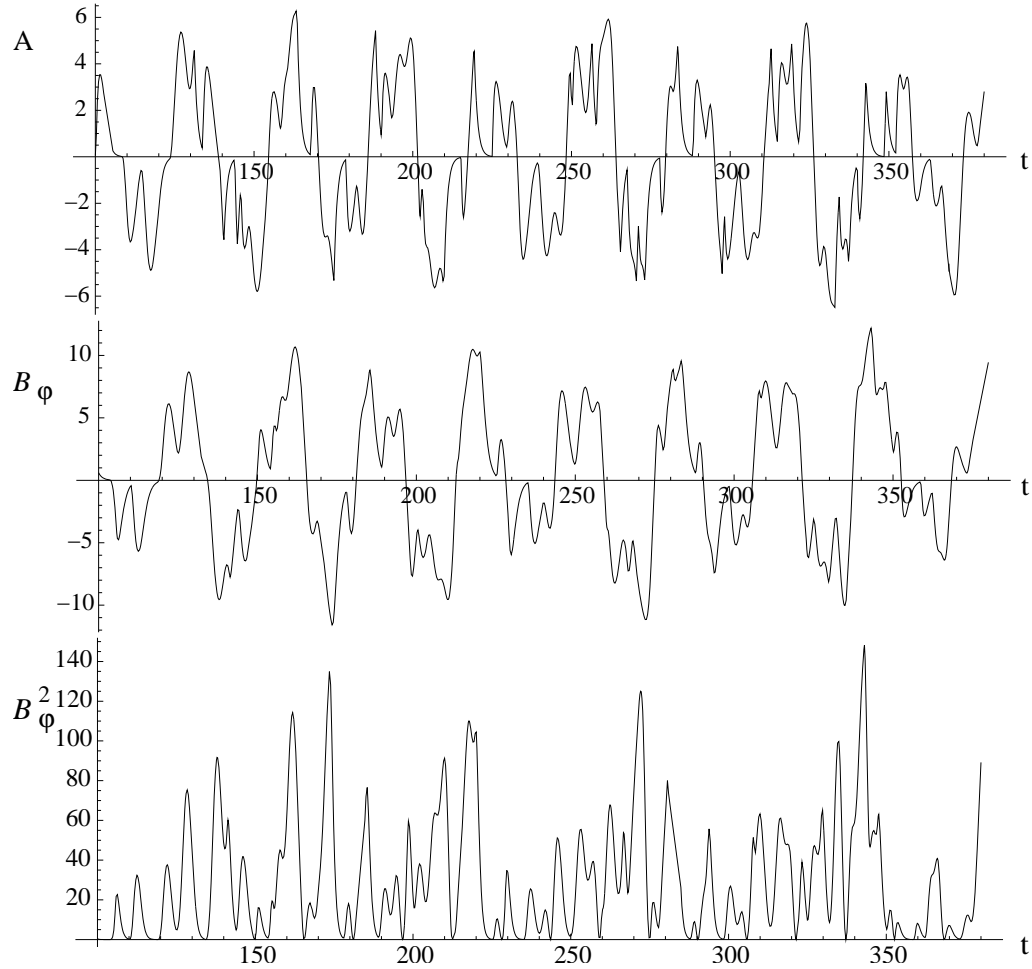
Figure 7.8: Diffusion dominated regime time-series with $N_D < 0$ for (*top*) the poloidal field, (*middle*) the toroidal field, and (*bottom*) the magnetic activity, and the parameters $\frac{\omega}{L} = -2$, $\alpha_0 = 1$ and $\tau_p = \tau_\phi = 1$, $T_0 = 10$, $T_1 = 4$.

7.3.2   Diffusion Dominated Regime

Solutions for which the diffusion timescales are smaller than time delays ($\tau_p, \tau_\phi \ll T_0 + T_1$) are discussed in this section. Physically, this corresponds to a scenario in which significant (ohmic) dissipation alters the magnitude of the fields on a timescale comparable to the flux transport between the source regions.

A wide variety of dynamics occur in this case. Again we begin by examining solutions for which $N_D < 0$. To illustrate some of these we fix the parameters $\tau_p = \tau_\phi = 1$, $T_0 = 10$, $T_1 = 4$ and examine a sequence of increasing absolute value of dynamo number, N_D (with values of B_{min} and B_{max} unchanged). Again the cut through parameter space given by $\omega/L + 2\alpha_0 = 0$ is taken, so that the relative strength of the source terms for poloidal and toroidal field production remain the same. The initial solution is taken as the constant $(B_{min} + B_{max})/2$ for both A and B_ϕ.

For all initial conditions with $-1 < N_D < 0$, solutions are attracted to the fixed point at the origin,

Figure 7.9: Time series for the magnetic activity with $N_D < 0$ and the parameters $\frac{\omega}{L} = -10$, $\alpha_0 = 5$, $\tau_p = \tau_\phi = 1$, $T_0 = 10$, $T_1 = 4$.

Figure 7.10: Time series for the magnetic activity with $N_D < 0$ and the parameters $\frac{\omega}{L} = -16$, $\alpha_0 = 8$, $\tau_p = \tau_\phi = 1$, $T_0 = 10$, $T_1 = 4$.

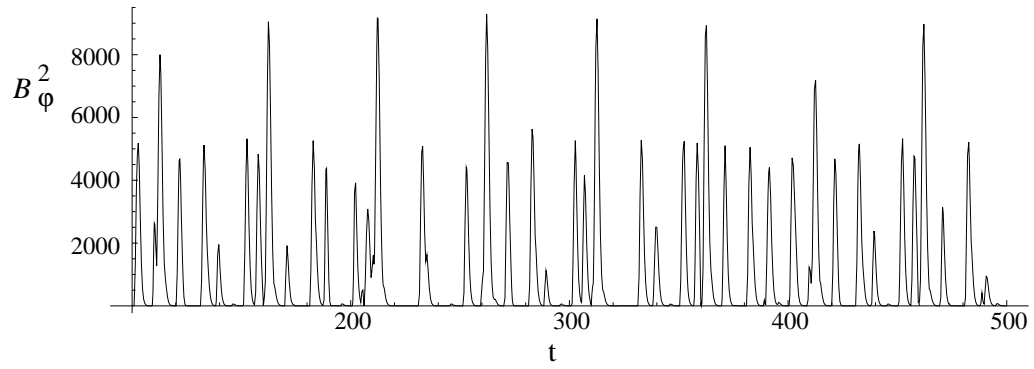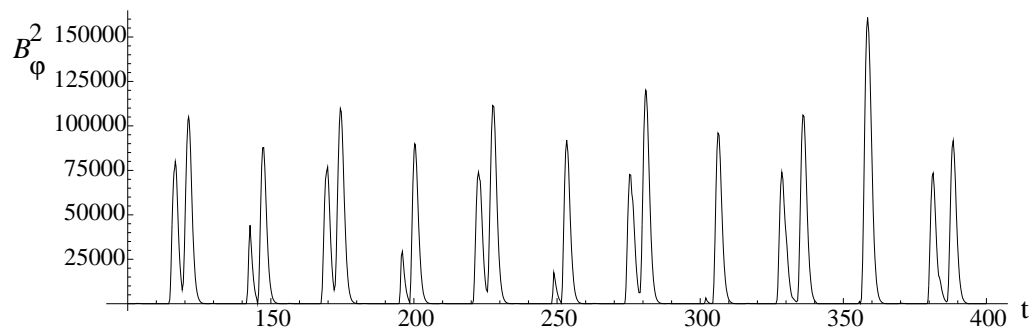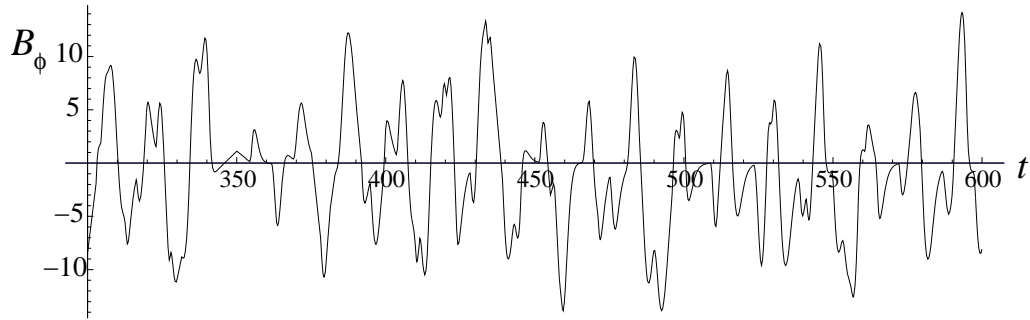Figure 7.11: Time series for the toroidal field with $N_D > 0$ and initial solution $A(t) = B_\phi(t) = \cos(t)$. The parameters $\frac{\omega}{L} = -3$, $\alpha_0 = -1$, $\tau_p = \tau_\phi = 1$, $T_0 = 10$, $T_1 = 4$ have been taken.

$A, B_\phi \rightarrow 0$. When $N_D < -1$ oscillatory solutions which are characteristically irregular are obtained. A typical example of solutions obtained at low dynamo number is illustrated in Figure 7.8, where the time series for the poloidal field, A, toroidal field, B_ϕ, and magnetic activity, B_ϕ^2, are shown. Note that B_ϕ does not always lie within the range $[-B_{max}, B_{max}]$. Both A and B_ϕ show a long-term cycle (approximately 8.5 of which are illustrated here), where the fields oscillate between positive and negative signs, and is regular in its length, P say. The parameters taken in Figure 7.8 result in an average period $P = 31.6$ time-units. Within each half-cycle the field also oscillates, leading to a time series for the magnetic activity which does not have an underlying magnetic sequence oscillating between positive and negative signs. Both the period and amplitude of the activity cycle are irregular.

As the dynamo number is increased, amplitude modulation leads to time-spans where magnetic activity is considerably reduced, as apparent in Figures 7.9 and 7.10. Although the basic cycle persists throughout these episodes, the field strengths are significantly below the average values. The episodes become more regular with increasing dynamo number; a pattern to the events is clear in Figure 7.10 for example. Just as in the flux transport dominated case the amplitude of oscillation increases with dynamo number, as illustrated in Figures 7.8-7.10. However, the maximum amplitude is now not constant from cycle to cycle. For a given set of parameters τ_p, τ_ϕ, T_0 and T_1, there exist certain parameter values ω/L and α_0 such that the amplitude of solution is relatively regular, with Figure 7.10 providing an example of this. Fixing ω/L, α_0, τ_p and τ_ϕ in such a case and increasing the total time delay $T_0 + T_1$ no longer gives rise to a predictable trend in behaviour as found in the flux transport dominated case and illustrated in Figure 7.6. In this regime, the mean amplitude of solution remains constant with increasing $T_0 + T_1$, butxs the duration of minima and number of cycles between each minima varies irregularly with increasing $T_0 + T_1$.

Next, looking at solutions for positive dynamo number, $N_D > 0$, we find that the form of initial solution specified becomes important in determining the nature of the solution obtained. For initial solutions whose sign varies on a time-scale comparable or less than the diffusive time-scale, it is possible to obtain solutions which are qualitatively similar to those for which $N_D < 0$. An example is shown in Figure 7.11 where the initial solution $A(t) = B_\phi(t) = \cos(t)$ for $t \in [-T_0 - T_1, 0]$ has been specified. This may be compared to Figure 7.8, where $N_D < 0$. On increasing N_D the maximum field strength is again seen to increase, with periods of reduced activity occuring at higher dynamo numbers.

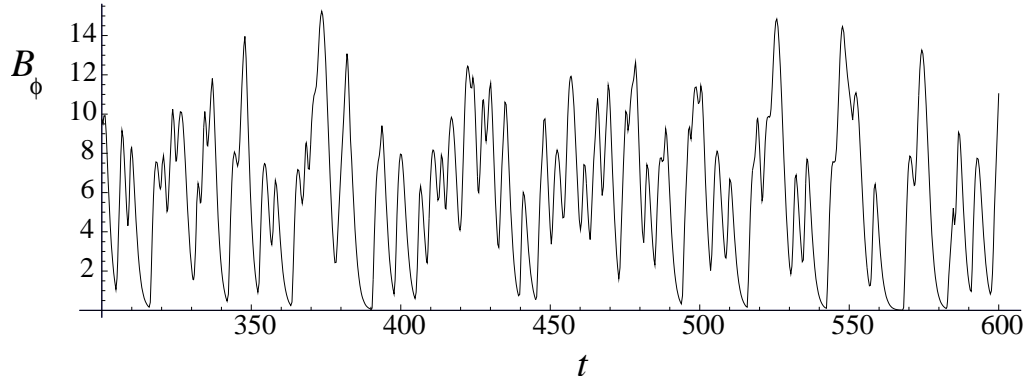A second type of solution occurs for $N_D > 0$, in which single signed oscillations of irregular amplitude

Figure 7.12: Time series for the toroidal field with $N_D > 0$ and constant initial solution. The parameters $\frac{\omega}{L} = -3$, $\alpha_0 = -1$, $\tau_p = \tau_\phi = 1$, $T_0 = 10$, $T_1 = 4$ have been taken.

and period are present. These solutions arise when the initial solutions vary only slowly when compared to the diffusive time-scales. An example is shown in Figure 7.12, where the constant initial solutions $A(t) = B_\phi(t) = 5$ for $t \in [-T_0 - T_1, 0]$ have been taken but the same parameters for Figure 7.11 used. In these low dynamo number solutions the minimum in magnetic energy is non-zero for sustained periods of time. On increasing the dynamo number periods of reduced activity in these single signed oscillations become apparent, in which between bursts of activity the field strength is near zero.

The analogy with a damped driven oscillator given by equation (7.4) can help explain some of these features. In the case $N_D < 0$, equations (7.7) and (7.6) may again be used to explain the point of bifurcation from a steady state to cyclic behaviour. Substituting $\tau = 1$, $T_d = 14$ into (7.7) implies $\Omega = 0.196$ at this bifurcation, corresponding to a period $P = 31.95$. Substituting this value for Ω into (7.6) to gives the dynamo number at the point of bifurcation as $N_D = -1.039$, corresponding closely to that found in the simulations.

For sufficiently low dynamo number the amplitude of the solution is small, and so B_ϕ is, for most of the time, within the range $[-B_{max}, B_{max}]$ over which the driving term on the right hand side of equation (7.4) operates. When the solution is outside of this range the high diffusivity ensures the field decays to within this range once again on a timescale shorter than the sum of the time delays. This rapidity when compared to the time delays distinguishes the solution from the flux transport dominated case since each time the delayed solution $B_\phi(t - T_0 - T_1)$ decays to $\pm B_{max}$, the solution $B_\phi(t)$ will have different magnitude, and may be of different sign, so changing the nature of the driving force. In this manner the short diffusive time-scales ensure it is possible to obtain double-signed oscillations when $N_D > 0$ (which cannot be achieved in the flux transport dominated regime). Such a solution relies on the sign of $B_\phi(t)$ being different to $B_\phi(t - T_0 - T_1)$ when $B_\phi(t - T_0 - T_1)$ decays to lie within the range $[-B_{max}, B_{max}]$. This will ensure that the term on the right-hand side of (7.4), $NB_\phi(t - T_0 - T_1)$, acts to drive the solution toward a different sign. At some $t > 0$ the solution $B_\phi(t)$ will leave the range $[-B_{max}, B_{max}]$, but now the rapid decay of the solution has the result that $B_\phi(t - T_0 - T_1)$ may be of different sign to $B_\phi(t)$, given suitable initial conditions. Such conditions were specified in Figure 7.11, where double-signed oscillations occur.

7.4 Discussion

A number of generalisations can be made to the above analysis. In particular it has been assumed throughout that $\tau_p = \tau_\phi$. In the more generic case, where $\tau_p \neq \tau_\phi$, the qualitative nature of the results described above remains. The same behaviour is to be expected from equation (7.4) since, when the solution $B_\phi(t)$ lies outside of the range $[-B_{max}, B_{max}]$ and the driving term is zero, a change from $\tau_p = \tau_\phi$ to $\tau_p \neq \tau_\phi$ has the effect of converting the system from a damped oscillator to an overdamped oscillator, for which solutions are qualitatively similar.

It has been assumed that during the flux transport no dissipative effects act on the fields – the source terms in equations (7.2) and (7.3) are proportional to ω/L and α_0 respectively. In the most general case the fields may be subject to dissipative losses during their transportation from one source region to another. Accordingly, extra loss factors can be introduced to the equations to take dissipation into account, which we would expect to become important only when flux transport is by spatial diffusion, specifically in the diffusion dominated regime. In this case the general form of the equations should be

$$\frac{dB_\phi(t)}{dt} = \frac{\omega}{L} e^{-T_0/\tau_p} A(t - T_0) - \frac{B_\phi(t)}{\tau_\phi}, \tag{7.8}$$

$$\frac{dA(t)}{dt} = \alpha_0 f\left(B_\phi(t - T_1) e^{-T_1/\tau_\phi}\right) e^{-T_1/\tau_\phi} B_\phi(t - T_1) - \frac{A(t)}{\tau_p}. \tag{7.9}$$

The additional multiplicative exponential factors are close to unity (and hence unimportant) in the flux transport dominated case, but small (and hence important) in the diffusion dominated case. However, in both situations qualitatively similar behaviour to that described in Section 7.3 may be obtained given a suitable re-scaling of the parameters ω/L and α_0 (corresponding to an increase in dynamo number). The resultant solutions are then of greater amplitude compared with the system (7.2), (7.3), since it can be seen from equation (7.4) that an exponential term within the quenching factor f will have the effect of increasing the range of B_ϕ over which forcing operates.

We considered a particular choice of algebraic α-effect that gives rise to the possibility of having both a lower and an upper cut-off in the range over which the α-effect operates. In the examples illustrated above, the value of B_{min} is such that the α-effect is non-zero throughout the range $[-B_{max}, B_{max}]$, although its value decreases rapidly outside the range $[|B_{min}|,|B_{max}|]$. With an increase of B_{min} such that there is some finite range between $[-B_{max}, B_{max}]$, centred at $B_\phi = 0$, where the α-effect is zero, the majority of the solution types described above can be recovered. The exceptions are the behaviour at low dynamo numbers, both in the diffusion dominated case shown in Figure 7.8, and in the flux transport dominated case shown in Figure 7.3. These solutions rely on the quenching factor f being non-zero within $[-B_{max}, B_{max}]$ and $B_\phi(t)$ being contained within that range. This is no longer the case with a higher value B_{min}.

If an explanation of both the flux transport dominated and diffusion dominated regimes in terms of an analogy with a damped driven oscillator can be invoked, then the nature of the driving term (given by the right-hand side of equation (7.4)) is important. In the first case since the diffusive timescales are long when compared to the time delays, and once the solution $B_\phi(t)$ is not within the range $[-B_{max}, B_{max}]$ for all time, the sign combination $B_\phi(t)B_\phi(t - T_0 - T_1)$ will always be positive when the driving term begins
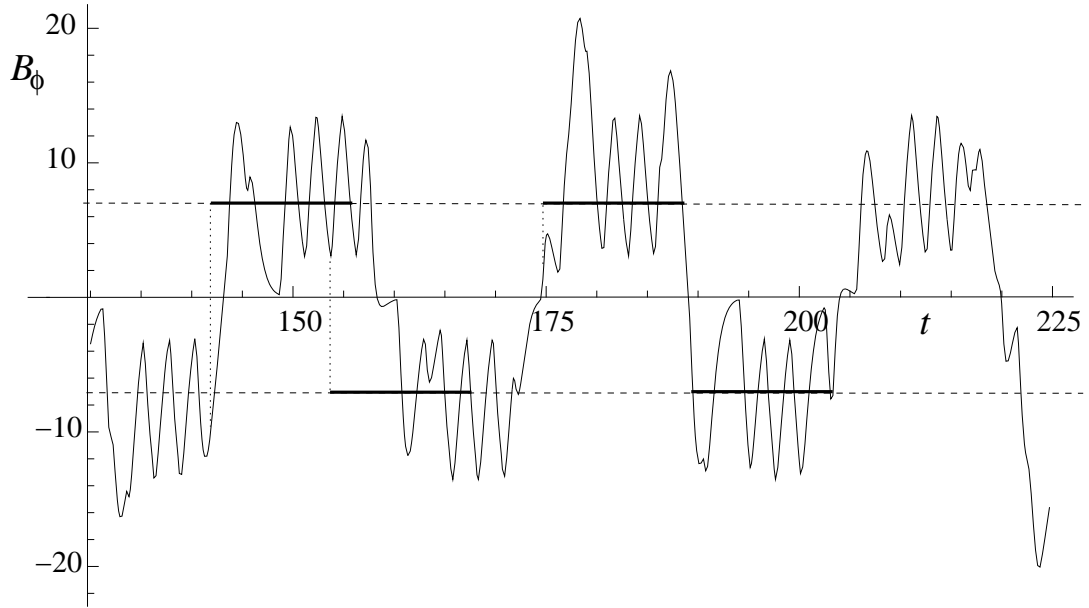
Figure 7.13: Time series for the toroidal field in the diffusion dominated case with $N_D < 0$ and using the parameters $\frac{\omega}{L} = -6$, $\alpha_0 = 3$, $\tau_p = \tau_\phi = 0.5$, $T_0 = 10$, $T_1 = 4$. The dashed lines indicate the boundaries of the forcing region and the thick solid lines are of length $T_0 + T_1 = 14$ corresponding to the total time delay. The first two bars have been placed to illustrate a negative sign combination of $B_\phi(t)B_\phi(t - T_0 - T_1)$ which leads to further oscillation within a half cycle, and the final two bars to illustrate the positive sign combination of $B_\phi(t)B_\phi(t - T_0 - T_1)$ present at the end of each half-cycle.

to act during the declining phase of each cycle. This predictability leads to the regularity in the system, to the single-signed oscillations for $N_D > 0$ and to the double-signed oscillations for $N_D < 0$. In the second case, since the rapid diffusivities ensure the solution returns to the forcing region in a timescale shorter than the time delays, the sign combination $B_\phi(t)B_\phi(t - T_0 - T_1)$ will not be fixed as in the diffusive case. Thus, the sign of the driving term will vary between cycles and within each half-cycle, leading to irregularity in the system. Figures 7.13 and 7.14 illustrate these effects. They show typical solutions in each of the regimes, with bars corresponding to the length of the time delays superimposed on the solution to illustrate the sign combinations of $B_\phi(t)B_\phi(t - T_0 - T_1)$ and, in the flux transport dominated case, the change in gradient of the solution as it enters the forcing region.

7.5 Summary

To summarise, we have constructed a physically motivated reduced stellar dynamo model, which includes time delays (in the flux transport), to study the effects of spatial segregation of the dynamo source-regions in stellar convection zones. The model can be generalized to study a diverse set of α-effect mechanisms located at different layers in stellar convection zones, such as the tachocline, or the base of the convection zone, or near the surface. This can be achieved by varying the time delays to appropriately account for the dominant flux transport mechanisms that are unique to a specific dynamo model based on a particular α-effect mechanism. This can be, for example, the meridional circulation timescale in Babcock-Leighton
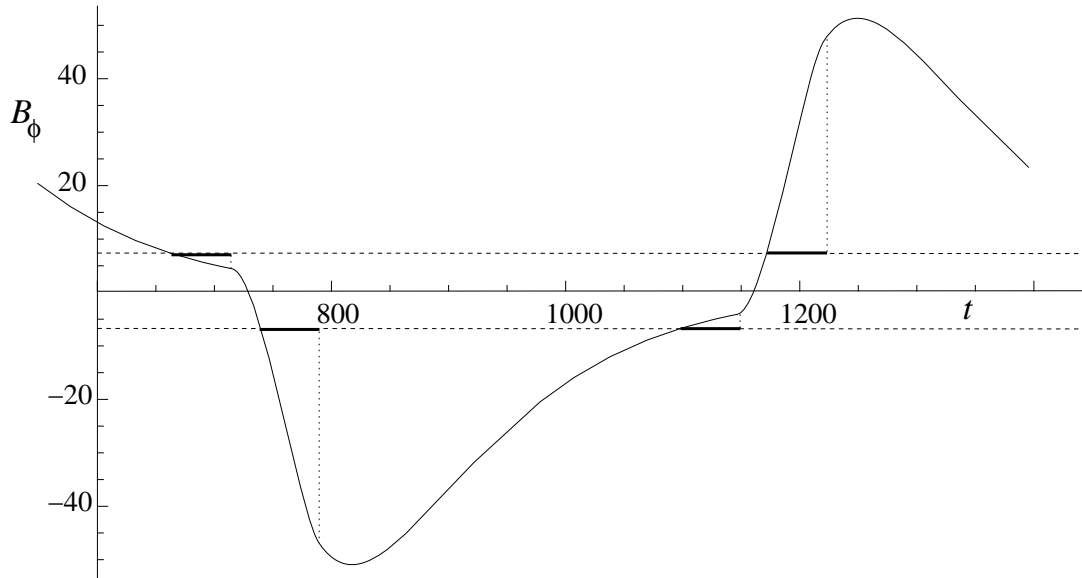
Figure 7.14: Time series for the toroidal field in the flux transport dominated case with $N_D < 0$ and using the parameters $\frac{\omega}{L} = -0.008$, $\alpha_0 = 0.008$, $\tau_p = \tau_\phi = 100$, $T_0 = 40$, $T_1 = 10$. The dashed lines indicate the boundaries of the forcing region and the thick solid lines are of length $T_0 + T_1 = 50$ corresponding to the total time delay. The bars have been placed to illustrate firstly the change in gradient of solution as $B_\phi(t - T_0 - T_1)$ enters the forcing region (before which the solution is purely diffusive) and secondly the switch in the solution from being driven to being purely diffusive as the solution $B_\phi(t - T_0 - T_1)$ leaves the forcing region.

dynamo models, or the turbulent pumping timescale in interface (or other) dynamo models that do not rely on meridional circulation. Motivated by stellar activity observations and the wide parameter space it offers, we have explored the dynamics of our model by increasing the dynamo number N_d (consequently reducing the Rossby number R_o), specifically for two extreme regimes.

In the flux transport dominated regime some similarity to the solar cycle is seen. On increasing the dynamo number a transition from no magnetic activity to oscillatory behaviour occurs. The solutions show polarity reversal however only in the case of negative dynamo number, which, when the differential rotation ω/L is assumed to be negative (as is observed in the high latitude part of the solar tachocline), corresponds to a positive alpha effect (as is the case in the Babcock-Leighton mechanism). The steep rising phase and longer declining phase resembles that of the sunspot cycle; the similarity of the solar cycle to a non-linear relaxation oscillator was noted in Mininni et al. (2001). As expected, upon increasing the dynamo number, the level of magnetic activity increases. Although the period of the magnetic cycle is significantly longer than both the length of the time delays and the diffusive timescales, the expected qualitative behaviour of the dynamo (i.e., increasing period of oscillation and amplitude with increasing time delays) is recovered. However, events such as grand-minima would be hard to explain in this model-regime without invoking some form of stochasticity in the poloidal source term or including some other physics. Nevertheless, given the similarity of the solutions in this case with other aspects of the solar cycle, we conclude that the solar dynamo is possibly (in its present state of activity) in the flux transport dominated regime.

The model is capable of irregular behaviour, including significant amplitude modulation, in the diffusion

dominated regime. In this case the magnetic cycle shows polarity reversal for both positive and negative dynamo numbers, and has an average length, about which it shows small variations. The average length of each magnetic cycle is of the same order as the sum of the two time delays. Amplitude modulation is seen for solutions along a cut through parameter space corresponding to increasing dynamo numbers, although the character of the modulation varies considerably. For small dynamo numbers episodes of minimal activity are present which are short compared to the cycle period, and that are spaced irregularly in time. On increasing the dynamo number, the duration of events becomes longer, and is regular in both length and spacing for larger dynamo numbers. These phases of reduced activity are reminiscent of the solar Maunder minima; however, the overall nature of the magnetic activity is qualitatively similar to many stars in the Mt. Wilson project which show highly irregular behavior. This may imply that these latter stars, which exhibit irregular magnetic activity, support dynamos whose underlying physics is similar to the diffusion dominated regime of our model.

It would be possible to take a cut through parameter space, corresponding to increasing dynamo number, that links both of these regimes. Taking an increase in $|\alpha_0\omega/L|$ but a decrease in $\tau_p\tau_\phi$ in such a way as to increase $|N_D|$, moves solutions from the regular oscillations present in the flux transport dominated regime, to the irregular nature of the diffusion dominated regime, and increases the level of magnetic activity. This is exactly the behaviour observed in solar-like stars, whose magnetic activity is distinguished by rotation rate (recall that low Rossby number R_o corresponds to high dynamo number N_d). While this particular cut through parameter space may be artificial because it is not clear how field diffusivities are affected by rotation rate, the principle of increasing a system parameter and observing a qualitative change in solutions provides an useful analogy to stellar activity observations.

Chapter 8

Summary and Future Work

8.1 Summary

In Chapter 3 we used an expansion technique to address one of the questions raised by the work of Hornig and Priest (2003): does the freedom to impose an ideal flow on the particular reconnective solution arise from the neglect of the momentum equation or is it inherent to the 3D process? The investigations presented suggest the latter, with several examples found in which ideal and non-ideal solutions are decoupled. In these solutions the inclusion of an ideal flow does not change the reconnection rate itself, but does have a significant effect on the evolution of magnetic flux and hence changes the interpretation of the reconnection rate. The fundamental counter-rotational reconnective plasma flows previously found to arise as a consequence of the 3D localisation of the non-ideal region were confirmed.

In the analysis of Chapter 3, as well as in previous models of 3D reconnection processes (Hornig and Priest, 2003, Pontin et al., 2004, 2005b), the localisation of the non-ideal region is imposed via a localisation of the plasma resistivity, η. In Chapter 4 we presented an example of a 3D reconnection process in which the current term itself is localised in all three-dimensions. The field geometry considered is elliptic – reconnection in such a geometry can only occur in 3D. We developed qualitative and quantitative models for the process, termed *flux-tube disconnection*, and determined how the reconnection rate and size of the non-ideal region scale with the imposed plasma velocities.

In Chapter 5, a numerical experiment modelling an elementary heating event was described. In the experiment two intertwined magnetic flux tubes were taken with spinning driving velocities imposed on their magnetic footpoints. The distribution of magnetic flux was followed in time and magnetic reconnection, which exhibited flux pile-up characteristics, was found to occur continuously across a central separator current sheet. Several comparisons were made with a similar experiment, described by De Moortel and Galsgaard (2006b), in which the same boundary driving velocities were imposed in initially separate magnetic flux tubes, and the two situations were shown to have many common characteristics.

In the remaining two chapters of the thesis we explored the slightly different question of how the large-

scale solar magnetic field is continually regenerated via dynamo action. Chapter 6 presented a third-order ODE model of a dynamo, derived via bifurcation theory, that displays the underlying mathematical structure expected to be present in spatially extended models. This allowed for an in-depth investigation of the nature of solutions present in various regions of parameter space. The model is able to reproduce many of the basic types of behaviour found in observations of solar-type stars. In the appropriate parameter regime, a chaotic modulation of the basic cycle is present, together with varying periods of low activity such as that observed during the Maunder minimum.

The simple model for the dynamo process presented in Chapter 7 was derived from physical motivations and consists of two coupled delay (or functional) differential equations. Through the use of time delays the generation of field components in spatially segregated layers and the communication between them was modelled. A variety of dynamic behaviours were found to arise in the model, with different parameter regimes giving rise to periodic and aperiodic oscillations. Two characteristic regimes were found, the flux-transport dominated regime (in which the time delays are smaller than the dissipative timescale) and the diffusion dominated regime (where the opposite situation is found). The Sun itself is expected to be in the flux-transport dominated regime, whose solutions were found to be regular.

8.2   Questions outstanding

There are several questions arising from the work presented in this thesis. We briefly detail some of these questions here.

Chapter 3: Dynamic Non-Null Reconnection

- We detailed some examples in which the scheme is solved explicitly up to third order. In principle the remaining orders can be solved numerically. To do so involves solving all quantities on a grid on the hyperbolic-flux tube. What is the best way to do this? If such a scheme is set up then we can examine a number of factors, the most obvious and important being the nature of the higher-order terms.

- How is the rate of reconnection determined in the model?

- Is it possible to include additional physical effects (such as the Hall term) in the expansion and still obtain a similar scheme? If so, what are the consequences of including these terms?

- Can we make a sufficiently good choice of the free functions and variables in the first few orders of the scheme to allow a closed solution to be obtained (this seems somewhat unlikely).

Chapter 4: Flux-Tube Disconnection

- One drawback to the analysis presented is in the neglect of the momentum equation (i.e. the kinematic nature of the analysis). Is a straight flux-tube physically realistic? The momentum equation should

determine whether the tube expands or contracts (or both) as it is spun (for a similar investigation see Browning and Hood (1989)).

- It will probably not be very easy to include the momentum equation in the analytical work (although approaching the problem via the expansion scheme of Chapter 3 may give some insight). Instead, or in addition, a 3D MHD numerical investigation of the problem would be interesting. In such an experiment it would be possible to take a flux-tube and gradually ramp-up a spinning footpoint velocity on the ends of the tube. Accordingly, such an experiment would be useful in addressing questions relating to the stability and dynamic accessibility of the solution.

- On a slightly different note, is it possible to find field line mappings (and therefore carry out an analysis similar to the quantitive one presented here) for a hyperbolic magnetic field with a localised current?

Chapter 5: An MHD experiment into the effect of spinning boundary motions on misaligned flux-tubes

The material presented in this chapter corresponds only to a preliminary investigation of the numerical experiment. A significant number of questions have not been addressed and will need to be in future. For example:

- What is the nature of the magnetic flux connectivity in the experiment and how does the connectivity evolve in time? Having gained such a knowledge, what do we learn about the reconnection process?

- Is it possible to track magnetic field lines attached to fluid elements in time? To do so would enable a better understanding of where the reconnection is taking place and the nature of the reconnection.

- A flux pile-up regime is often associated with a high-β environment. The values of β used in the experiment are unrealistically high if the situation is to represent a coronal environment. It would be interesting to redesign the experiment with a low β and see whether the same behaviour persists.

Chapter 7: A Time-Delay Model for Solar and Stellar Dynamos

The solar dynamo is in the flux-transport dominated regime. Although solutions in this category show several similarities to the solar dynamo, modulation of cycle amplitude and variable cycle lengths are not observed. However the amplitude of the solar meridional circulation is known to vary significantly with Snodgrass and Dailey (1996) finding that

> *The activity-cycle-related time variations of the meridional motion are as large as the motion itself . . . there are no latitudes at which the motion is steady during the course of the cycle.*

Is it possible that, with the inclusion of a variable meridional circulation in the model (corresponding to a variable time-delay T_0), amplitude and period modulation and even intermittency could arise in the flux-transport dominated regime? Preliminary investigations suggest so. Figure 8.1 shows the time series for B_ϕ^2 and A^2 for a solution in the flux-transport dominated regime where T_0 is varied in time stochastically by 80% of its mean value. A full investigation into this phenonomen is currently underway, attempting to answer questions such as:
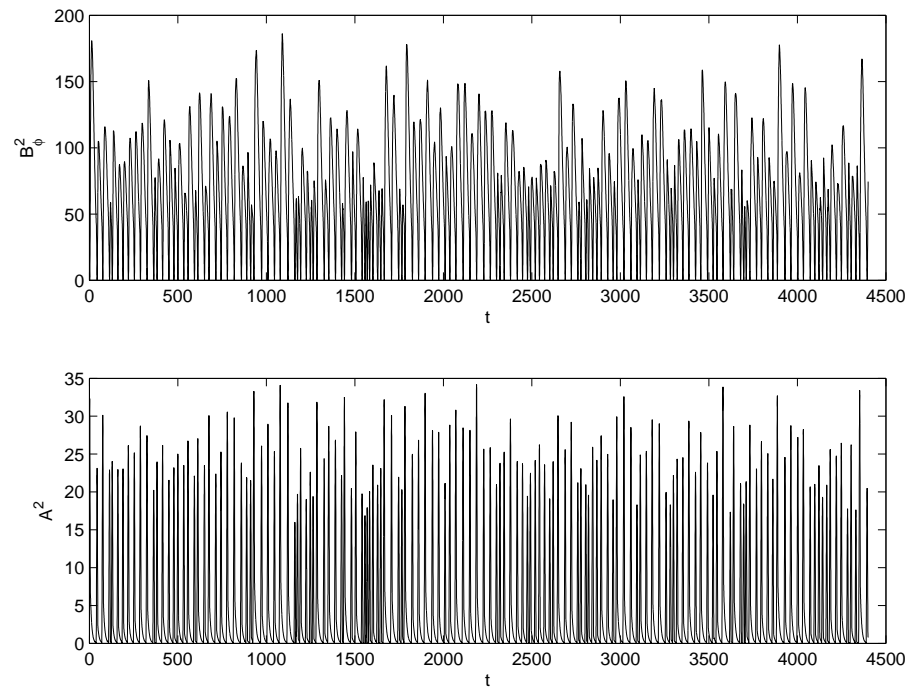
Figure 8.1: Time-series B_ϕ^2 and A^2 with a stochastically varying time-delay T_0. The solutions show significant amplitude and period modulation.

- How do long-term fluctuations in the time-delay T_0 affect the cycle?

- What is the nature of solutions when stochastic fluctuations in the time-delay T_0 are taken? How do they differ for various coherence times and amplitude of fluctuations?

- What is the effect of including time variation in the amplitude of the alpha effect (i.e. in α_0)?

Bibliography

P. Ashwin, A.M. Rucklidge, and R. Sturman. Two-state intermittency near a symmetric interaction of saddle-node and hopf bifurcations: a case study from dynamo theory. *Physica D Nonlinear Phenomena*, 194:30, 2004.

W.I. Axford. *Magnetic Reconnection in Space and Laboratory Plasmas*, volume 30 of *Geophys. Monogr. Ser.*, chapter 1, page 1. AGU, Washington D.C., 1984.

H.W. Babcock. The topology of the sun's magnetic field and the 22-year cycle. *The Astrophysical Journal*, 133:572, 1961.

S.L. Baliunas et al. Chromospheric variations in main-sequence stars. *The Astrophysical Journal*, 438:269, 1995.

J. Beer, S. Tobias, and N. Weiss. An active sun throughout the maunder minimum. *Solar Physics*, 181:237, 1998.

D. Biskamp. Magnetic reconnection via current sheets. *Physics of Fluids*, 29:1520, 1986.

T.J.M. Boyd and J.J Sanderson. *The Physics of Plasmas*. Cambridge University Press, 2003.

A. Brandenburg, I. Tuominen, A. Nordlund, P. Pulkkinen, and R.F. Stein. 3-d simulation of turbulent cyclonic magneto-convection. *Astronomy and Astrophysics*, 232:277, 1990.

J. Brooke, D. Moss, and A. Phillips. Deep minima in stellar dynamos. *Astronomy and Astrophysics*, 395: 1013, 2002.

D.S. Brown, C.E. Parnell, E.E. Deluca, L. Golub, and R.A. McMullen. The magnetic structure of a coronal x-ray bright point. *Solar Physics*, 201:305, 2001.

P.K. Browning and A.W. Hood. The shape of twisted, line-tied coronal loops. *Solar Physics*, 124:271, 1989.

A.S. Brun, M.S. Miesch, and J. Toomre. Global-scale turbulent convection and magnetic dynamo action in the solar envelope. *The Astrophysical Journal*, 614:1073, 2004.

P.J. Bushby. Modelling dynamos in rapidly rotating late-type stars. *Monthly Notices of the Royal Astronomical Society*, 342:L15, 2003.

P.J. Bushby. Zonal flows in a mean-field solar dynamo model. *Astronomische Nachrichten*, 326:218, 2005.

A.R. Champneys and V. Kirk. The entwined wiggling of homoclinic curves emerging from saddle-node/hopf instabilities. *Physica D Nonlinear Phenomena*, 195:77, 2004.

K.H. Chan, X. Liao, K. Zhang, and C.A. Jones. Non-axisymmetric spherical interface dynamos. *Astronomy and Astrophysics*, 423:L37, 2004.

P. Charbonneau. Multiperiodicity, chaos, and intermittency in a reduced model of the solar cycle. *Solar Physics*, 199:385, 2001.

P. Charbonneau, G. Blais-Laurier, and C. St-Jean. Intermittency and phase persistence in a babcock-leighton model of the solar cycle. *The Astrophysical Journal Letters*, 616:L183, 2004.

P. Charbonneau, C. St-Jean, and P. Zacharias. Fluctuations in babcock-leighton dynamos. i. period doubling and transition to chaos. *The Astrophysical Journal*, 619:613, 2005.

P. Chatterjee, D. Nandy, and A.R. Choudhuri. Full-sphere simulations of a circulation-dominated solar dynamo: Exploring the parity issue. *Astronomy and Astrophysics*, 427:1019, 2004.

E. Covas and R. Tavakol. Crisis-induced intermittency in truncated mean field dynamos. *Physical Review E*, 55:6641, 1997.

T.G. Cowling. The magnetic field of sunspots. *Montly Notices of the Royal Astronomical Society*, 91:39, 1934.

A. Cox. Geomagnetic reversals. *Science*, 163:237, 1969.

I. De Moortel and K. Galsgaard. Numerical modelling of 3d reconnection due to rotational footpoint motions. *Astronomy and Astrophysics*, 451:1101, 2006a.

I. De Moortel and K. Galsgaard. Numerical modelling of 3d reconnection. ii. comparison between rotational and spinning footpoint motions. *Astronomy and Astrophysics*, 459:627, 2006b.

M. Dikpati and P. Charbonneau. A babcock-leighton flux transport dynamo with solar-like differential rotation. *The Astrophysical Journal*, 518:508, 1999.

M. Dikpati and P.A. Gilman. Flux-transport dynamos with α-effect from global instability of tachocline differential rotation: A solution for magnetic parity selection in the sun. *The Astrophysical Journal*, 559:428, 2001.

S. D'Silva and A.R. Choudhuri. A theoretical model for tilts of bipolar magnetic regions. *Astronomy and Astrophysics*, 272:621, 1993.

D.K. Duncan, A.H. Vaughan, O.C. Wilson, G.W. Preston, J. Frazer, H. Lanning, A. Misch, J. Mueller, D. Soyumer, L. Woodard, S.L. Baliunas, R.W. Noyes, L.W. Hartmann, A. Porter, C. Zwaan, F. Middelkoop, R.G.M. Rutten, and D. Mihalas. Ca ii h and k measurements made at mount wilson observatory, 1966-1983. *The Astrophysical Journal Supplement*, 76:383, 1991.

B. R. Durney. On the torsional oscillations in babcock-leighton solar dynamo models. *Solar Physics*, 196:1, 2000.

B.R. Durney. On a babcock-leighton dynamo model with a deep-seated generating layer for the toroidal magnetic field. *Solar Physics*, 160:213, 1995.

B..R. Durney. On a babcock-leighton solar dynamo model with a deep-seated generating layer for the toroidal magnetic field. iv. *The Astrophyiscal Journal*, 486:1065, 1997.

B.R. Durney and J. Latour. On the angular momentum loss of late-type stars. *Geophysical and Astrophysical Fluid Dynamics*, 9:241, 1978.

D.M. Eardley and A.P. Lightman. Magnetic viscosity in relativistic accretion disks. *The Astrophysical Journal*, 200:187, 1975.

J.A. Eddy. The maunder minimum. *Science*, 192:1189, 1976.

Y. Fan, G.H. Fisher, and A.N. McClymont. Dynamics of emerging active region flux loops. *The Astrophysical Journal*, 436:907, 1994.

A. Ferriz-Mas, D. Schmitt, and M. Schuessler. A dynamo effect due to instability of magnetic flux tubes. *Astronomy and Astrophysics*, 289:949, 1994.

K. Galsgaard and Å Nordlund. Heating and activity of the solar corona 1. boundary shearing of an initially homogeneous magnetic field. *Journal of Geophysical Research*, 101:13445, 1996.

K. Galsgaard and Å Nordlund. Heating and activity of the solar corona. 3. dynamics of a low beta plasma with three-dimensional null points. *Journal of Geophysical Research*, 102:231, 1997.

K. Galsgaard and C.E. Parnell. Elementary heating events - magnetic interactions between two flux sources. iii. energy considerations. *Astronomy and Astrophysics*, 439:335, 2005.

K. Galsgaard, C.E. Parnell, and J. Blaizot. Elementary heating events - magnetic interactions between two flux sources. *Astronomy and Astrophysics*, 362:395, 2000.

P.A. Gilman and G.A. Glatzmaier. Compressible convection in a rotating spherical shell. i - anelastic equations. ii - a linear anelastic model. iii - analytic model for compressible vorticity waves. *The Astrophysical Journal Supplement Series*, 45:335, 1981.

R.M. Green. Modes of annihilation and reconnection of magnetic fields. In T. Gold, editor, *IAU Symp. 22: Stellar and Solar Magnetic Fields*, page 398, 1965.

J.L. Han and G.J. Qiao. The magnetic field in the disk of our galaxy. *Astronomy and Astrophysics*, 288: 759, 1994.

D. H. Hathaway, D. Nandy, R.M. Wilson, and E.J. Reichmann. Evidence that a deep meridional flow sets the sunspot cycle period. *The Astrophysical Journal*, 589:665, 2003.

A.L. Haynes, C.E. Parnell, K. Galsgaard, and E.R. Priest. Magnetohydrodynamic evolution of magnetic skeletons. *Proceedings of the Royal Society A*, 463:1097, 2007.

A. Hempelmann, J.H.M.M. Schmitt, and K. Stępień. Coronal x-ray emission of cool stars in relation to chromospheric activity and magnetic cycles. *Astronomy and Astrophysics*, 305:284, 1996.

M. Hesse and K. Schindler. A theoretical foundation of general magnetic reconnection. *Journal of Geophysical Research*, 93:5559, 1988.

G. Hornig and E.R. Priest. Evolution of magnetic flux in an isolated reconnection process. *Physics of Plasmas*, 10(7):2712, 2003.

G. Hornig and K. Schindler. Magnetic topology and the problem of its invariant definition. *Physics of Plasmas*, 3:781, 1996.

P. Hoyng. *The field, the mean and the meaning*, volume 9 of *The Fluid Mechanics of Astrophysics and Geophysics*, chapter 1, page 1. Taylor & Francis, 2003.

D.V. Hoyt and K.H. Schatten. How well was the sun observed during the maunder minimum? *Solar Physics*, 165:181, 1996.

D.E. Huddleston, C.T. Russell, G. Le, and A. Szabo. Magnetopause structure and the role of reconnection at the outer planets. *Journal of Geophysical Research*, 102:24289, 1997.

D.W. Hughes, R. Rosner, and N.O. Weiss, editors. *The Solar Tachocline*. Cambridge University Press, Cambridge, UK, 2007.

M. Jardine and E.R. Priest. Weakly nonlinear theory of fast steady-state magnetic reconnection. *Journal of Plasma Physics*, 40:143, 1988.

C.A. Jones, N.O. Weiss, and F. Cattaneo. Nonlinear dynamos: A complex generalization of the lorenz equations. *Physica D Nonlinear Phenomena*, 14:161, 1985.

V. Kirk. Breaking of symmetry in the saddle-node hopf bifurcation. *Physics Letters A*, 154:243, 1991.

E. Knobloch and A.S. Landsberg. A new model of the solar cycle. *Monthly Notices of the Royal Astronomical Society*, 278:294, 1996.

J.D. Landstreet. Magnetic fields at the surfaces of stars. *Astronomy and Astrophysics Review*, 4:35, 1992.

J. Larmor. How could a rotating body such as the sun become a magnet? *British Association for the Advancement of Science Reports*, page 159, 1919.

Y-T. Lau and J.M. Finn. Three dimensional kinematic reconnection in the presence of field nulls and closed field lines. *The Astrophysical Journal*, 350:672, 1990.

Y-Y. Lau and J.M. Finn. Three dimensional kinematic reconnection of plasmoids. *The Astrophysical Journal*, 366:577, 1991.

R.B. Leighton. A magneto-kinematic model of the solar cycle. *The Astrophysical Journal*, 156:1, 1969.

M. Linton and E.R. Priest. Three-dimensional reconnection of untwisted magnetic flux tubes. *The Astrophysical Journal*, 595:1259, 2003.

D.W. Longcope. Topology and current ribbons: A model for current, reconnection and flaring in a complex, evolving corona. *Solar Physics*, 169:91, 1996.

D.W. Longcope and S.G. Cowley. Current sheet formation along three-dimensional magnetic separators. *Physics of Plasmas*, 3:2885, 1996.

D.W. Longcope, D.E. McKenzie, J. Cirtain, and J. Scott. Observations of separator reconnection to an emerging active region. *The Astrophysical Journal*, 630:596, 2005.

P.C.H. Martens. Applications of nonlinear methods in astronomy. *Physics Reports*, 115:315, 1984.

J. Mason, D.W. Hughes, and S.M. Tobias. The competition in the solar dynamo between surface and deep-seated α-effects. *The Astrophysical Journal Letters*, 580:L89, 2002.

L. Mestel and H.C. Spruit. On magnetic braking of late-type stars. *Monthly Notices of the Royal Astronomical Society*, 226:57, 1987.

M.S. Miesch. Large-scale dynamics of the convection zone and tachocline. *Living Reviews in Solar Physics*, 2(1), 2005. cited on 22/03/07.

P. D. Mininni, D.O. Gomez, and G.B. Mindlin. Simple model of a stochastically excited solar dynamo. *Solar Physics*, 201:203, 2001.

H. K. Moffatt. *Magnetic field generation in electrically conducting fluids.* Cambridge University Press, 1978.

B. Montesinos, J.H. Thomas, P. Ventura, and I. Mazzitelli. A new look at the relationship between activity, dynamo number and rossby number in late-type stars. *Monthly Notices of the Royal Astronomical Society*, 326:877, 2001.

D. Nandy. Constraints on the solar internal magnetic field from a buoyancy driven solar dynamo. *Astrophysics and Space Science*, 282:209, 2002.

D. Nandy. Meridional circulation and the solar magnetic cycle. In D. Danesy, editor, *ESA SP-559: SOHO 14 Helio- and Asteroseismology: Towards a Golden Future*, page 241, 2004.

D. Nandy and A.R. Choudhuri. Explaining the latitudinal distribution of sunspots with deep meridional flow. *Science*, 296:1671, 2002.

Å Nordlund and K. Galsgaard. A 3d mhd code fo parallel computers. Technical report, Astronomical Observatory, Copenhagen University, 1997.

C. Norman and J. Heyvaerts. Anomalous magnetic field diffusion during star formation. *Astronomy and Astrophysics*, 147:247, 1985.

R.W. Noyes, L.W. Hartmann, S.L. Baliunas, D.K. Duncan, and A.H. Vaughan. Rotation, convection, and magnetic activity in lower main-sequence stars. *The Astrophysical Journal*, 279:763, 1984a.

R.W. Noyes, N.O. Weiss, and A.H. Vaughan. The relation between stellar rotation rate and activity cycle periods. *The Astrophysical Journal*, 287:769, 1984b.

M. Ossendrijver. The solar dynamo. *The Astronomy and Astrophysics Review*, 11:287, 2003.

E.N. Parker. Hydromagnetic dynamo models. *The Astrophysical Journal*, 122:293, 1955.

E.N. Parker. Sweet's mechanism for merging magnetic fields in conducting fluids. *Journal of Geophysical Research*, 62:509, 1957.

E.N. Parker. The solar-flare phenomenon and the theory of reconnection and annihiliation of magnetic fields. *The Astrophysical Journal Supplement*, 8:177, 1963.

E.N. Parker. Topological dissipation and the small-scale fields in turbulent gases. *The Astrophysical Journal*, 174:499, 1972.

E.N. Parker. Magnetic neutral sheets in evolving fields - part two - formation of the solar corona. *The Astrophysical Journal*, 264:642, 1983.

E.N. Parker. A solar dynamo surface wave at the interface between convection and nonuniform rotation. *The Astrophysical Journal*, 408:707, 1993.

C.E. Parnell and K. Galsgaard. Elementary heating events - magnetic interactions between two flux sources. ii rates of flux reconnection. *Astronomy and Astrophysics*, 428:595, 2004.

C.E. Parnell, J.M. Smith T. Neukirch, and E.R. Priest. The structure of three-dimensional magnetic neutral points. *Physics of Plasmas*, 3:759, 1996.

C.E. Parnell, A.L. Haynes, and K. Galsgaard. Recursive reconnection and magnetic skeletons. *The Astrophysical Journal*, 2007. submitted.

H.E. Petschek. Magnetic field annihilation. In W.N. Hess, editor, *The Physics of Solar Flares*, page 425, 1964.

V.V. Pipin. The Gleissberg cycle by a nonlinear alpha L\ dynamo. *Astronomy and Astrophysics*, 346:295, 1999.

D.I. Pontin, G. Hornig, and E.R. Priest. Kinematic reconnection at a magnetic null point: spine-aligned current. *Geophysical and Astrophysical Fluid Dynamics*, 98:407, 2004.

D.I. Pontin, K. Galsgaard, G. Hornig, and E.R. Priest. A fully magnetohydrodynamic simulation of three-dimensional non-null reconnection. *Physics of Plasmas*, 12:2307, 2005a.

D.I. Pontin, G. Hornig, and E.R. Priest. Kinematic reconnection at a magnetic null point: Fan-aligned current. *Geophysical and Astrophysical Fluid Dynamics*, 99:77, 2005b.

F. Porcelli, D. Boucher, and J.M. Rosenbluth. Model for the sawtooth period and amplitude. *Plasma Physics and Controlled Fusion*, 38:2163, 1996.

G.W. Preston. The mean surface fields of magnetic stars. *The Astrophysical Journal*, 164:309, 1971.

E.R. Priest. *Solar Magnetohydrodynamics*. D. Reidel, 1982.

E.R. Priest and T.G. Forbes. New models for fast steady state magnetic reconnection. *Journal of Geophysical Research*, 91:5579, 1986.

E.R. Priest and L.C. Lee. Nonlinear magnetic reconnection models with separatrix jets. *Journal of Plasma Physics*, 44:337, 1990.

E.R. Priest and M.A. Raadu. Preflare current sheets in the solar atmosphere. *Solar Physics*, 43:177, 1975.

E.R. Priest and V.S. Titov. Magnetic reconnection at 3d null points. *Philosophical Transactions of the Royal Society*, 354:2951, 1996.

E.R. Priest, J.F. Heyvaerts, and A.M. Title. A flux-tube tectonics model for solar coronal heating driven by the magnetic carpet. *The Astrophysical Journal*, 576:533, 2002.

E.R. Priest, G. Hornig, and D. Pontin. On the nature of three-dimensional magnetic reconnection. *Journal of Geophysical Research Space Physics*, 108(A):7, 2003.

J.E. Pringle. On the formation of binary stars. *Monthly Notices of the Royal Astronomical Society*, 239: 361, 1989.

L. Rastaetter and T. Neukirch. Magnetic reconnection in a magnetosphere-accretion-disk system. axisymmetric stationary states and two-dimensional reconnection simulations. *Astronomy and Astrophysics*, 323:923, 1997.

C.B. Roald and J.H. Thomas. Simple solar dynamo models with variable alpha and omega effects. *Monthly Notices of the Royal Astronomical Society*, 288:551, 1997.

B. Roberts, P.M. Edwin, and A.O. Benz. On coronal oscillations. *The Astrophysical Journal*, 279:857, 1984.

M.M. Romanova and R.V.E. Lovelace. Magnetic field, reconnection, and particle acceleration in extragalactic jets. *Astronomy and Astrophysics*, 262:26, 1992.

S.H. Saar and A. Brandenburg. Time evolution of the magnetic activity cycle period. ii. results for an expanded stellar sample. *The Astrophysical Journal*, 524:295, 1999.

K. Schindler. *Physics of Space Plasma Activity*. Cambridge University Press, 2007.

K. Schindler, M. Hesse, and J. Birn. General magnetic reconnection, parallel electric fields, and helicity. *Journal of Geophysical Research*, 93:5547, 1988.

S. Schmalz and M. Stix. An alpha-omega dynamo with order and chaos. *Astronomy and Astrophysics*, 245: 654, 1991.

D. Schmitt, M. Schuessler, and A. Ferriz-Mas. Intermittent solar activity by an on-off dynamo. *Astronomy and Astrophysics*, 311:L1, 1996.

J. Schou et al. Helioseismic studies of differential rotation in the solar envelope by the solar oscillations investigation using the michelson doppler imager. *The Astrophysical Journal*, 505:390, 1998.

H.B. Snodgrass and S.B. Dailey. Meridional motions of magnetic features in the solar photosphere. *Solar Physics*, 163:21, 1996.

E.A. Spiegel and L.-P. Zahn. The solar tachocline. *Astronomy and Astrophysics*, 265:106, 1992.

M. Steenbeck and F. Krause. On the dynamo theory of stellar and planetary magnetic fields. i. ac dynamos of solar type. *Astronomische Nachrichten*, 291:49, 1969.

M. Steenbeck, F. Krause, and K.H. Rädler. Berechnung der mittleren lorentz feldstärke für ein elektrisch leitendes medium in turbulenter, durch coriolis kräfte beeinflusser bewegung. *Z. Naturforsch*, 21a:369, 1966.

P.A. Sweet. The neutral point theory of solar flares. In B. Lehnert, editor, *IAU Symp. 6: Electromagnetic Phenomena in Cosmical Physics*, page 123, 1958.

P.A. Sweet. Mechanisms of Solar Flares. *Annual Review of Astronomy and Astrophysics*, 7:149, 1969.

J.-C. Thelen. A mean electromotive force induced by magnetic buoyancy instabilities. *Monthly Notices of the Royal Astronomical Society*, 315:155, 2000.

V.S. Titov. On the method of calculating two-dimensional potential magnetic fields with current sheets. *Solar Physics*, 139:401, 1992.

S.M. Tobias. The solar cycle: parity interactions and amplitude modulation. *Astronomy and Astrophysics*, 322:1007, 1997.

S.M. Tobias. Grand minimia in nonlinear dynamos. *Astronomy and Astrophysics*, 307:L21, 1996.

S.M. Tobias, N.O. Weiss, and V. Kirk. Chaotically modulated stellar dynamos. *Monthly Notices of the Royal Astronomical Society*, 273:1150, 1995.

S.M. Tobias, N.H. Brummell, T.L. Clune, and J. Toomre. Transport and storage of magnetic field by overshooting turbulent compressible convection. *The Astrophysical Journal*, 549:1183, 2001.

C.A. Tout and J.E. Pringle. Accretion disc viscosity - a simple model for a magnetic dynamo. *Monthly

Notices of the Royal Astronomical Society, 259:604, 1992.

S.I. Vainshtein and Ya. B. Zeldovich. Origin of magnetic fields in astrophysics. *Soviet Physics Uspehki*, 15:159, 1972.

A.A. van Ballegooijen. Cascade of magnetic energy as a mechanism of coronal heating. *The Astrophysical Journal*, 311:1001, 1986.

V.M. Vasyliunas. Theoretical models of magnetic field line merging. i. *Reviews of Geophysics and Space Physics*, 13:303, 1975.

B. von Rekowski, C.E. Parnell, and E.R. Priest. Solar coronal heating by magnetic cancellation: I. connected equal bipoles. *Monthly Notices of the Royal Astronomical Society*, 366:125, 2006.

G. Wagner, J. Beer, J. Masarik, R. Muscheler, P.W. Kubik, W. Mende, C. Laj, G.M.Raisbeck, and F. Yiou. Presence of the solar de vries cycle (˜205 years) during the last ice age. *Geophysics Research Letters*, 28:303, 2001.

N.O. Weiss, F. Cattaneo, and C.A. Jones. Periodic and aperiodic dynamo waves. *Geophysical and Astrophysical Fluid Dynamics*, 30:305, 1984.

A. L. Wilmot-Smith, G. Hornig, and E.R. Priest. Dynamic non-null magnetic reconnection in three dimensions. i. particular solutions. *Royal Society of London Proceedings Series A*, 462:2877, 2006a.

A. L. Wilmot-Smith, G. Hornig, and E.R. Priest. Dynamic non-null magnetic reconnection in three dimensions. ii. composite solutions. *Geophysical and Astrophysical Fluid Dynamics*, 2007a. submitted.

A.L. Wilmot-Smith and I. De Moortel. Magnetic reconnection in flux-tubes undergoing spinning footpoint motions. *Astronomy and Astrophysics*, 473:615, 2007.

A.L. Wilmot-Smith and E.R. Priest. Flux-tube disconnection – an example of 3d reconnection. *Physics of Plasmas*, 14(10):102903, 2007.

A.L. Wilmot-Smith, P.C.H. Martens, D. Nandy, E.R. Priest, and S.M. Tobias. Low-order stellar dynamo models. *Monthly Notices of the Royal Astronomical Society*, 363:1167, 2005a.

A.L. Wilmot-Smith, E.R. Priest, and G. Hornig. Magnetic diffusion and the motion of field lines. *Geophysical and Astrophysical Fluid Dynamics*, 99:177, 2005b.

A.L. Wilmot-Smith, D. Nandy, G. Hornig, and P.C.H. Martens. A time delay model for solar and stellar dynamos. *The Astrophysical Journal*, 652:696, 2006b.

A.L. Wilmot-Smith, P.C.H. Martens, D. Nandy, E.R. Priest, and S.M. Tobias. Erratum: Low-order stellar dynamo models. *Monthly Notices of the Royal Astronomical Society*, 2007b. in preparation.

C.J. Xiao et al. In situ evidence for the structure of the magnetic null in a 3d reconnection event in the earth's magnetotail. *Nature Phys.*, 2:478, 2006.

H. Yoshimura. Nonlinear astrophysical dynamos - multiple-period dynamo wave oscillations and long-term modulations of the 22 year solar cycle. *The Astrophysical Journal*, 226:706, 1978.

I.B. Zeldovich, A.A. Ruzmaikin, and D.D. Sokolov, editors. *Magnetic fields in astrophysics*, 1983.